8-1999

Quantitative, Non-Destructive Calibration of Scanned Probe Microscope Cantilevers

John Hazel
Western Michigan University

QUANTITATIVE, NON-DESTRUCTIVE CALIBRATION OF SCANNED PROBE MICROSCOPE CANTILEVERS

by

John Hazel

A Thesis
Submitted to the
Faculty of The Graduate College
in partial fulfilment of the
requirements for the
Degree of Master of Science
Department of Construction Engineering,
Materials Engineering and Industrial Design

Western Michigan University
Kalamazoo, Michigan
August 1999

ACKNOWLEDGEMENTS

My thanks go to my wife, Debra Hazel, and my advisor, Vladimir Tsukruk who were the main driving forces to complete this program of study. My children, Amanda and Emily very patienly waited while Daddy worked on his thesis and also during revision helped keep page numbers in order. I also would like to thank the following people who contributed to this work: Dr. Valeriy Gorbunov, National Academy of Science, Belarus; Dr. Valery Bliznyuk, Oxford University; Zheng Huang, GM Research Labs; Dale Visser, Yale University; Dr. Tim Bunning, Wright Labs, USAF; Dr. Jason Cleveland, Digital Instruments Corp; Dr. Dimitri Vesenov, Harvard University; Dr. Alexander Noy, Lawrence Livermore Labs. Funding for my research at WMU was provided by the National Science Foundation and the Air Force Office of Scientific Research.

John Hazel

QUANTITATIVE, NON-DESTRUCTIVE CALIBRATION OF SCANNED PROBE MICROSCOPE CANTILEVERS

John Hazel, M.S.

Western Michigan University, 1999

Principles of surface science and engineering are applied to determine scanned probe microscope cantilever spring constants. The bi-component gold-ceramic cantilever composition is modeled analytically. Finite element analysis is applied to simulate deflection behavior of the probe tip. Data from experimental determination of resonant frequency are employed to infer material characteristics. Combination of the results from these three procedures is employed to infer material characteristics. Combination of the results from these three procedures is used to produce a spring constant assessment within 10% of actual values. An additional convenient program for assessment of scanning probe microscopy cantilever spring constants is developed for rapid estimation with 20% accuracy.

TABLE OF CONTENTS

Table of Contents--continued

LIST OF TABLES

LIST OF FIGURES

List of Figures - continued

List of Figures - continued

CHAPTER I

INTRODUCTION

The scanning probe microscopy (SPM) technique is a relatively new tool for studying of surface properties on a sub-micron scale (Binning & Quate, 1986). The basic concept of SPM is identical to a profilometer. A sharp point is monitored as it is moved across a sample. The behavior of the tip during this scanning is used to infer characteristics of the surface. Topography is established by recording the height of the tip as it is scanned in a raster pattern across the surface. If the forces on the tip can be detected, many additional parameters may be investigated.

Knowledge and control of the forces applied normal to the surface allows characterizing wear and damage resistance (Tsukruk, Bliznyuk, Hazel & Visser, 1996). Adhesion between the tip and surface can also be useful in characterizing the sample (Tsukruk & Bliznyuk, 1996). Indenting the surface while monitoring the force applied yields data for characterization of sample hardness (Bliznyuk and Hazel, 1998). Knowledge of lateral forces allows friction interactions to be quantified (Tsukruk, Hazel, et al., 1998). These parameters are of practical interest in the micro-scale conditions.

When the scale of measurement is brought near that of molecules and atoms though, many more possibilities are opened. For example a protein molecule can be unfolded by attaching one end to an SPM tip and the other to a sample surface then

moving the tip away from the surface (Reif, Osterhelt, Heymann, & Gaub, 1997). SPM techniques have also been used to experimentally quantify forces of molecular binding and unbinding in biomolecule recognition events (Florin, Moy, & Glaub, 1994).

With calibrated force detection, these molecular forces can be quantified for comparison to theoretical models. The preceding example illustrates the primary strength of SPM. The scales of measurements are very tiny. Typical sizes for the mentioned raster scans are from hundreds of microns down to tens of nanometers. Vertical heights can be measured with resolution of angstroms. The ability to measure vertical and lateral deflections on a sub-nanometer scale and at nanonewton forces has not been fully developed or exploited. The near future holds many rapid advancements in surface science due to the SPM's capabilities to probe at such tiny scales (Overney & Tsukruk, 1998).

Figure 1 shows the general configuration of a representative SPM (Digital Instruments, 1997). The point of interest is the contact between sample and SPM tip. The probe has a radius typically of 20-40nm and in specialized tips has radius as low as 5nm (Digital Instruments Corp, 1995). Contact forces range from a few thousand nanonewtons during indentation experiments down to negative hundreds of nanonewtons when the tip is being pulled away from the surface in adhesion measurements. During raster scanning the forces typically range from a few hundred nanonewtons down to negative tens.

Two essential features are necessary for successful operation of an SPM. The

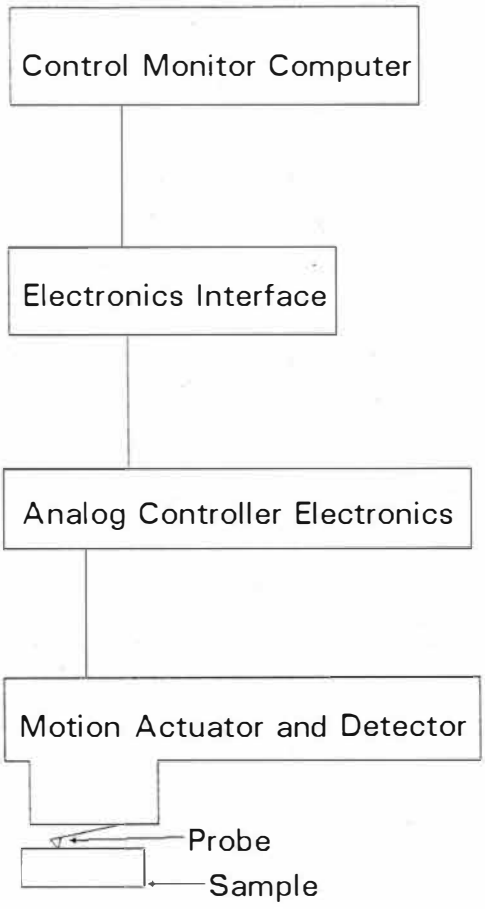

Figure 1. Basic Scanning Probe Microscope Components.

first is precisely controlled motion of the tip-sample positioning. In SPM this positioning is done by electronically controlled peizoelements. Usually there are three separate piezo actuators. Each actuator controls the motion in a single axis. For lateral motions a tube array of four elements is employed with range of motion varying from a few microns to hundreds of microns (Taylor, 1993). Opposite pairs of elements are employed for actuation for both lateral axis motions. In the vertical direction motion is controlled by a single peizo element with the maximum range of motion usually less than ten microns. Figure 2 illustrates the arrangement of the piezo

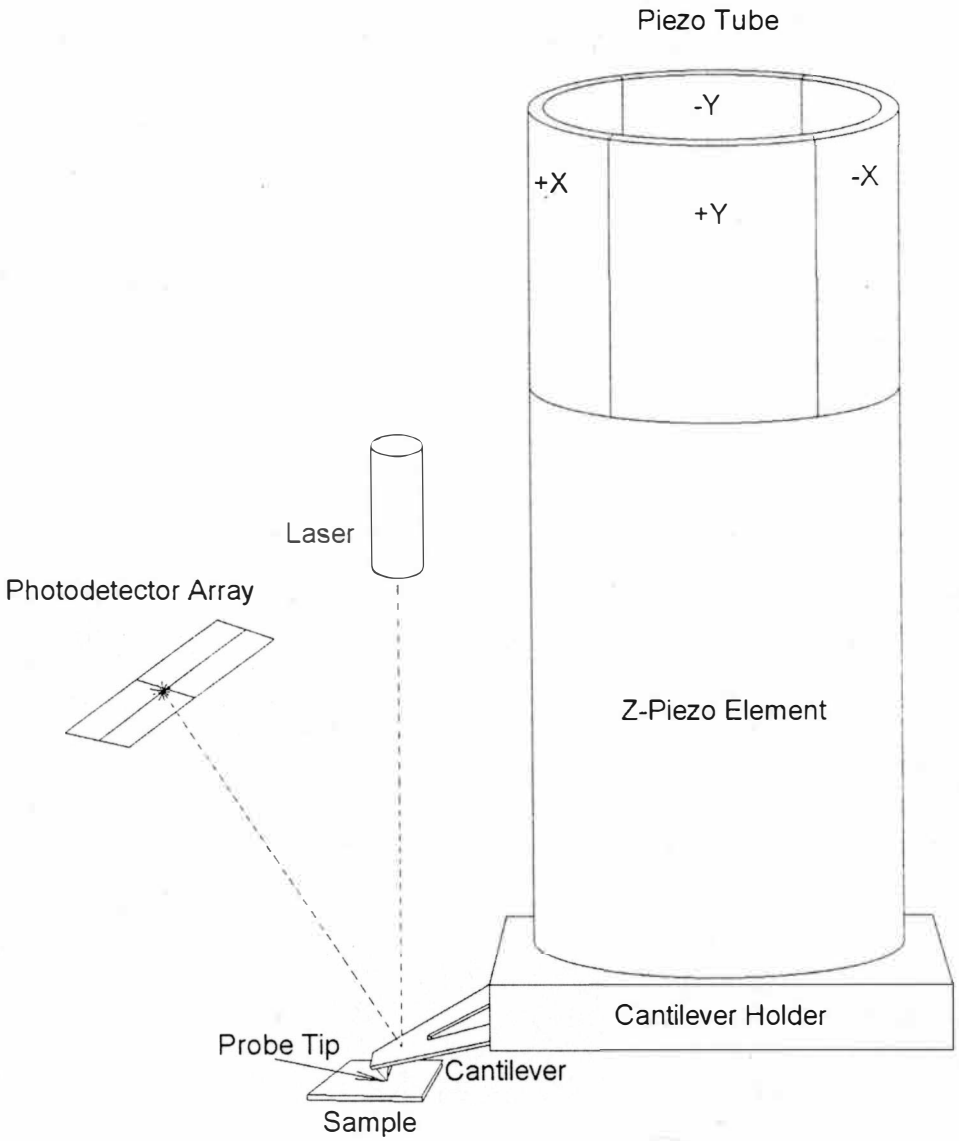

Figure 2. Scanning Probe Microscope.

tube. Generally, the calibration of piezo based motion control is made via scanning standard samples of known geometry and then adjusting internal control parameters. Questions regarding the operation and calibrations of piezoelments are beyond the

scope of this thesis. For discussions of piezoelemets relative to SPM consult (Hues, Draper, & Colton, 1994; Park & Carman, 1997; Tapsen & Green, 1997; Vanlandingham, et al., 1994).

The second critical element in SPM is the detection of tip-sample interaction. Most SPM use a 100-200μm long cantilever to hold the probe. The light lever method is used in the SPM considered here. As shown in Figure 2, a laser beam is focused onto the cantilever. The laser reflects from the cantilever and then falls on a photo-detector array. Forces between the probe tip and sample cause the cantilever to bend which changes the direction of the reflected laser beam and the location of where the laser falls on the photo-detector array. With the change in location of the laser on the photo-detectors comes a change in voltage output from the photo-detectors. This voltage is read by the electronics in the SPM controller to infer the bend of the cantilever. In more recent models of SPM this array has four quadrants to facilitate detection of both bending and twisting of the cantilever.

The detection of lateral forces is performed by detecting the twisting of the cantilever as it traverses the sample. This mode of data collection is termed friction force microscopy (FFM). Collection of the SPM tip torsion deflection data in addition to the usual vertical deflection data can also be used to infer dynamic adhesion response of the tip and surface. Combining the abilities of detecting sample-tip interaction and controlling motion, both at sub nanometer resolution, allows investigation of surface properties at the molecular and atomic scales.

The usual mode of SPM raster scanning operation is to use a feedback loop

that maintains a preset bend in the cantilever. Figure 3 shows a block diagram of the feedback loop (Digital Instruments, 1995). As the scan proceeds the vertical

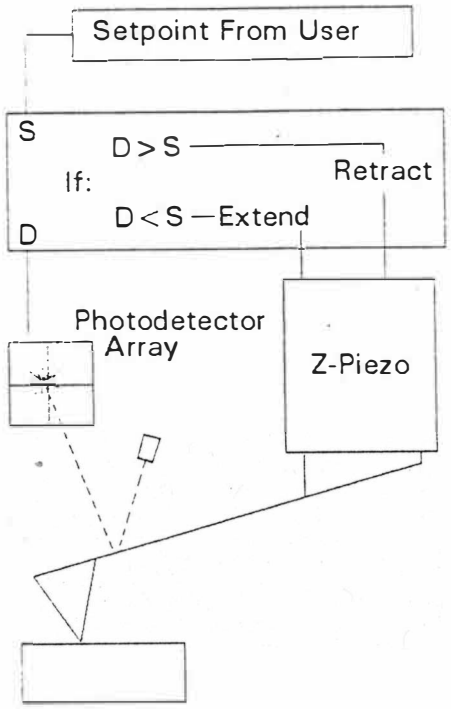

Figure 3. SPM Feedback Loop.

displacement of the tip holder follows the shape of the surface. Because the cantilever deflection is constant, this mode is sometimes called "constant force mode." The height of the surface corresponds to the voltage applied on the Z-piezo element. 3-dimensional topography is then recorded after scaling the applied voltage to height data for each x -y position (pixel) on the raster scan. Figure 4 is an example of such data. With modern SPM the lateral force signal can be recorded simultaneously with height data during a raster scan. The ability to simultaneously collection multiple types of data is becoming an increasingly important feature of SPM based research (Overney & Tsukruk, 1998). This increases the importance of obtaining quantitative

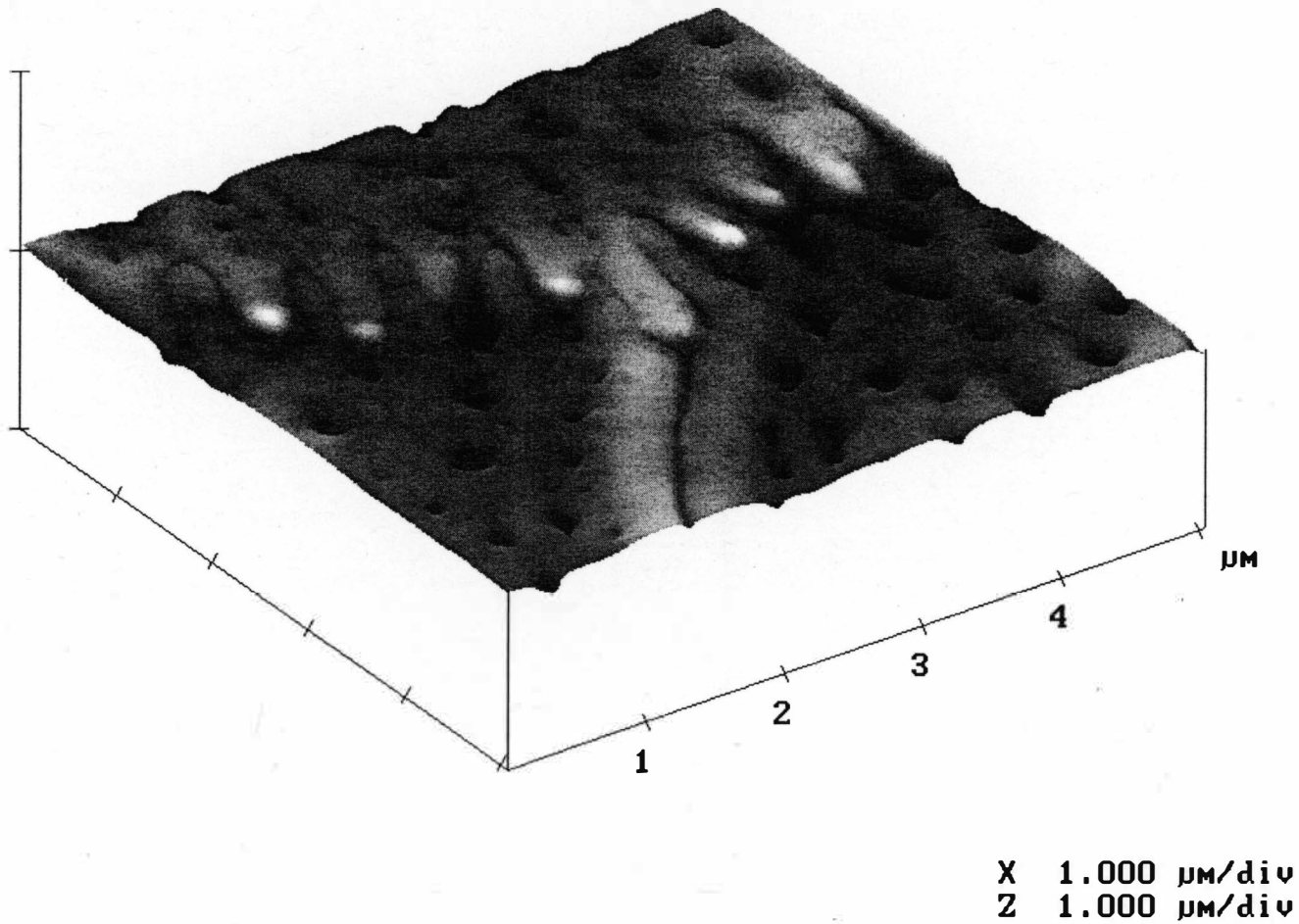

Figure 4. Sample SPM Topographic Data.

Characterization of the surface-probe interaction at a single point of contact is also possible using SPM. The concept of single point analysis by SPM is similar to testing fruit for ripeness at the market. The shopper uses a thumb to indent the surface. The rate of indentation and recovery of the fruit surface is observed and the shopper interprets this indentation data to estimate the material characteristics (ripeness) of the fruit.

SPM provides an electronically controlled, nano-mechanical analog of the fruit shopper's ripeness test. This cantilever deflection vs. holder surface height data is usually presented graphically in a "force-distance curve." Figure 5 shows a typical force-distance curve used for adhesion and indentation data collection.

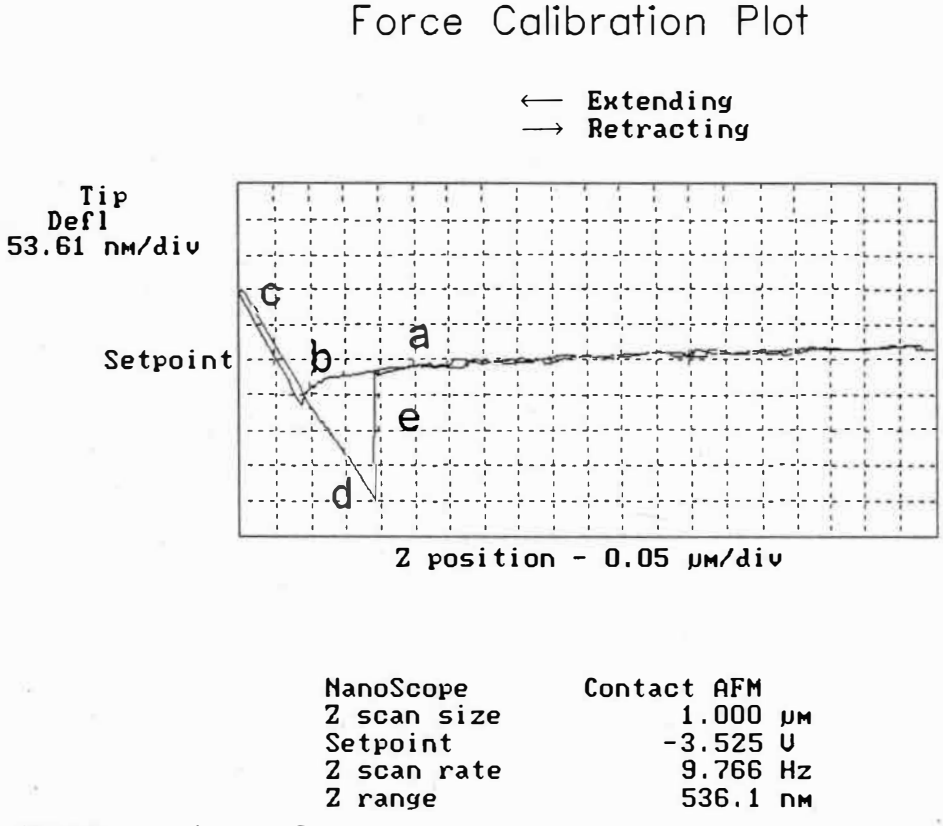

Figure 5. SPM Force-Distance Curve.

This technique, also known as point spectroscopy, uses a fixed x-y position. Refer to corresponding letter marks in Figures 5 and 6. The tip starts off the surface at "a" As the probe tip nears the surface it undergoes a jump to contact due to attractive forces, "b" The cantilever holder continues to move closer to the surfaceuntil a prescribed amount of cantilever deflection "c" is obtained. At that point the holder is moved away from the surface, "d" until reaching the point where spring force exceeds adhesion and the probe snaps away from the surface, "e" The holder and probe returns to the starting height.

Indentation and adhesion data are interpreted by comparing the cantilever deflection with the vertical movement of the cantilever holder. Very hard surfaces deflect the cantilever by an amount equal to the vertical movement of the tip holder. Soft samples allow some indentation of the probe resulting in cantilever deflections that are less than the vertical movement of the holder.

Figures 7a and 7b (Tim Bunning, Wright Labs, Dayton, OH) show a scanning electron micrograph of an SPM microfabricated cantilever with an integrated nano-tip. The process of fabrication starts out with deposition of an etch mask on a silicon surface this mask consists of square holes of the same dimensions as the cantilever tips. An etch process which preferentially removes silicon along the (111) planes is used to produce a pit with a very sharp point at its bottom. This pit is a pyramidal shape with sides that have angles of 55 degrees. After creation of the pit, the etch mask is removed.

Next, the smooth silicon surface with pits is coated with silicon nitride by the

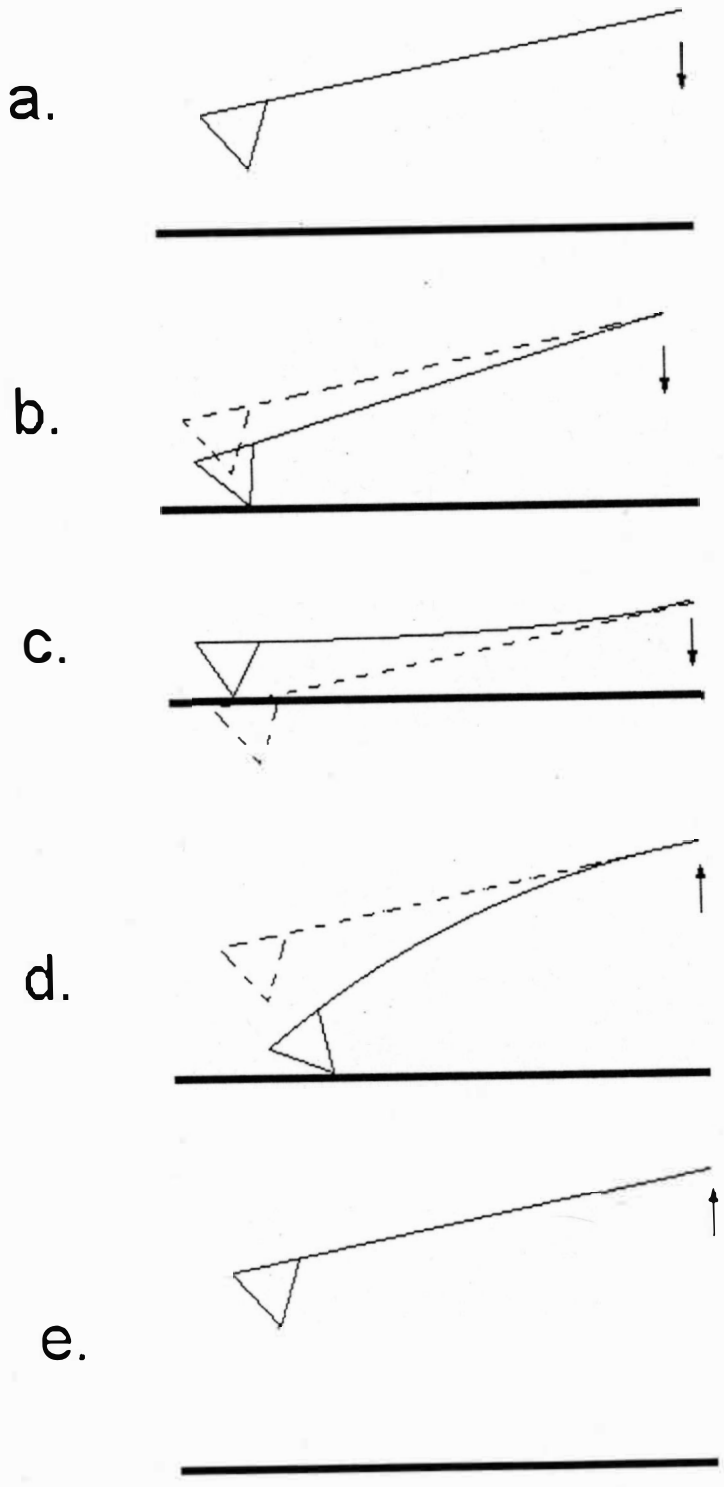

Figure 6. SPM Cantilever During Force-Distance Data Collection.

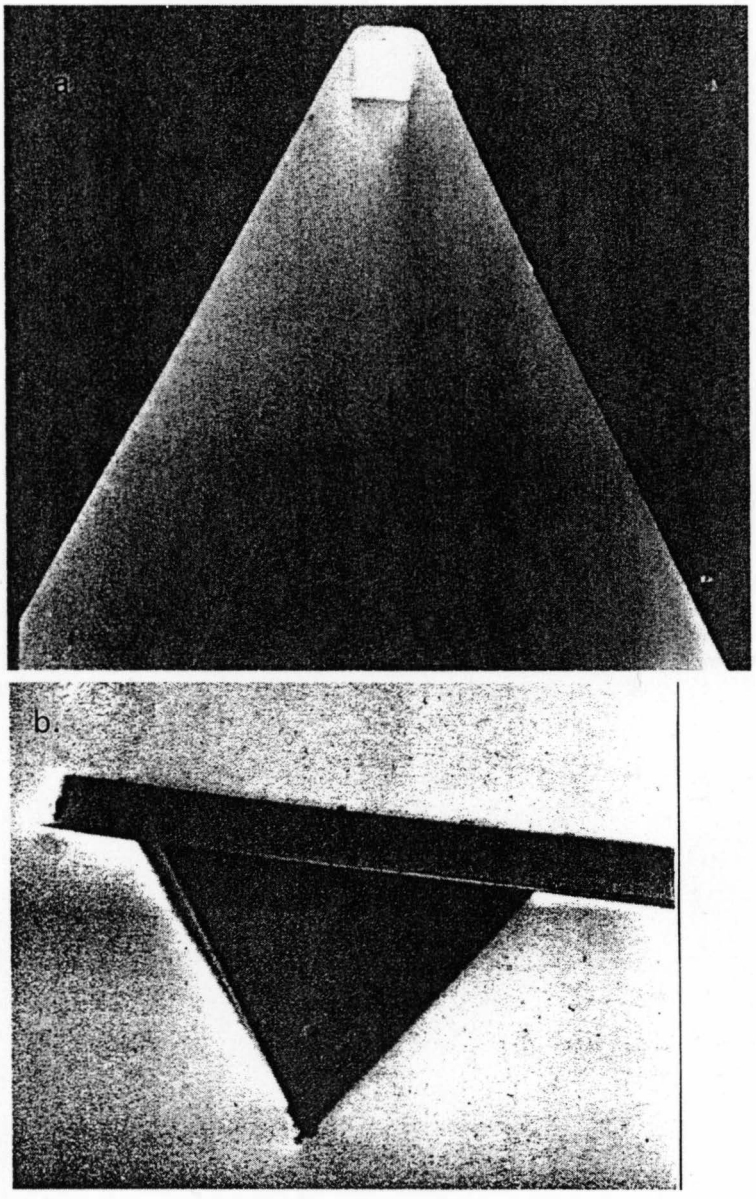

Figure 7. SEM Micrograph of SPM Probe.
Source: Tim Bunning, Wright Labs

chemical vapor deposition (CVD) method. This process coats the silicon surface including the pits. This deposition simultaneously forms the probe tip and cantilever leg material layer. A second etch mask is applied with the cantilever arms and top surface of the substrate delineated. The unprotected silicon nitride is then etched away. After removal of the etch mask the silicon nitride cantilever with pyramidal probe tips formed by the Si3N4 during the CVD are left on the surface of the silicon. Usually this process results in 90%+ of the probe tips being sharp enough to use for scanning. Later steps of fabrication involve the application of more masks and CVD of Si3N4 to produce a chip thick enough to have the mechanical strength needed for mounting in the AFM scanner.

In the photolithography process the lateral dimensions are very well controlled. The current families of microprocessors use dimensional accuracy of better than 0.1μm laterally (Sheats & Smith, 1998). Typical sizes of the most popular V-shaped cantilevers are length of 100 - 200μm, beam width of 10 - 40μm and thickness of0.3 - 2μm. Because the directionality of the etch process is so well controlled by the highly preferred etching direction, the tip height is as well controlled as the lateral dimensions. However maintaining accurate control over the thickness of each deposition is a much more challenging task. It is this lack of control over thickness of the cantilever legs that creates a large portion of the uncertainty in the determination of SPM cantilever spring constants. For contact type cantilevers, which are the focus of this study, overall thickness is 0.5 - 1 μm

The ability to measure vertical and lateral interaction on a sub-nanometer

scale and at nanonewton forces opens exciting perspectives for investigating tribological properties of molecular scale modified surfaces and boundary lubricant films. (Tsukruk, Hazel, et. al., 1998) Boundary lubricant films are molecular scale thickness layers applied to modify surface properties.

The application of these layers to microstructures has far reaching implications for the implementation of tiny machines. Several examples are: molecular friction (Mate, McClelland, Erlandsson, & Chiang, 1987), nanomechanical elastic properties of monolayers (Burnham, Kulik, Gremaud, Gallo, & Oulevey, 1996), frictional properties of micron size domains in mixed Langmuir monolayers (Overney et al., 1992), viscoelastic properties of polymer surfaces (Friedenberg & Mate, 1996; Overney & Tsukruk, 1995) wearing behavior of magnetic discs (Bhushan & Blackman, 1991; Bhushan & Ruan, 1994;Cutiongo, Li, Chung, & Bhatia, 1996; Jiang, Lu, Bogy, & Miyamoto, 1995), nanotribology of boundary lubricants (Meyer et. al., 1992; Tsukruk, Hazel, et al., 1996), and intermolecular interactions of various chemical groups (Green, McDermot, Porter, & Siperko, 1995; Noy, Frisbie, Rozsnyai, Wrighton, & Lieber, 1995).

In the past years, many new observations on tribological properties of various surfaces such as self-assembled monolayers, Langmuir-Blodgett films, spin-coated, and dip-coated films along with a number of polymer surfaces have been reported. The variety of parameters measured and reported are increasing rapidly as the operators of SPM machines develop new techniques and apply them to practical and theoretical problems. Questions of adhesion become very important at tiny scales and

have been shown to be an extremely difficult obstacle to overcome in the fabrication and implementation of microelectromechanical structures (MEMS). Adhesion is an important parameter that SPM addresses.

CHAPTER II

LITERATURE SURVEY

The early versions of SPM did not have provisions for detecting torsional deflection of cantilevers. Without the ability to detect torsional deflections, direct detection of friction force was impossible. The two-element photodiode array was only able to detect the vertical motion of the laser beam due to changes in the slope of the cantilever end. Radmacher, Tillman, Fritz, & Gaub (1992) proposed that frictional data could be collected from a friction caused height artifact. This effect is still an important consideration for experiments that scan in a direction parallel to the cantilever axis.

When the cantilever is scanned in a direction parallel with the axis of the SPM cantilever, a high friction area will have a reduced apparent height when scanning in the forward direction and a increased apparent height when scanning in the reverse direction. Their claim was that the tip of the cantilever delivers a bending torque to the end of the beam as a result of the friction and the tip height. Radmacher, Tillman, Fritz, & Gaub (1992) proposed extraction of friction force data by subtracting height images collected in both forward and reverse directions of scanning. This approach still has some merit. It is also a consideration of artifacts associated with contact mode

scanning in the direction parallel to the cantilever symmetry axis. This point is addressed in the discussion section.

Friction forces became much easier to detect in a qualitative way when four-element SPM photo-detector arrays (Figure 2) became commonplace. While qualitative results are valuable, quantitative measurements allow a much more detailed analysis if quantitative frictional data is available. For example the point damage threshold for loading can be determined in wear analysis experiments (Tsukruk, Hazel et. al., 1996). Several reports of SPM cantilever analysis and calibration have been published recently (Hazel & Tsukruk, 1998). Five different experimental approaches have been explored for estimation of normal (vertical) spring constants, k_n, none of the experimental methods considered estimations of torsional spring constants, k_t, of V-shaped cantilevers.

One experimental approach (Cleveland, Manne, Brocek, & Hansma, 1993) is to measure variation in resonant frequency for the SPM cantilever as it is loaded by high-density micro-spheres (e.g., tungsten). Measurement of resonant frequencies for a given cantilever is a usually a reliable, repeatable, process with modern electronic oscillator standards. This is not the case though in the placement of added mass. Inaccuracy in the sphere placements (within 10 μm) implies a possible error of 20 - 30% in k_n.

The measurement of the diameter is also a significant source of potential error. A one-micron error in the optical measurement of the sphere diameter would

create a 15% error in the calculated mass of a 20 micron sphere. This would translate directly to a 15% error in spring constant.

In addition to the large errors possible, contamination of chemically sensitive tips is possible by the agent used to adhere the added mass to the cantilever. In this method, a standard model of mechanical harmonic oscillation is adopted for the cantilever. This is the classic mass on a spring model represented by the equation:

$$\omega = \frac{1}{2\pi}\sqrt{\frac{K}{m}} \qquad (1)$$

With K being the spring constant at the tip and m being the effective mass at the tip. If the resonant frequency is measured but neither the spring constant nor the mass is known a series of experiments may be performed with a known amount of mass added to the system. Several different amounts of added mass are applied and the resulting resonant frequency is recorded. Extrapolation to a zero added mass gives "effective mass" of the cantilever that can be used for evaluation of spring constants by using the fundamental resonant frequency. Figure 8 shows an example of data from an added mass procedure. This approach does not solve the problem completely because measurement of torsional spring constant, k_t, is not possible with the added mass method.

A second experimental method (Hutter & Bechhoefer, 1993) suggests that by observing the frequency domain response to thermal noise that one can detect the resonant frequency of a cantilever and deduce the spring constant. These methods

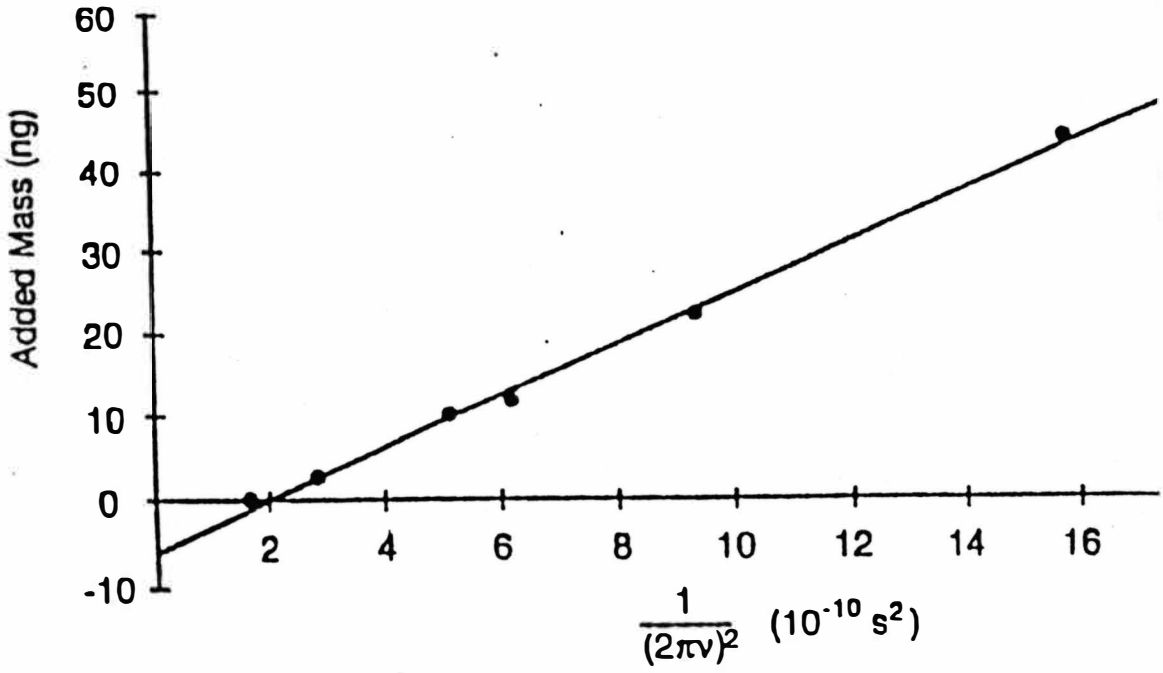

Figure 8. Added Mass Data Example.
Source: Cleveland et. al. (1993)

always require an effective mass to be known beforehand. Calculation of the effective mass of the cantilever for complicated V-shaped cantilevers is not a trivial matter, so this required determination of effective mass tends to reduce the attractiveness of these methods. As in the added mass method the lateral spring constant is not addressed.

The third experimental approach is to determine spring constant by measurement of deflections between a cantilever and a wire spring or a pendulum (Butt et al., 1993; Ruan & Bhushan, 1993). These two schemes are illustrated in Figure 9. The procedure used is to compare deflection of the cantilever with the

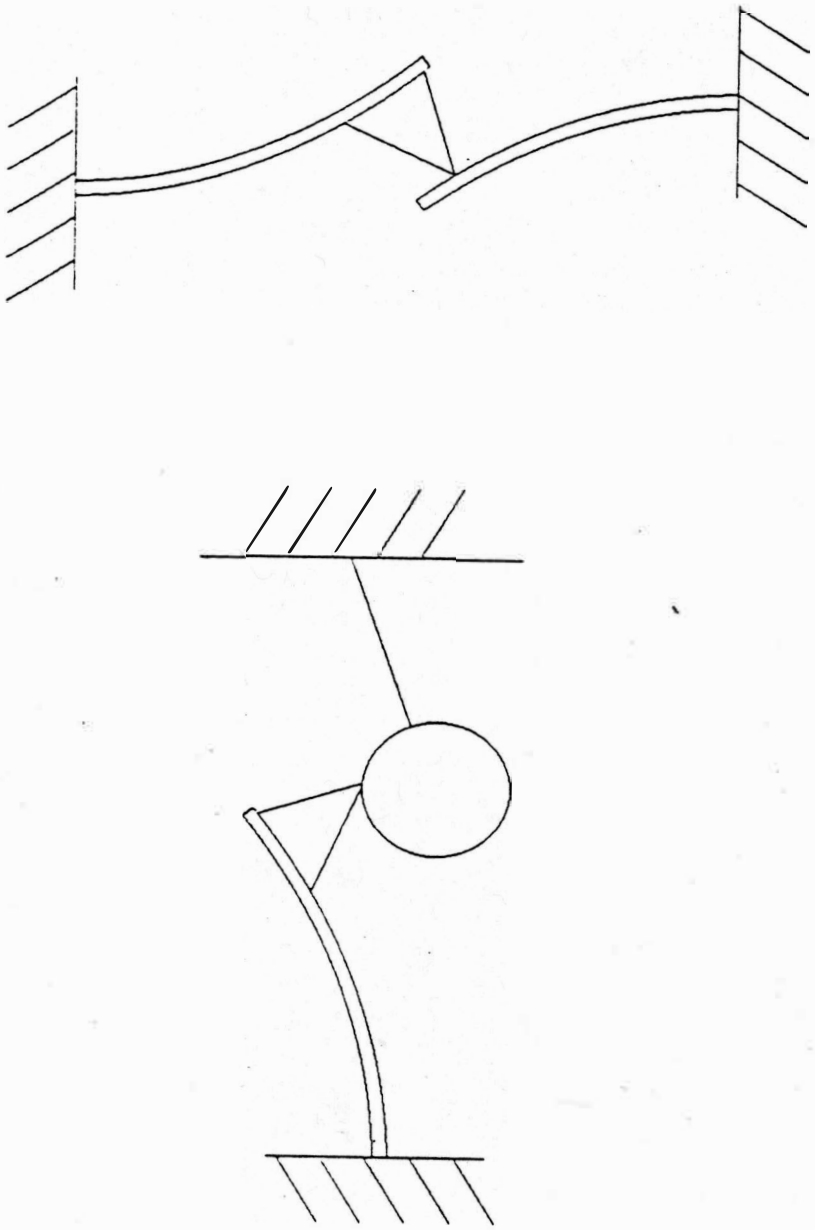

Figure 9. Spring-Spring and Spring-Pendulum Schemes.

deflection against a known spring. The cantilever spring constant is then derived from the deflections and the known spring constant.

$$k_n = \frac{Z_{known}}{Z_{cant}} k_{known} \quad (2)$$

These methods can bring 30 - 50% uncertainty as well. Usually the largest source of error is a noise result from the oscillations of such systems. This is due to the measurement standard being orders of magnitude greater in mass. This much larger mass is a result of the need to make the experimental apparatus' spring constant measurable. The device needs to be of a size that it is large enough to measure the K_n directly.

Reducing the size of the reference cantilever to escape the resonant interference introduces the same difficulty in measuring spring constant as that of the SPM cantilevers. To get very good results with these experimental procedures many small problems must be overcome and large numbers of experiments must be made to achieve a solid statistical foundation for spring constant estimates. As is the case for added mass methods, these efforts yield only data for estimation of the vertical spring constant leaving the lateral stiffness uncalibrated. Calculation of k_t from the known value of k_n requires the following simplification and analytical approximation.

The fourth experimental method incorporated a precision low force balance for the measurement of SPM probe K_n. (Smith & Howard, 1994) The method is to

use a capacitor electrode to sense the position of a rod which has the SPM probe pressed against it. A very small magnet is also attached to the rod. A miniaturized coil is driven by a feedback circuit which senses the rod position. The signal used by the feedback circuit is from the output of the capacitance sensor attached to the previously mentioned electrode. The scale was calibrated using a known cantilever using previously described methods (Butt et. al., 1993; Ruan & Bhushan, 1994). The cantilevers used were also more than an order of magnitude higher K_n than typical contact type SPM probes.

In addition to the purely experimental methods for calibration, three mathematical representation approaches have been proposed. These are intended to avoid the errors in experimental measurements of the small forces involved in deflection of SPM cantilevers.

The parallel beam approximation (PBA) analytic approach (Albrecht, Akamine, Carer, & Quate, 1990) incorporates known solutions of simplified geometry for estimation of both k_n and k_t. Figures 10a and 10c show a V-shaped cantilever with its PBA approximation. In this approach, the cantilever legs are replaced by two parallel beams. This scheme reduces the analysis to well known equations for simple rectangular beam one-component cantilevers where exact solutions for spring constants exist. For the rectangular beam cantilever, simple analytical expressions are known for estimation of vertical and lateral spring constant

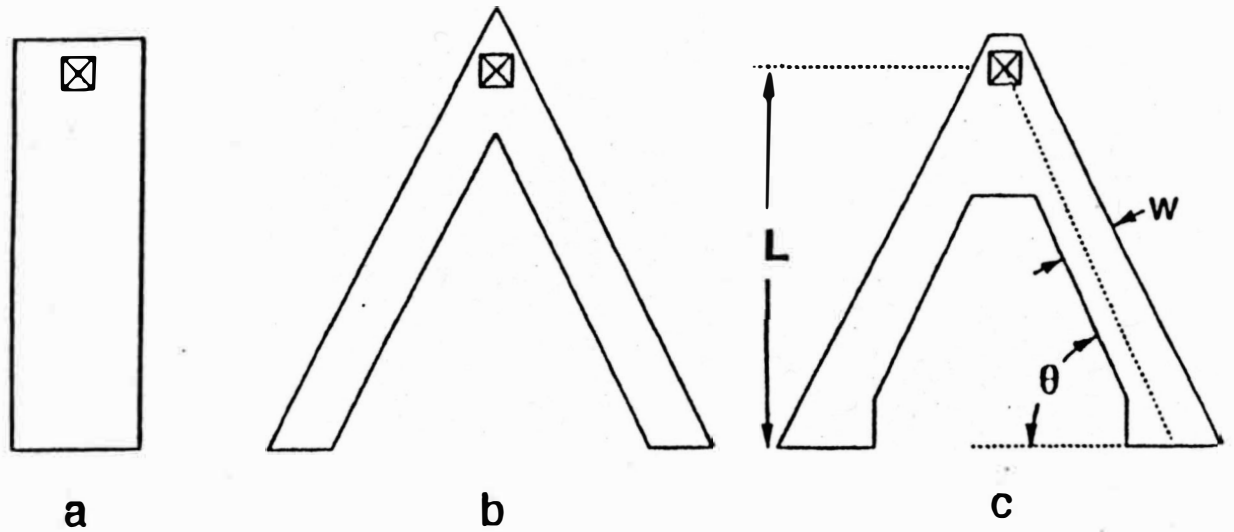

Figure 10. Simplified Geometrical Approximations of SPM Cantilevers.

and their ratio k_t/k_n is:

$$k_n = \frac{Ewt^3}{4L^3} \quad (3)$$

$$k_{lat} = \frac{Ewt^3}{6L(1+\nu)H^2} \quad (4)$$

$$\frac{k_t}{k_n} = \frac{2L^2}{3(1+\nu)} \quad (5)$$

where ν is Poisson's ratio.

The advantage of this expression for experimental measurements is that the knowledge of the ratio k_{lat}/k_n is enough for estimation of friction coefficient, $dF_t/dF_n = (k_{lat}/k_n)\, dx/dy$, where F_t and F_n are torsion and normal forces and dx and dy are lateral and normal cantilever deflections. This approach requires only knowledge of the tip deflections and thereby evaluation of friction coefficient does not depend on uncertainties in cantilever thickness, density, or Young's modulus of the Si_3N_4. Unfortunately the friction coefficient does not remain constant as the normal force is

varied (Tsukruk, Hazel, et. al., 1996) so assessment of critical loading requires some quantification of K_n.

Second, Noy et. al. (1995) proposed an analytical derivation of an idealized triangular approximation of the V-shaped cantilevers for both lateral and normal spring constants. The authors employed a strain energy calculation with standard analytical values for a simple beam with a free end. They expressed total strain energy, **U**, stored in skewed beams as a sum of bending, $\mathbf{U_b}$, and twisting, $\mathbf{U_t}$, components for the beams:

$$U = 2(U_b + U_t) = 2\left(\frac{M^2 L}{2EI} + \frac{\tau^2 L}{2GJ}\right) \qquad (6)$$

where M and τ are bending and twisting components of torque, I and J are the bending and twisting sectional moments for a rectangular beam, L is the Length of the cantilever, E is Young's modulus and G is shear modulus. The bending and twisting components depend on the angle of the cantilever legs and the applied torque.

$$M = \frac{T}{2}\sin\theta \qquad (7)$$

$$\tau = \frac{T}{2}\cos\ \theta \qquad (8)$$

M and τ account for the contribution of both bending and twist due to any torque applied to the cantilever ends. After substitution and taking the second derivative of U, Noy et al received:

$$K_{lat} = \frac{2}{6\cos^2\theta + 3(1+\upsilon)\sin^2\theta}\left(\frac{L}{H}\right)^2 K_n. \qquad (9)$$

Similar to the PBA, formulation of K_{lat} in terms of K_n allows accurate assesment of friction coefficient even in the case of unknown normal sping constant.

Finally, the third mathematical approach relies on computer modeling of the SPM cantilever geometry by a finite element analysis (FEA) (Neumeister & Ducker, 1994; Sader, Larson, Mulvaney, & White, 1995). FEA approximations are produced by creation of a mathematical model of an object's geometry and physical properties. These models are similar to the previous analytic models in the respect that complicated geometry is represented by simple geometric elements. However, the actual geometry of the original item is represented much more precisely due to the very large number of elements used. Figure 11 illustrates the elements used for one

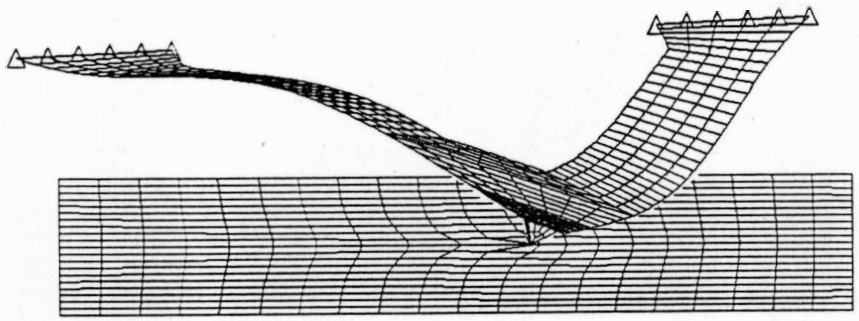

Figure 11. Finite Element Grid for the SPM Cantilever.

of the cantilevers analyzed. This analysis can provide reliable values of spring constants for complicated V-shaped SPM cantilevers when the cantilever material parameters are known.

The previous published FEA studies are valuable however they are all incomplete in their modeling of the composite nature of the SPM cantilevers, ceramics-gold. A gold coating significantly changes the mass and stiffness of the cantilever. These changes are not by identical proportions because gold has much greater density than is Si_3N_4 but is much less stiff. Adding a gold layer of 50 - 60 nm increases cantilever mass by about 40% but only increases the bending stiffness by about 15%. In addition, experimental verification of material properties such as Young's modulus has to be implemented. This is due to the very large percentage of the cantilever material volume that can be under the influence of surface effects. One FEA (Labardi, Allegrini, Salerno, Frediani, & Ascoli, 1994) produced the

unexpected result that the lateral spring constant is reduced by an order of magnitude when there is a normal deflection of the cantilever.

CHAPTER III

PROBLEM STATEMENT

Quantified forces are crucial in the establishment of materials properties from SPM data. Calibration of cantilevers is currently the only path toward quantitative determination of force during SPM scanning. As methods push beyond simple topographical measurements into the materials science of surfaces calibration of scanning forces becomes essential.

Spring parameters of SPM micro-beam structures cannot be easily determined by standard mechanical testing. The typical 100μm cantilever size limits the accessibility of mechanical force detection devices. In addition, for micro-fabricated cantilevers with a nominal thickness below 1 μm, material properties such as Young's modulus, E, can be greatly influenced by surface effects. Variation in stoichiometry renders bulk values grossly in error, which invalidates theoretical estimates. Therefore, the absolute values of normal and lateral spring constants are very uncertain (typically ± 200% of nominal values quoted by a manufacturer). This range of uncertainty is a great hindrance to progress in materials science research via SPM. An accurate method of calibration is needed.

The established methods from the literature all have serious ambiguities. Uncertainty in quantification of spring constants or the lack of an assessment of lateral spring constant are the two most serious problems of previous methods. To

address these issues a new more accurate assessment of spring constants is needed. The new technique should provide quantitative calibration of both lateral and normal spring constants of SPM cantilevers to make quantitative measurements of material properties.

The goal of this work is to develop experimental procedures for calibrating SPM cantilevers as accurately as possible using commonly available SPM research lab resources.

The proposed method for achieving this goal joins the methods of resonant frequency analysis, FEA modeling and analytic approximation. They can be combined into a complimentary package that address the geometrical and materials property estimation shortcomings of the previous calibration attempts. The cantilever Si_3N_4 and Au layers are transformed analytically into an equivalent single composite layer. This single layer is then modeled by FEA using measured geometric parameters from the actual cantilevers of interest.

After identification of important parameters, a sensitivity analysis revealed a set of trends that were incorporated into easy to use calibration plots. A calibration plot is presented for estimation of spring constants from resonant frequency measurements for the cases of known gold thickness and a less precise one for faster rough estimate by resonance frequency data alone. FEA modeling results are compared to several analytic estimates. A new analytical solution for the ratio of lateral to normal spring constants is provided. This relation of K_n to K_{lat} is nearly

independent of cantilever material properties and therefore allows quick, fairly accurate measurement of friction coefficient.

CHAPTER IV

ANALYTICAL TREATMENT OF COMPOSITE BEAMS

Advances in microlithography technology have continuously driven the electronics industry toward smaller devices. Silicon and silicon nitride are often employed as construction materials for these devices. Eventually researchers have made micro mechanical structures including SPM probe-cantilevers.

Although Si_3N_4 is very suitable for constructing microstructures it is transparent. Since the cantilever surface is used to reflect laser light, a gold coating is applied to the cantilever. The presence of the gold overlay significantly changes the mass and stiffness of the SPM cantilever. For a 0.05μm Au layer on a 0.55μm cantilever as measured in our case, 40% of the total mass and 15% of the stiffness was due to Au . The change in stiffness due to the Au layer can be determined by analysis of the equivalent transformed section that provides a much more accurate approach than the simple linear approximations elaborated in the literature (Sader, 1993). Figure 12 shows the error implicit in linear weighting vs. correct analytical derivation of section modulus. The detailed derivation of the equivalent section modulus of a bi-component section is given in Appendix A. In the section transformation method used here, the composite section is reduced to a single material section with identical bending stiffness and homogeneous Young's modulus equal to that of the Si_3N_4 (Figure 13). The resulting geometry is a pair of joined

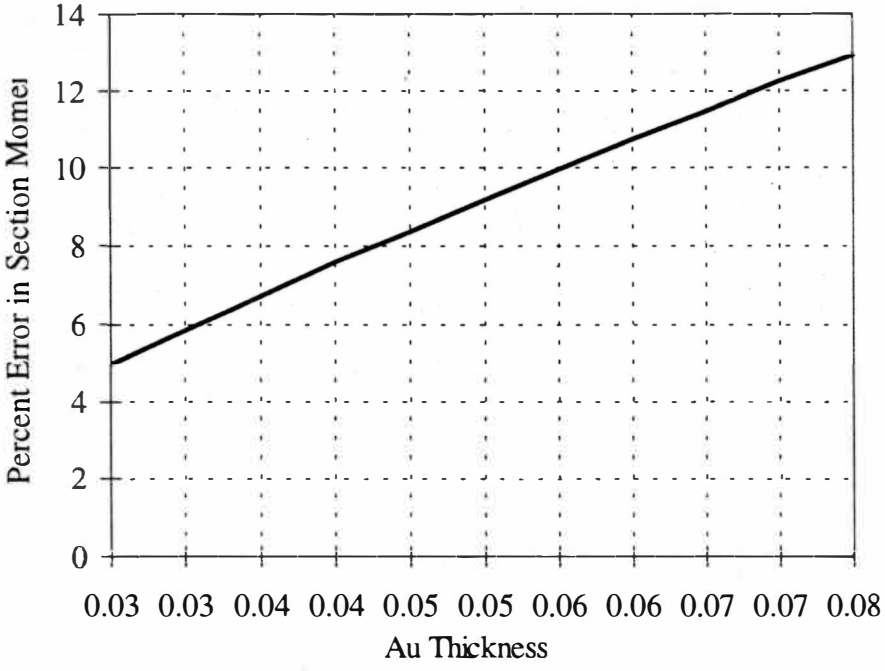

Figure 12. Error in Linear Approximation.

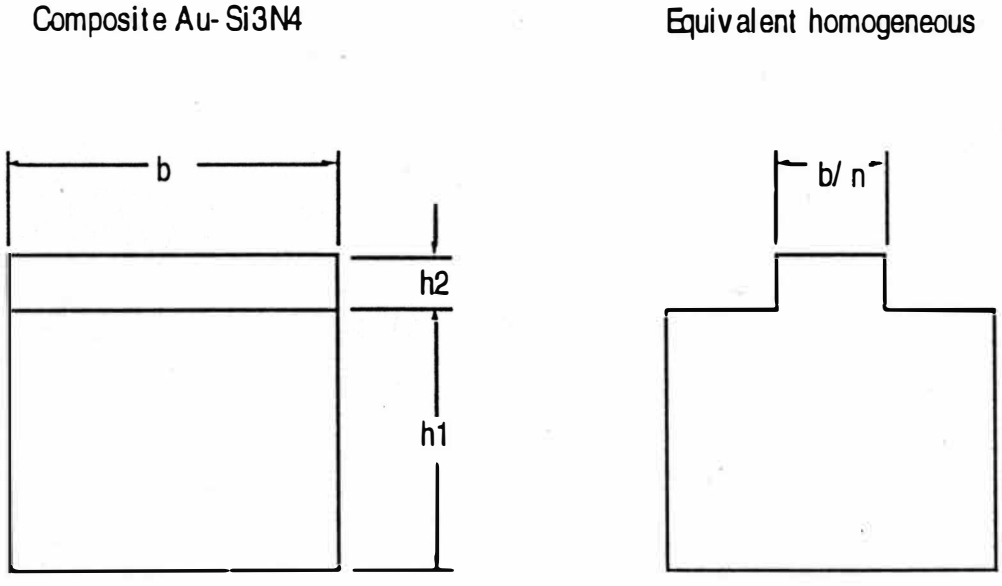

Figure 13. Section Transformation.

rectangular sections whose section modulus can be determined by employment of the parallel axis theorem.

For a composite section with a width b and a Si_3N_4 thickness of h_1 and Au layer of thickness h_2 the equivalent transformed section will have the width of the portion representing the Au reduced by a factor of $n = \frac{E_{Au}}{E_{Si_3N_4}}$ (see Figure 13 for designations). This width reduction is valid for calculation of the section moment about the horizontal axis only. The transformation to compensate for bending around the vertical axis would require a reduction not in width but thickness of the Au layer. For the torsional loading, since the ratio of width to thickness of the cantilevers is high the effective thickness of the cantilever having section moment about the horizontal axis was used. For the cantilevers studied here this simplification introduces a very small systematic error of less than 0.2% in the calculated ratio of normal to lateral spring constant.

The thickness of Si_3N_4 and Au layers are h_1 and h_2, and the width of Si_3N_4 remains unchanged. Using standard practice, the centroid location, y_c, of the transformed section can be determined by:

$$y_c = \frac{A_1 y_1 + A_2 y_2}{A_1 + A_2} \qquad (10)$$

where A_1 and A_2 are the areas of the rectangular sections and y_1 and y_2 are the locations the centroids of the individual areas. The composite section moment I_{comp}, is:

$$I_{comp}=I_1+A_1(y_c-y_1)^2+I_2+A_2(y_c-y_2)^2 \qquad (11)$$

where $I_1=\frac{1}{12}bh_1^3$ and $I_2=\frac{1}{12}nbh_2^3$. The actual cantilever bending stiffness EI then has the following relationship to E_{SiN} and I_{comp}: E I = E_{SiN} I_{comp}. If b is set to unity the composite cantilever then can be represented by FEA using homogeneous plate element of thickness: h_{eq} = $(12I)^{1/3}$. Using this thickness and adjusting the Young's modulus in the FEA simulation to reproduce the experimental resonance frequency yields the actual young's modulus of the Si_3N_4. Alternately, an expression for effective Young's modulus, E_{eff}, based on total actual cantilever thickness $h_1 + h_2$ is:

$$\frac{E_{eff}(h_1+h_2)^3}{12}=E_{SiN}I_{comp} \qquad (12)$$

The expression (12) gives different results for E_{eff} as compared to the standard linear combination:

$$E_{eff} = \frac{h_1 E_{SiN} + h_2 E_{Au}}{h_1 + h_2} \quad (13)$$

Actual deviations of linear estimations of bending stiffness as shown in Figure 12 are as high as 10% overestimation for our cantilevers and are even higher for cantilevers with a thicker gold overlay.

The next important parameter is composite beam effective density, p_{comp}, which is calculated from data for ceramic and gold materials according to the known relationship:

$$\rho_{comp} = \frac{\rho_{Au} h_2 + \rho_{Si3N4} h_1}{h_2 + h_1} \quad (14)$$

Effective density of composite ceramic-gold cantilevers is 4.30 g/cm^3 as estimated from experimental parameters for our cantilevers and p_{Au} = 19.6 g/cm^3, p_{SiN} = 3.0 g/cm^3. The plate elements in FEA analysis were given a density scaled by the ratio of actual cantilever thickness to the plate element thickness to account for the total mass of Au and Si_3N_4. The relationships between I_{comp}, spring constant, and resonant frequency for composite cantilevers are:

$$f_o = C_1 \left(\frac{I_{comp} E_{SiN}}{M_{comp}} \right)^{\frac{1}{2}} \qquad (15)$$

$$k_n = C_2 I_{comp} E_{SiN} \qquad (16)$$

where M_{comp} is effective composite cantilever mass, C_1 and C_2 are geometrical coefficients determined by actual cantilever shape. The results of FEA modeling can be used for finding numerical values for coefficients C_1 and C_2.

Mechanical behavior of the SPM cantilevers depends upon a number of geometrical and materials parameters and is usually analyzed using the known relationships for homogeneous beams as summarized below. Normal spring constant, k_n, of a one-component cantilever can be expressed in the form:

$$k_n = C_3 E h^3 \qquad (17)$$

where C_3 is a geometrical factor determined by cantilever shape ($C_3 = w / 4L^3$ for a rectangular beam), h is overall thickness, w is width, and L is total length.

Resonant frequency, f_o, represents a fundamental experimental parameter which can be easily measured in the modern SPMs. Resonant frequency is related to cantilever geometrical and mechanical parameters as:

$$f_o = \frac{\left(\frac{k_n}{m}\right)^{\frac{1}{2}}}{2\pi} = \frac{C_4 w^{\frac{1}{2}} h E^{\frac{1}{2}}}{\rho^3} \qquad (18)$$

where C_4 is a geometrical factor ($C_4 = 1 / (2\pi L^2)$ for a rectangular beam) and • is material density. A combination of equations. (16) and (17) results in a new relationship:

$$k_n = C_5 \rho^{\frac{3}{2}} E^{\frac{-1}{2}} f_0^3 \qquad (19)$$

where C_5 is a geometrical factor ($C_5 = 2\pi^3 w L^3$ for a rectangular beam). Equations (16 - 18) are derived for homogeneous beams and believed to be a good approximation for homogeneous beams. However, the composite nature of actual Si_3N_4/Au cantilevers reveals itself in fundamental differences of their mechanical behavior such as changes of k (f_o) behavior as will be demonstrated below.

CHAPTER V

GEOMETRY OF V-SHAPED CANTILEVERS

Lateral cantilever dimensions were measured by scaling high magnification optical microphotographs of actual cantilevers made concurrently with a 10μm calibration grid. We made extensive simulations for short (100μm) and long (200μm) cantilevers. Overall thickness, tip location, height, and lateral sizes were measured using high resolution, low voltage scanning electron micrographs as shown in Figure 7. The gold film thickness was found from SPM images on top of cantilever chips with partially removed gold overlay. The gold overlay was removed by applying a double-sided adhesive tape which resulted in pulling out large (many hundreds of microns) areas. The surface of both gold layer and underlying silicon nitride was studied by SPM to assure homogeneous composition and morphology of both surfaces. Bearing surface analysis was used to calculate gold layer thickness from height histograms. These measurements were made by Dale Visser in our lab.

The gold coating thickness for the batch of cantilevers in this study was 47 ±7 nm. Cantilevers in our particular wafer had length and width listed in Table 1, an overall thickness, h, of 0.60 ± 0.01 μm, and tip height (including half of cantilever thickness), H, of 3.8 ±0.1μm. Thickness and lateral geometrical dimensions measured on several long and short cantilevers randomly selected within the same wafer have been shown to be quite uniform (± 1-3%). In addition, resonant frequency

measured for several dozens of cantilevers was virtually constant with deviations not higher ±1.5%.

Table 1

Cantilever Dimensions

	"short," nominal length 100 μm	"long," nominal length 200 μm
E_{comp}, (composite), GPa	172	185
E, (Si_3Ni_4), GPa	197	214
f_o, (air), KHz	52.1	18.0
k_n, normal, N/m (FEA)	0.235	0.059
K_t, torsional, nNm/rad	1.71	1.25
K_{lat}, lateral, N/m	118	83.8
length, μm	108.4	184.3
width, μm	15.6	20.6
tip height, μm	3.8	3.8
θ angle degrees,	67	62.5

CHAPTER VI

FEA MODELING

Geometrical dimensions of the FEA model correspond to popular V-shaped cantilevers shown in Table 1. These cantilevers were purchased from Digital Instruments Inc, Santa Barbara. The FEA simulation of the cantilever was carried out using plate elements in the ALGOR® FEA software package (Algor Interactive System, Inc., 1991). The nearly 2-D geometry of SPM cantilevers lend themselves well to modeling by plate elements. The number of elements (Figure 14) varied

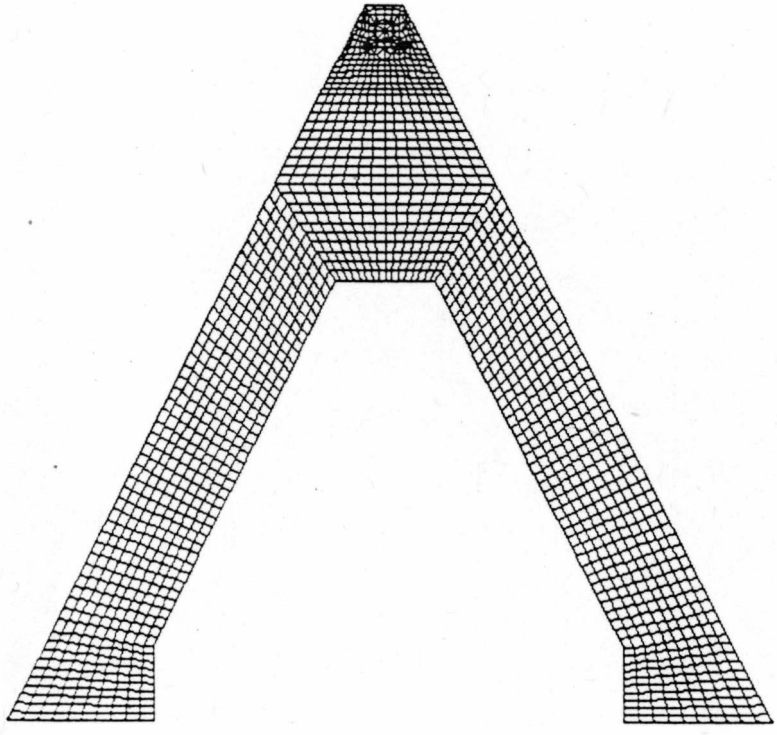

Figure 14. Fine Finite Element Grid.

between about 200 and 2000 in different versions of the cantilever models. A model with 530 elements was selected for the majority of modeling. Choosing the lower number of elements allowed more reasonable execution time of 30-60 minutes for the 486 class and P-60 computers available at the time of the modeling. Grid size independence for the FEA model was verified by comparing results of otherwise identical cantilever models with different number of elements. Models with 530 elements showed 0.4% different results for spring constant compared to 1440 element models.

Figure 15 shows stress distribution for normal deflection as calculated by FEA. This is a plot of the cantilever undergoing vertical forces only. This plot illustrates the shortcomings of the parallel beam approximations. Notice the concentration of stress in the middle points where leg of the cantilever joins the other. This concentration of stress shows the tendency for a beam to bend along its weakest axis being interfered with by the connected opposite beams restraining the beams ability to twist during deformation relative to the other non parallel leg. There are similar concentrations of stress at the attachment point where the legs join the supporting Si_3N_4 substrate.

This is the complementary torque reaction to the restriction of twisting at the joining of the legs near the probe tip. The second in the series, Figure 16 is the stress calculation of the reaction to lateral forces. Clearly shown is the concentration at the point where the legs join near the tip. This is where the simplified geometry analytical expressions fail to capture the important details of the actual geometry. Lastly the

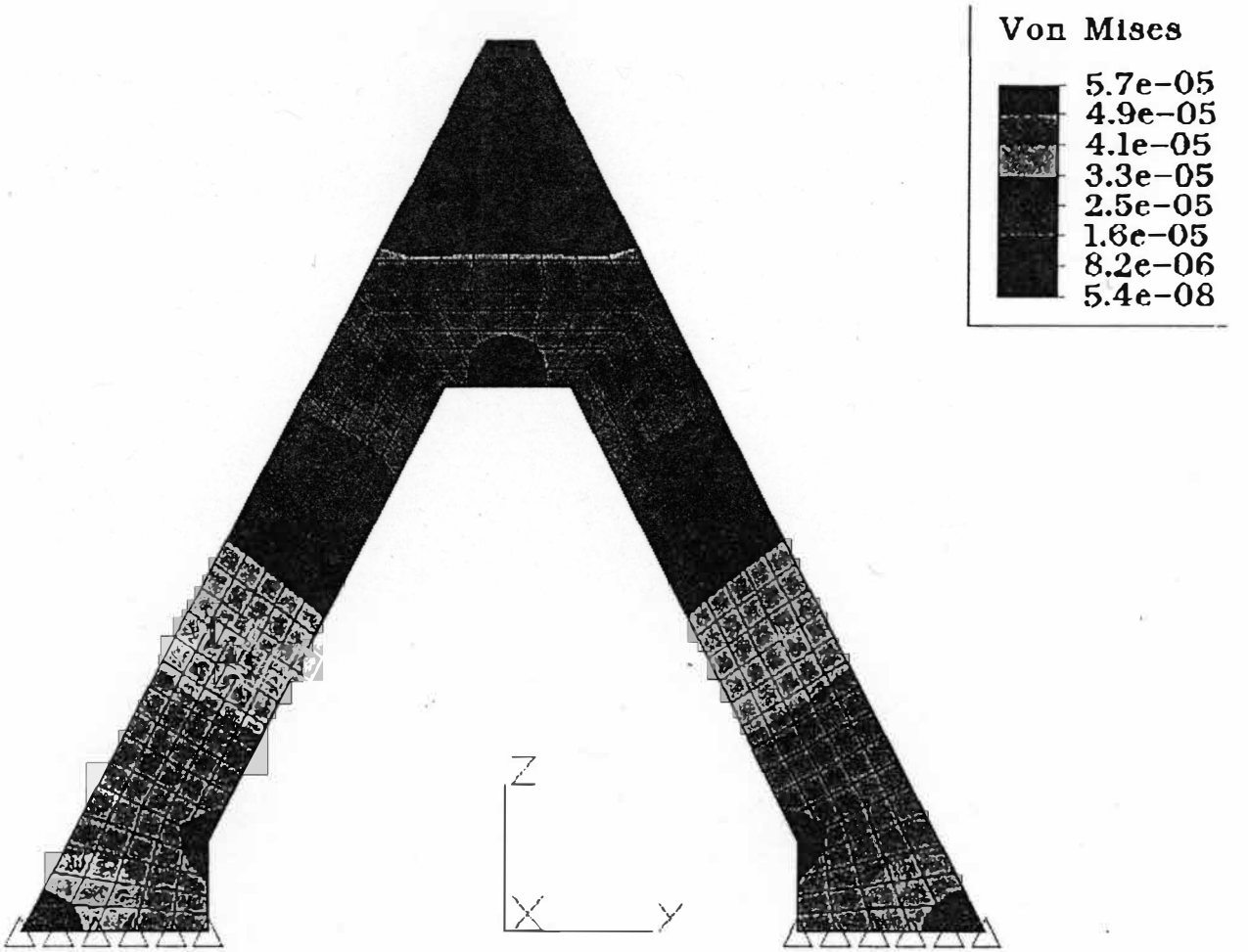

Figure 15. Stress During Application of Normal Force.

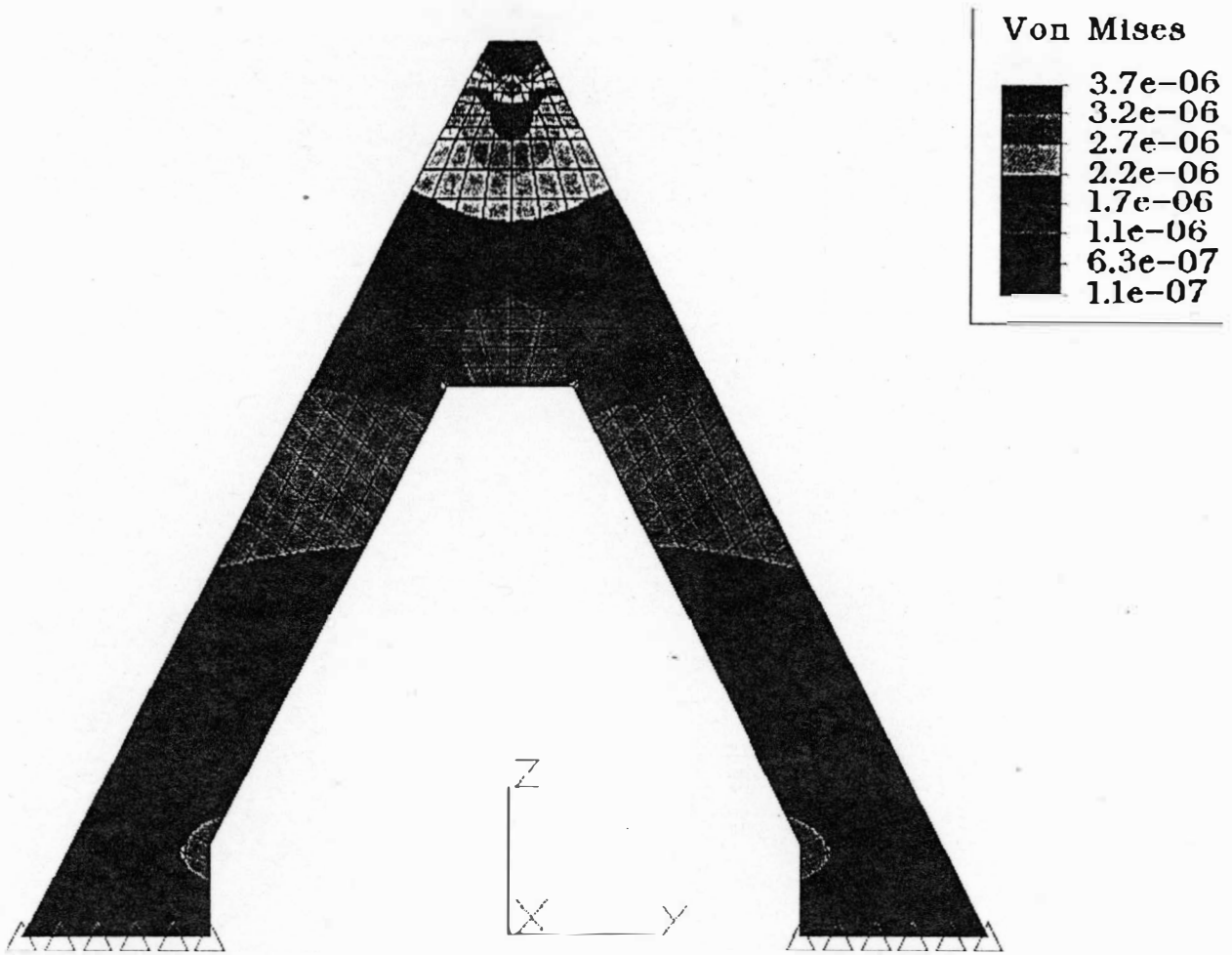

Figure 16. Stress During Application of Lateral Force.

third FEA stress plot, Figure 17, shows simultaneous and equal forces applied both laterally and vertically. This illustrates the relative stress concentrations of the two force directions.

It should be remembered though that the typical friction forces are around 0.1 of the normal force (Tsukruk, et al., 1998). In practice the relative contributions of the lateral forces will be smaller by an order of magnitude. This along with the two orders larger lateral spring constant compared to the normal spring constant indicate that the torsion of the tip end is indeed small. The range of deflections is very far below the threshold where considerations of buckling need to be taken.

Tests of the ratio of lateral deflections and torsion contributions to the total lateral deflections showed only a small contribution of the total for the stretching of the cantilever legs. Weak dependence on variation of Poisson's ratio was also demonstrated for the FEA model. Initially, Young's modulus and density were set to values available in the literature. These values were then adjusted until the calculated resonant frequency was equal to the experimentally determined one as described below.

After the above tests came the calculation of the fundamental resonant frequency, f_0. This process is performed by calculation of the Eigen vector of the representative array that defines the FEA model. AFM cantilevers undergo billions or trillions of oscillations before failure. This indicates that the cantilever material is working in its linear stress and strain range of deformation. Appropriately then, only linear analysis was chosen for the FEA.

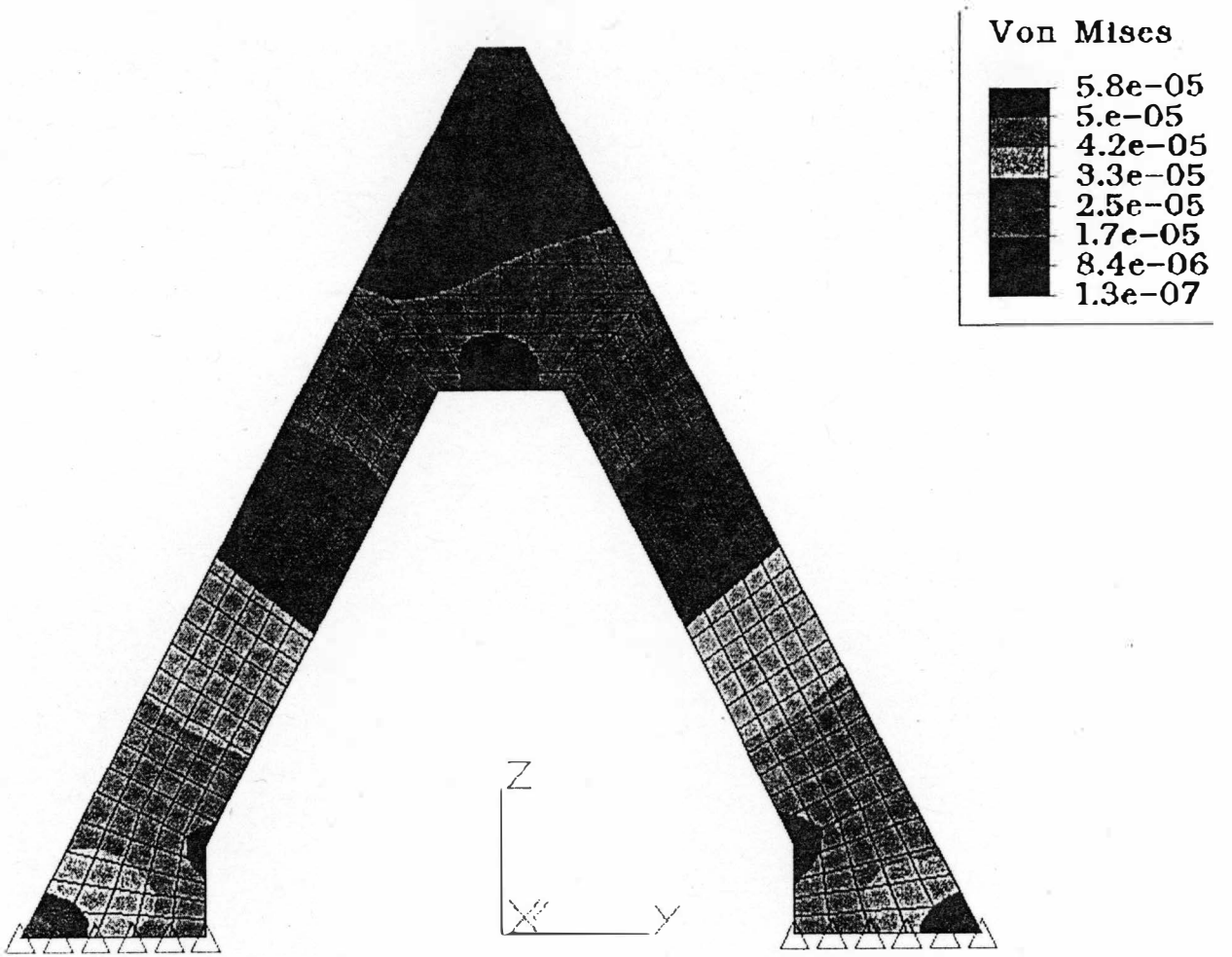

Figure 17. Combined Normal and Lateral Forces.

CHAPTER VII

RESONANT FREQUENCY MEASUREMENTS

The resonant frequencies were measured by Nanoscope IIIA tuning mode. Tuning mode is a software feature used to find the resonant frequency of the installed cantilever in preparation for non-contact scanning by SPM. The cantilever is excited with a small auxiliary peizo-ceramic element that is integral to the tip holder. Initially a frequency sweep is produced to drive the cantilever while observing the amplitude response of the photo-detector array in response to the oscillation amplitude of the cantilever. The single beam cantilevers usually show a first mode peak with Q factor of about 100 in the response curve generated during this drive frequency sweep.

V-shaped cantilevers investigated here are much more complicated in their response. Occasionally, a single resonant peak with high Q will appear but more often several peaks are observed (Figure 18a). These must be tested to discover whether the increased response in photo-detector output is actually a result of a cantilever resonance.

One very helpful method for sorting out the resonance of the tip holder and piezo-electric stack from the cantilever resonance is to move the laser spot away from its normal position at the end of the cantilever to a location on the supporting chip. This chip receives gold coating at the same time the cantilever is coated so the reflective coating is available on the chip surface also. Figure 18b shows the photo-

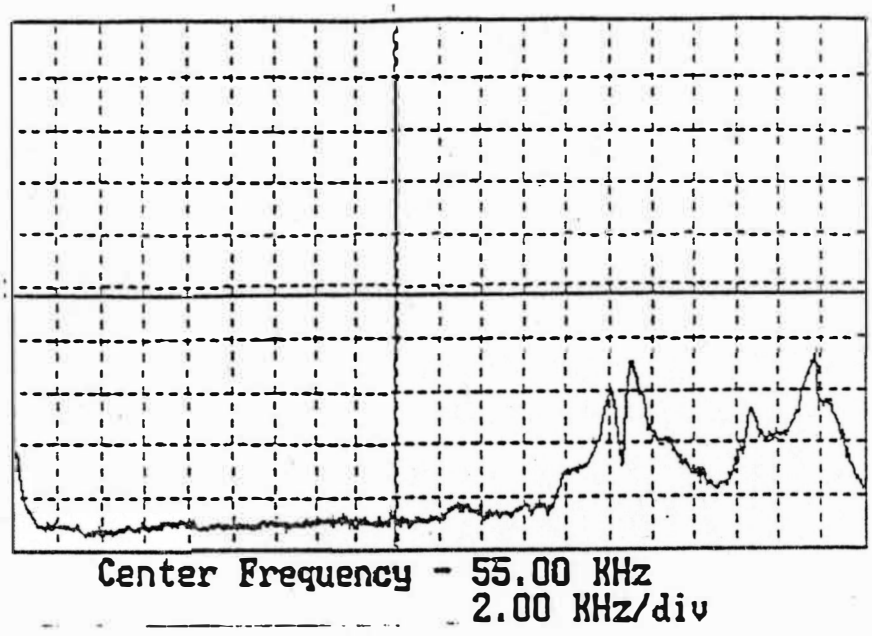

a.

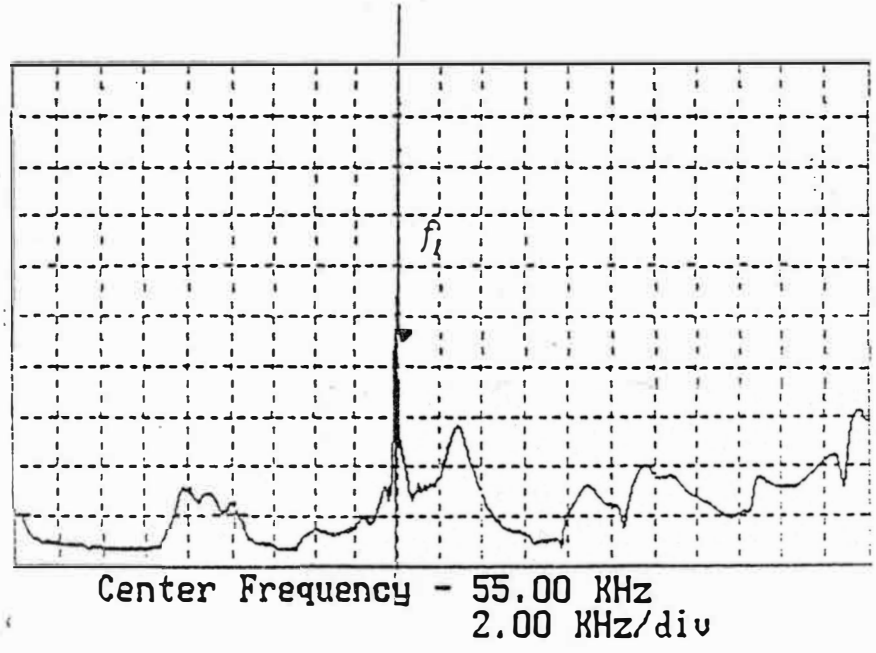

b.

Figure 18. Drive Frequency Response. (Vertical Axis: photodetector signal, Horizontal Axis: drive frequency)

detector response to the frequency sweep with the laser spot of the cantilever. The results can be compared with the sweep captured with the laser spot on the cantilever tip. Most of the peaks will appear in both results and by means of this comparison the peaks due to cantilever vibration may be identified.

The experimentally determined cantilever resonant peaks were also supported by comparing the calculated $2^{nd}$and 3^{rd} resonance with corresponding peaks in the frequency response graph. Initially these frequencies were very different than the measured ones but their proportional jumps in resonance as the first several modes were excited correspond to experimentally determined ones quite well. For example the match of the "long narrow" cantilever fundamental and first two bending harmonics were 19.1kHz, 98.3kHz, and 110.2kHz. After deriving the correct Young's modulus the calculated and measured values were within 2%. Similar results were obtained with the short narrow cantilevers.

CHAPTER VIII

SPRING CONSTANTS AND YOUNG'S MODULUS

After completion of the FEA model and the resonant frequency measurements, the FEA calculated resonant frequency is compared with experimental measurements of f_o. Next, Young's modulus of the FEA model was adjusted to match the experimental resonant frequency. The density of silicon nitride used was 3.0 g/cm^3 as reported for chemical vapor deposited silicon nitride materials. The current results give an effective Young's modulus of 172 ± 12 GPa and 185 ± 13 GPa for short and long cantilevers (Table 1). For Si_3N_4 materials itself we obtained 197 GPa and 214 GPa, respectively. These values are very close to the middle point of the range from 135 to 305 GPa reported for different stoichiometry of Si_3N_4 and are within the experimentally measured moduli for the SPM cantilevers (130 - 240 GPa range).

Reproducibility of the results for mechanical parameters is within 7% for cantilevers from the same wafer for 5 different cantilevers in sets of 5 - 10 independent measurements per cantilever. The actual precision of the measurements for a particular cantilever is much higher (~1%). The difference in Young's modulus for the two types of cantilevers falls within a 7% deviation range which can be attributed to variations in the air damping. Actual measured resonant frequency shifts due to the effect of air were available only for the short narrow cantilevers.

After the Young's modulus and density were established for Si_3N_4, normal and lateral loads were applied to the cantilever FEA model. Using the modeled forces and deflections Kn and Kt were derived.

To test the validity of PBA and ideal triangular shape simplifications (Figures 14b and 14c) models of these idealized geometries were included in the FEA analysis. We also tested our FEA model against the analytical solution for the PBA model. For our cantilever, the FEA model gives vertical spring constant 0.259 N/m that is very close to the exact solution for PBA That gives k_n = 0.256 N/m (Beer, 1981; Senden & Ducker, 1994).

Analytical PBA solutions used for the evaluation of triangular cantilevers give k_n from 0.173 to 0.256 N/m that is within 25% deviation from FEA results for either ideal triangular or real V-shaped cantilevers. Therefore, different PBA solutions can be used for the estimation of normal constant for V-shaped cantilever within 25% accuracy. The best fit for V-shaped cantilevers is achieved by the Butt et al. (1993) approximation although for a simple triangular geometry, the Albrecht et al.(1992) solution is the closest. An equation by Sader et al. (1995) underestimates normal spring constant for composite cantilevers by about 40%.

Analytical estimation of spring constant ratio, k_{lat}/k_n, for triangular cantilevers can be done according to an expression proposed recently by Noy, Vezenov & Lieber, (1997). The authors employed a strain energy calculation with standard analytical values for a simple beam with a free end. They expressed a total strain

energy stored in two skewed beams, **U**, as a sum of bending, $\mathbf{U_b}$, and twisting, $\mathbf{U_t}$, components for a single beam:

$$U = 2(U_b + U_t) = 2\left(\frac{M^2 L}{2EI} + \frac{\tau^2 L}{2GJ}\right) \quad (20)$$

This expression, which leads to the result presented in equation (9), gives the underestimated ratio $k_t/k_n = 5.74 \times 10^{-9}$ as was concluded from comparison with FEA simulations (Table 2). This torsion constant is about 45% less as compared to the full

Table 2

Spring Constant Calculation Comparison

	K_n, N/m	K_t, Nm/rad	K_t/k_n, M^2/rad	K_{lat}, N/m
PBA (Butt et al., 1993)	0.256			
PBA (Albrecht et al., 1990)	0.205			
PBA (Sader, 1995)	0.173			
Triangle (Noy et al., 1995)	0.256	1.47E-09	5.47E-09	111
Triangle*	0.256	1.77E-09	6.90E-09	123
PBA-FEA	0.259	1.87E-09	7.22E-09	130
Triangle-FEA	0.216	1.70E-09	7.76E-09	118
V shaped-FEA	0.235	1.71E-09	7.28E-09	118

FEA solution. The reason for this underestimation is that the influence of the connection between the two arms has not been accounted for in the original derivation. This derivation takes bending strain-energy as $\frac{M^2 L}{2EI}$ which is the value

for a beam with one fixed and one free end. In reality, however, the bending component of twist in the separated cantilever arms would cause one arm to move down and the other arm to move up. Figures 19a-c illustrate these modes of twisting.

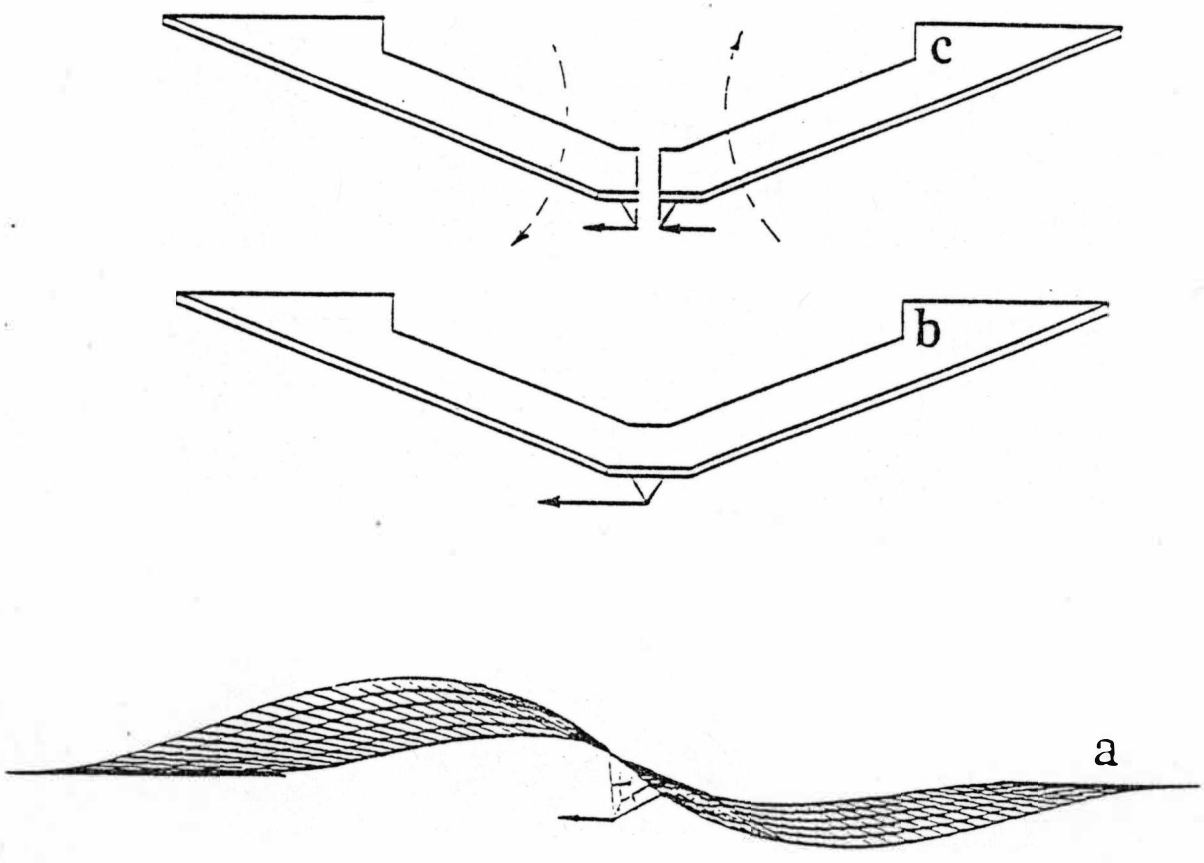

Figure 19. Joined Ends Effect on Torsion Response.

The appropriate mechanical model for the cantilever arms has to be a model having one fixed and one supported end since the two arms are connected at the tip and the

bending component of the torsion reaction on each arm is equal and opposite (Figure 5c). Such a consideration converts the cantilever with a free end to a cantilever with its end constrained for vertical motion.

In this mode of deformation, the bending energy expression for a cantilever with the constrained end, U_b, is one forth of that of the beam with a free end that requires replacement of initial Noy expression with :

$$U = 2(U_b + U_t) = 2\left(\frac{M^2 L}{8EI} + \frac{\tau^2 L}{2GJ}\right) \quad (21)$$

The expressions for I and J in the case of thin plates are:

$$I = \frac{wh^3}{12} \quad (22)$$

$$J = \frac{wh^3}{16}\left(\frac{16}{3} - 3.36\frac{h}{w}\right) \approx \frac{wh^3}{3} \quad (23)$$

Substitution of the values into equation 16 results in:

$$U = \frac{T^2 L}{Ewh^3}\left(6\cos^2\theta + 3(1+\upsilon)\sin^2\theta\right) \quad (24)$$

The torsional spring constant is obtained by taking the reciprocal of the second derivative.

$$K_t = \frac{Ewh^3}{L} \frac{1}{6\cos^2\theta + 3(1+\nu)\sin^2\theta} \quad (25)$$

of the total strain energy with respect to T. Taking the standard beam equation for the normal spring constant:

$$K_n = \frac{Ewh^3}{4L^3} \quad (26)$$

The ratio of torsional to nomal spring constants is:

$$\frac{K_t}{K_n} = \frac{4}{3} \frac{L^2}{\cos^2\theta + 3(1+\upsilon)\sin^2\theta} \quad (27)$$

Taking into account the tip height, H, the lateral spring constant is:

$$K_{lat} = \frac{K_t}{H^2} \quad (28)$$

Combining equations 20 and 21 the lateral spring constant is then:

$$K_{lat} = \frac{4}{3}\left(\frac{1}{\cos^2\theta + (1+\upsilon)\sin^2\theta}\right)\left(\frac{L}{H}\right)^2 K_n \quad (29)$$

Therefore, incorporation of the connection at the tip gives a different denominator expression for k_t/k_n. Compare equation (29) to equation (27).

$$\frac{K_t}{K_n} = \frac{4}{3}\frac{L^2}{[\cos^2\theta + 2(1+\nu)\sin^2\theta]} \quad (30)$$

and the denominator of equation (31) is also different compared to equation (29)

$$K_{lat} = \frac{4}{3}\frac{1}{[\cos^2\theta + 2(1+\nu)\sin^2\theta]}\left(\frac{L}{H}\right)^2 K_n \quad (31)$$

where Θ is the angle between substrate and one of the legs.

These final expressions are similar to ones proposed by Noy et al. but have different numerical coefficients. Equation (31) yields a value of $k_t/k_n = 6.9\text{x}10^{-9}$ which is very close to the full FEA solution of $7.28\text{x}10^{-9}$ (Table 2). The small difference is due to non-rectangular beam ends. The expressions (26) and (31) can be

recommended for calculation of torsion constants for V-shaped cantilevers and are expected to give precision better than 10%.

The next step is an estimation of the torsional spring constant of cantilevers for conversion of friction signal to a force scale. The torsional spring constant, k_t, in units torque per unit torsion angle, newton-meter per radian, is calculated from the rotation of the tip base plane caused by application of lateral forces to the end of the tip. The lateral deflection spring constant, k_{lat}, in units of force over linear tip displacement, Newtons per meter, is calculated from the linear motion of the probe tip under the same conditions. This linear lateral spring constant is a result of the torsion of the tip and the compression and extension of the cantilever legs. The contribution of the compression and extension of leg length as evaluated by FEA is less than 3% of the contribution due to torsion of the tip.

FEA results were used to calculate the lateral spring constant. A lateral application of force was modeled and the resulting deflection was used to calculate K_{lat}. Also several configurations were tested with the forces applied to represent contact. There was a very weak coupling of bending deflection and lateral spring constant.

In support of the FEA modeling, tests of a 5000:1 (larger) model of the cantilever showed similar response. This is in contrast to the Larbardi et al. (1994) results mentioned earlier.

CHAPTER IX

ERROR ANALYSIS OF METHODS

To simplify calibration and make it feasible for routine usage we have to analyze the role of different parameters and determine critical ones to be included in the final consideration. To examine the dependence of results to experimental measurements a sensitivity analysis was performed on the parameters involved in the derivation of spring constants and resonant frequencies. First an analysis of factors taken individually will show the large possible error range implied by isolation of the expected variation in individual parameters. Then an error analysis taking into account the expected interrelationship of the quantities of Young's modulus and density will show the advantage of combining the thickness, density, and Young's modulus into one measurement by experimental determination of the cantilever resonant frequency.

Au and Si_3N_4 layers and their respective Young's modulus. As previously mentioned the Au layer acco The section moment calculation is based on four factors, the thickness of the unts for 11% of the stiffness for the cantilevers tested. The possible range of transformed section moment due to uncertainty in Au thickness is shown in Figure 20. The ±5nm uncertainty in Au thickness produces an uncertainty of ±1.75% in calculated section moment. The Young's modulus estimate uncertainty of ±20Gpa would cause a total beam section modulus uncertainty of ±2.5% (Figure 21).

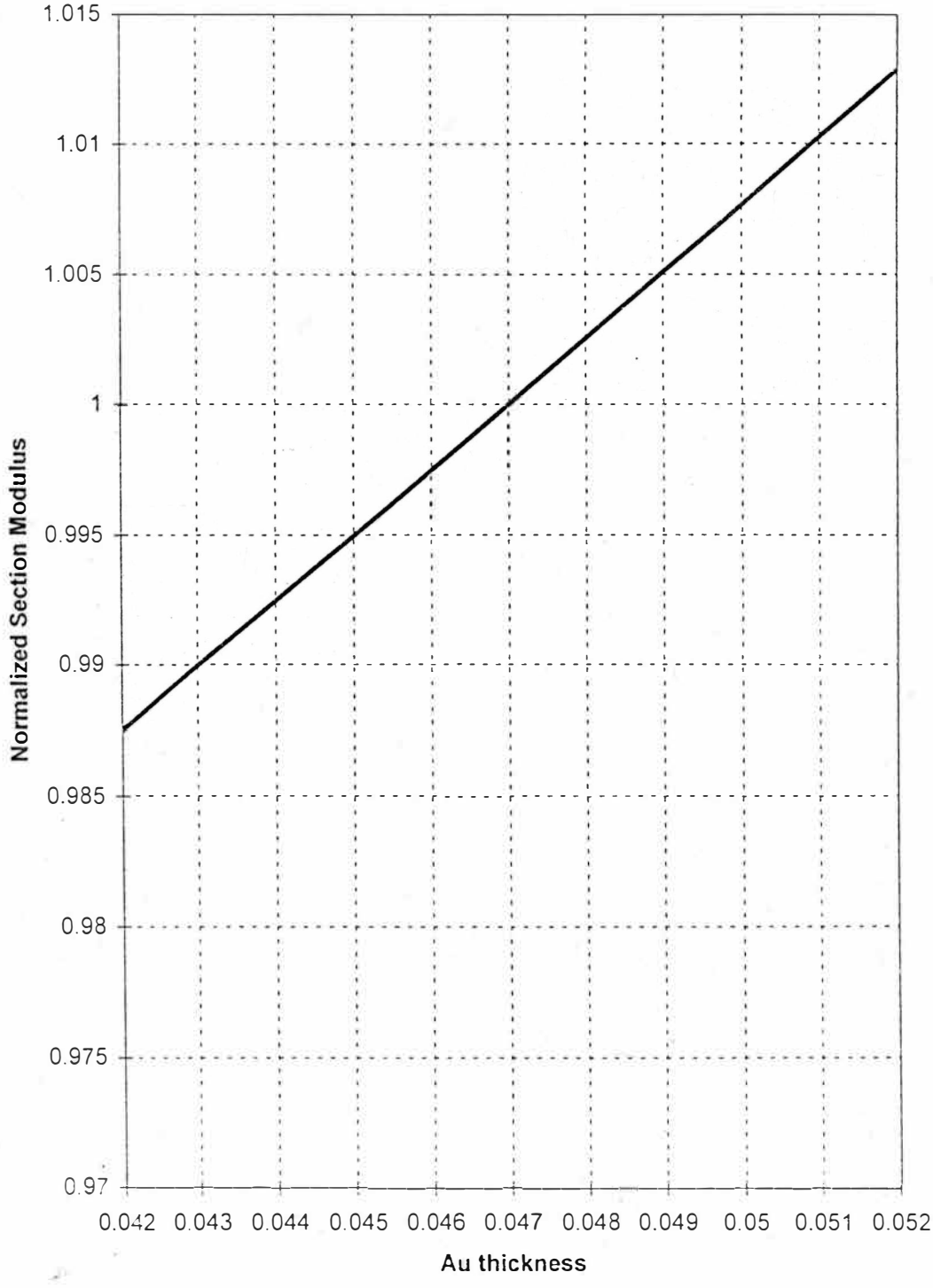

Figure 20. Section Moment vs. Au Thickness.

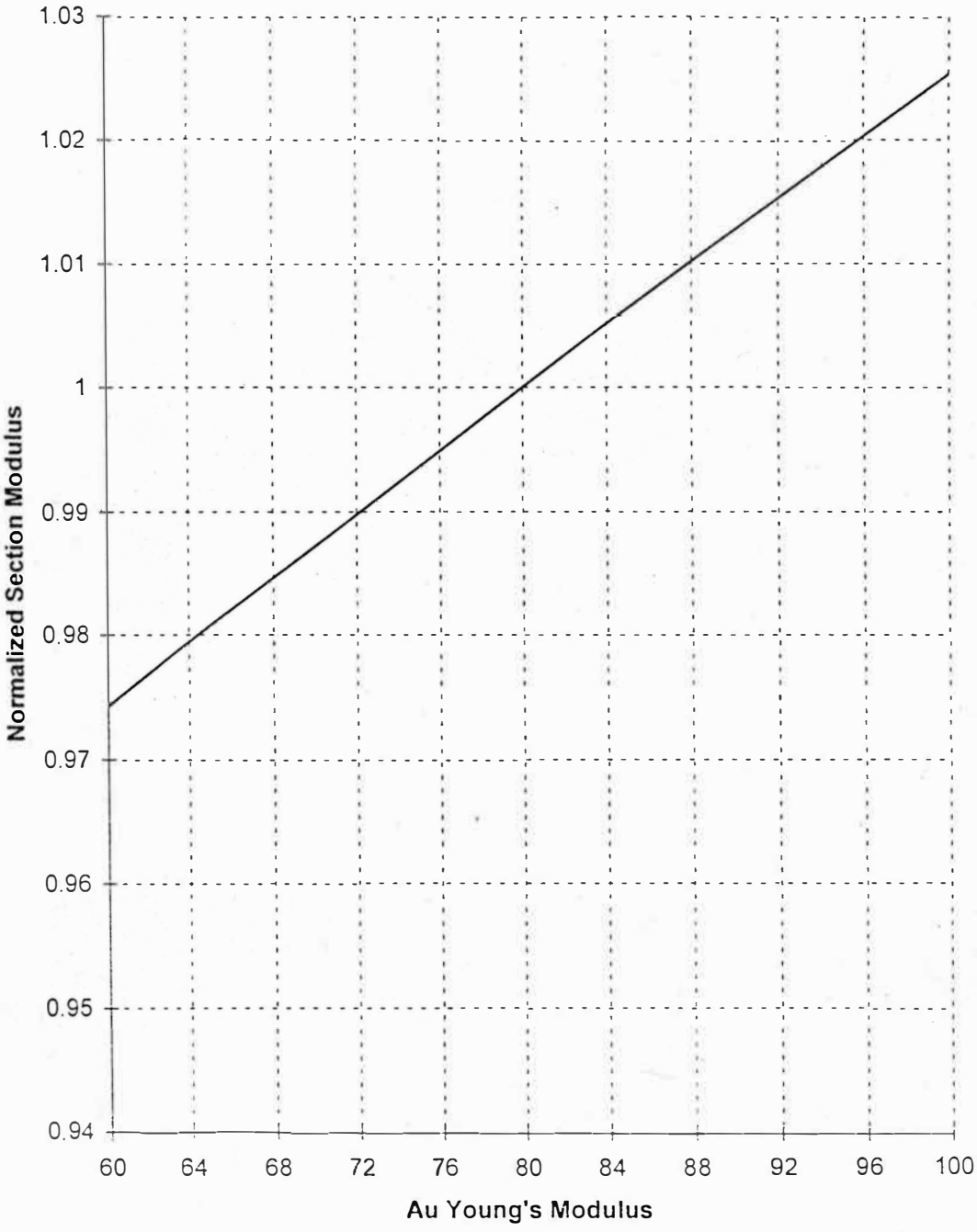

Figure 21. Section Modulus vs. Au Young's Modulus.

The Si_3N_4 layer thickness measurement by electron microscope has an uncertainty of ±50nm produces an uncertainty of ±24% for direct calculation of section modulus (Figure 22). Lastly the young's modulus of the Si_3N_4 can vary by ±50Gpa which also leads to an uncertainty of ±24% (Figure 23). Clearly the implied >50% uncertainty shows that directly calculating spring constant through geometry measurements and estimation of Young's modulus will not achieve the desired accuracy in cantilever stiffness calibration.

These variations taken separately would not allow ±10% accuracy in estimating the spring constant. However the combination of these elements into a resonant system creates an interdependence of the thickness and the resulting calculated Young's modulus that tends to compensate for any error in the thickness measurement of the Si_3N_4. An overestimate of thickness tends to result in an underestimate in the derived Young's modulus which has a self-correcting tendency in the determination of spring constant. The error in calculated mass is an important factor, and it will also be discussed below.

The evaluation of the dependence of cantilever resonance frequency on various parameters is critical to estimation of the spring constant. The uncertainty in thickness (Figure 24), density (Figure 25) and Young's modulus (Figure 26) of the gold coating all have less than 1% effect on resonant frequency.

The resonant frequency is determined by the spring constant and the effective mass (M_{eff}) of the cantilever.

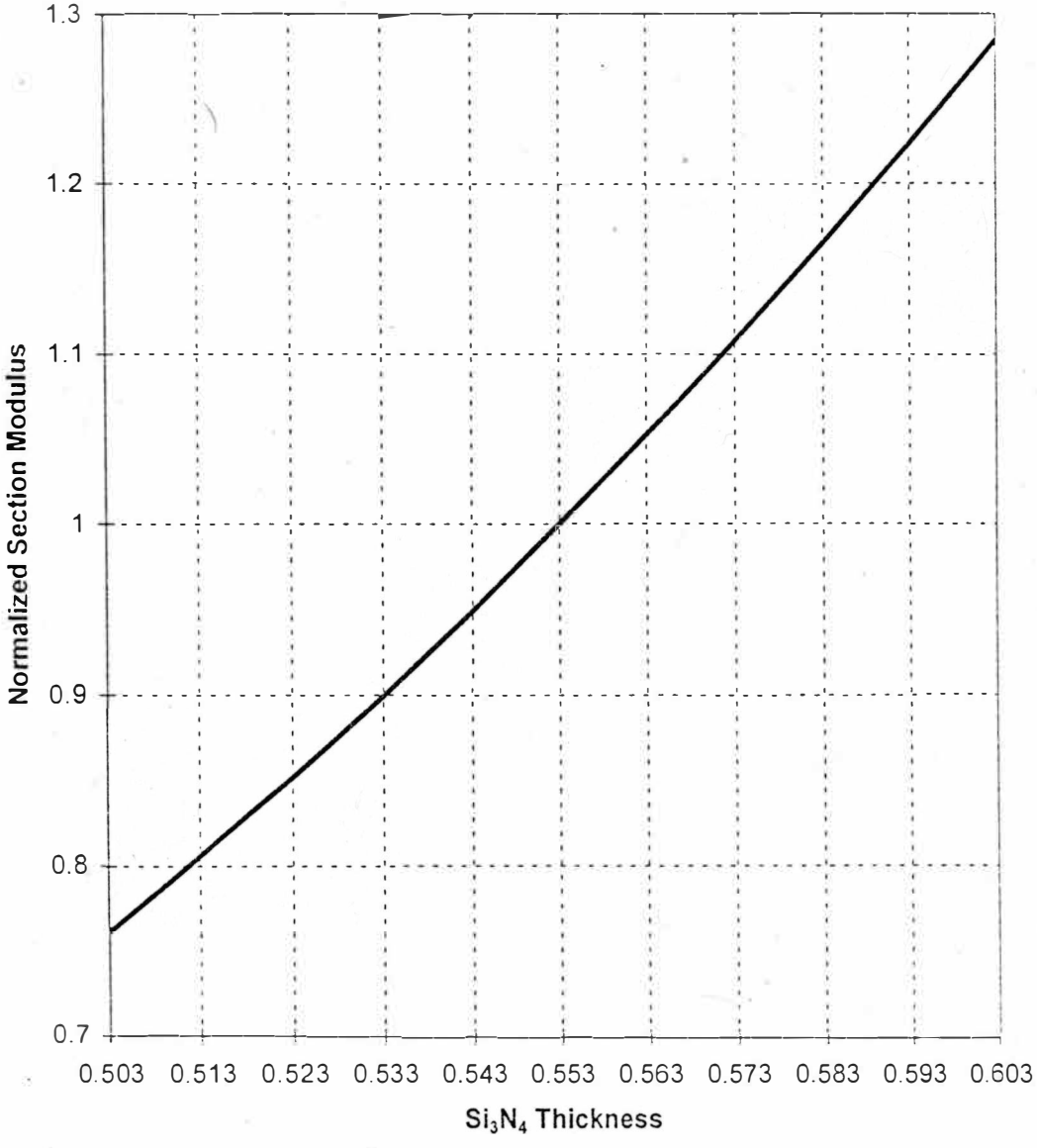

Figure 22. Section Modulus vs. Si_3N_4 Thickness.

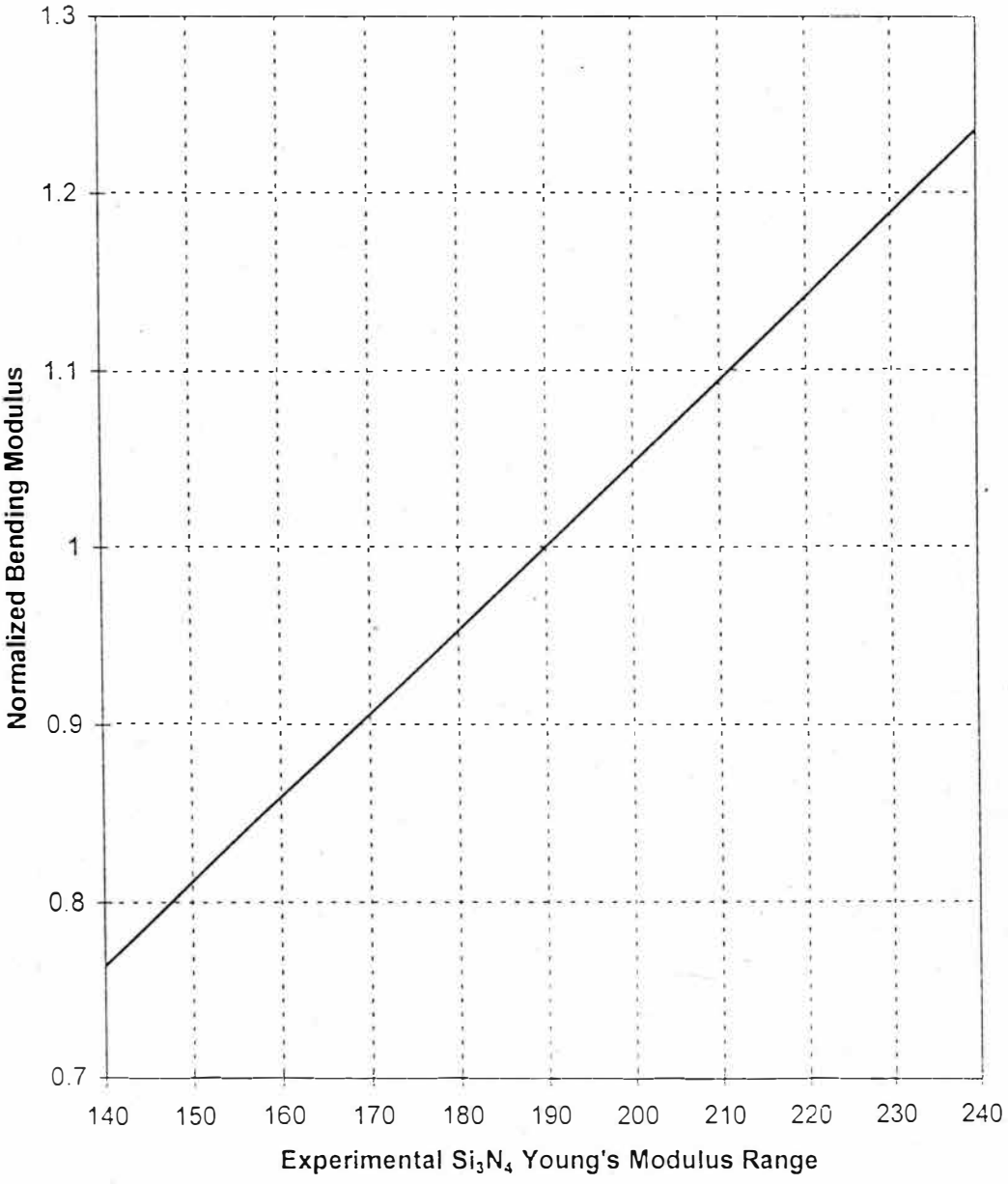

Figure 23. Section Bending Modulus vs. Si_3N_4 Young's Modulus.

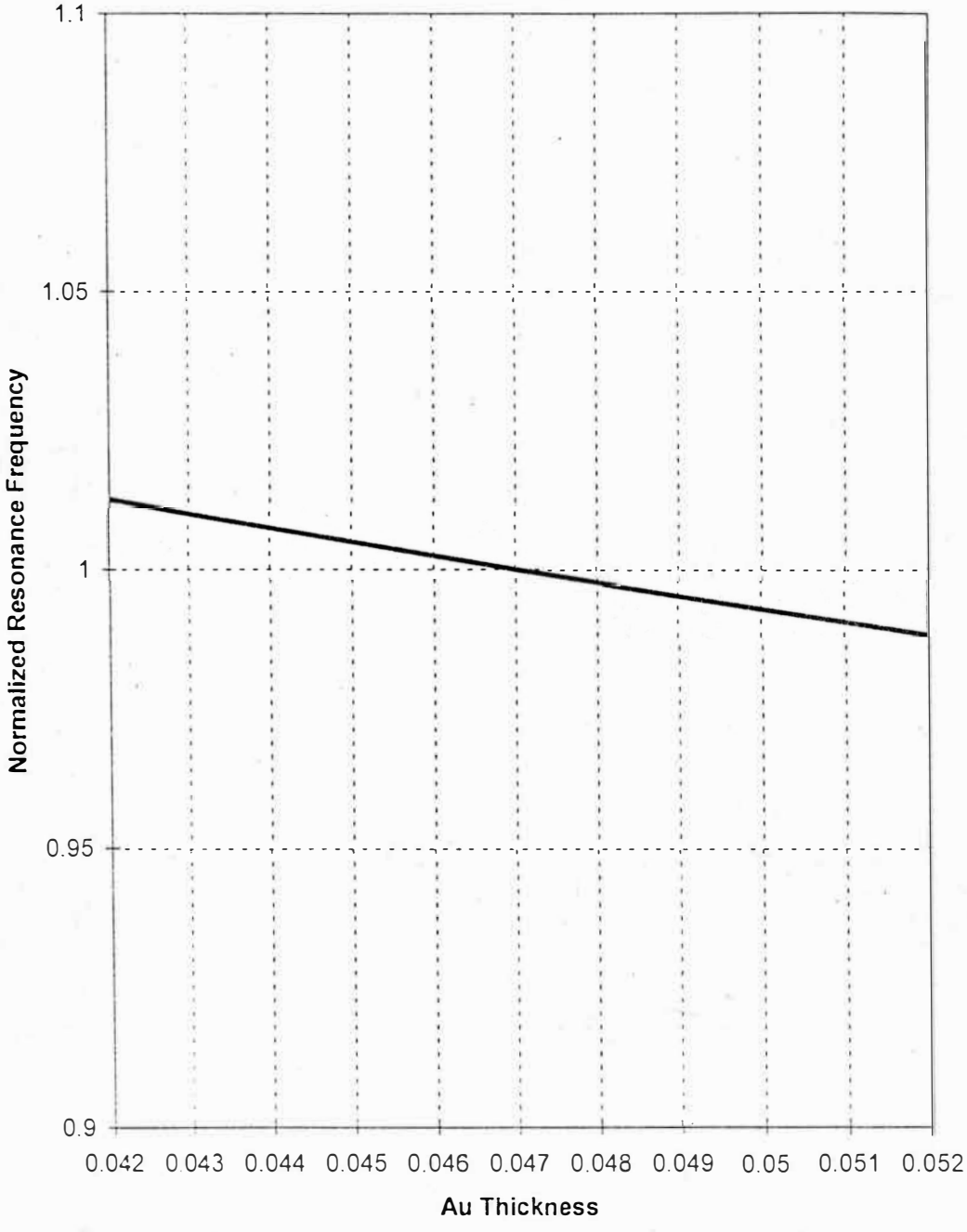

Figure 24. Sensitivity of Resonance Frequency to Au Thickness.

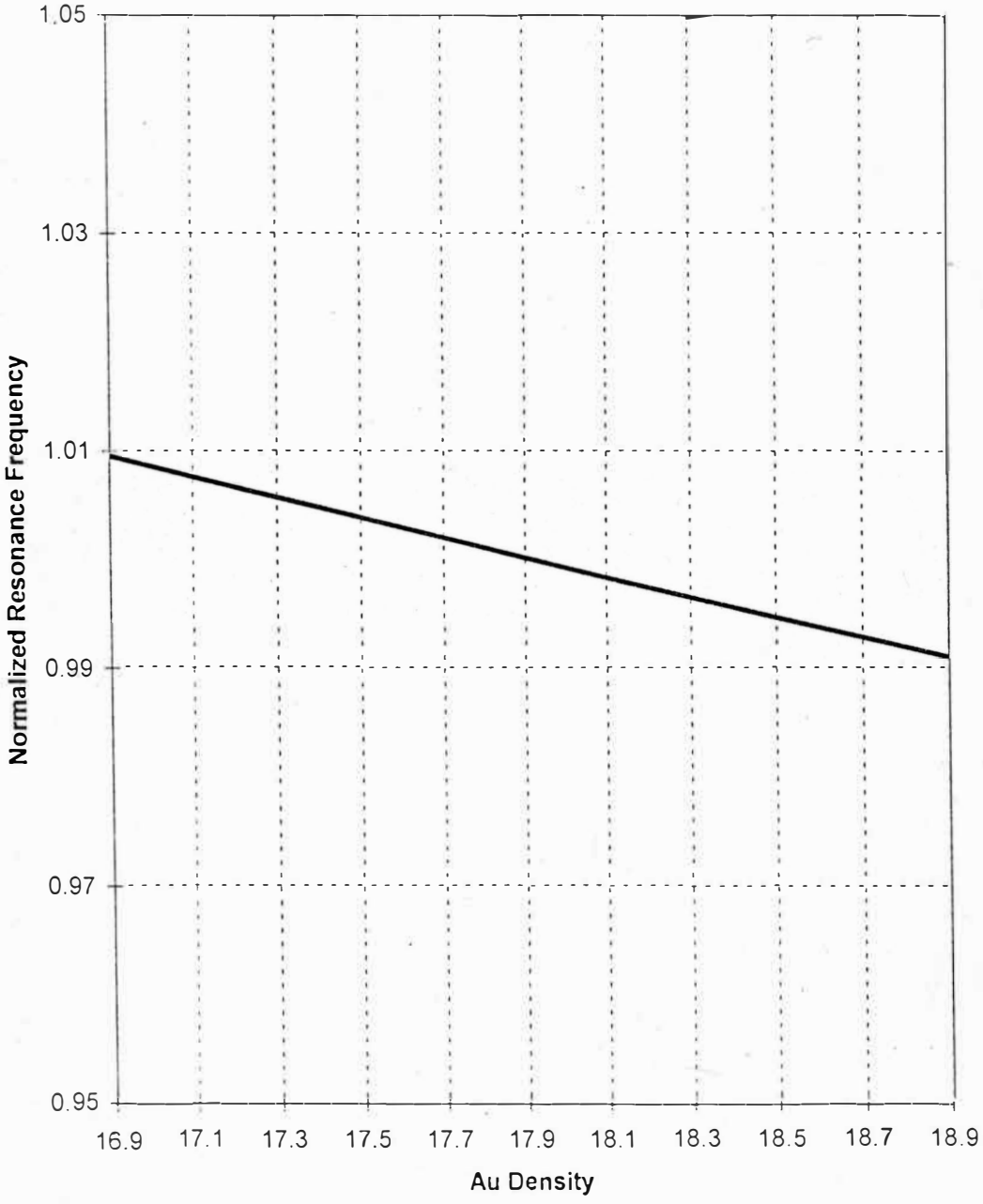

Figure 25. Sensitivity of Resonance Frequency to Au Density.

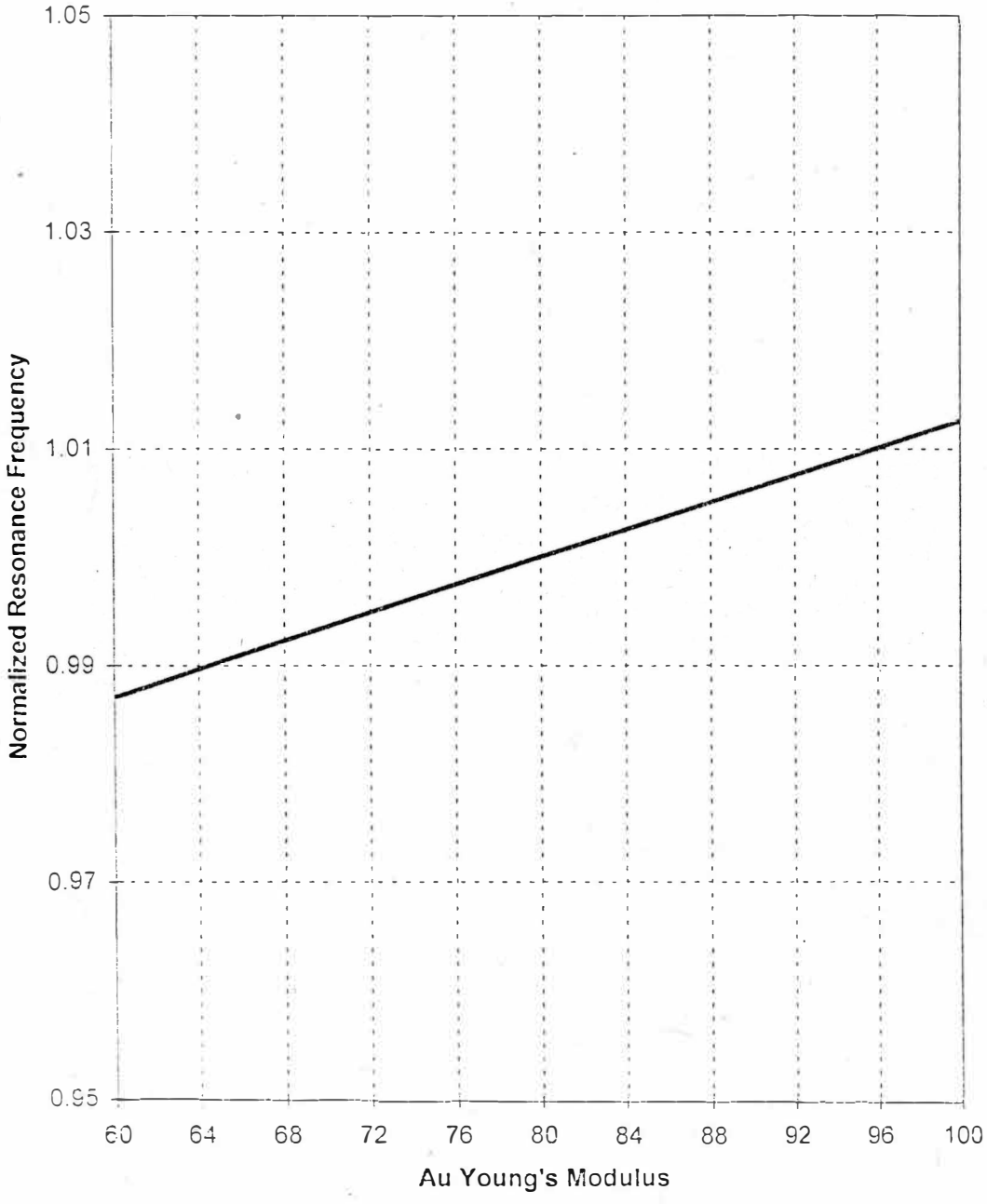

Figure 26. Sensitivity of Resonance Frequency to Au Young's Modulus.

$$F_o = \frac{1}{2\pi}\sqrt{\frac{K_n}{M_{eff}}} \qquad (32)$$

The value of Kn can be expressed as:

$$K_n = CEI \qquad (33)$$

C is a factor that takes into account the lateral geometry of the cantilever. E is the Young's modulus and I is the section moment. These two factors which are responsible for the greatest uncertainty in calculating Young's modulus are measured as a group. This lumping of parameters allows for drastic reduction in uncertainty due to the accuracy in measuring the resonance frequency of better than 0.1% using the cystal oscillator based system of the AFM non-contact apparatus.

Complicating this issue is the additional parameter of the change in calculated mass due to a change in thickness that is an integral part of modeling the composite cantilever. A 10% increase in Si_3N_4 thickness implies a 6% increase in the composite cantilever which would cause a 6% increase in the estimated spring constant.

Figure 27 shows the relationship for the resulting Young's modulus vs. measured thickness for a fixed resonant frequency and lateral dimensions. The corresponding calculation of spring constant due to the range of error in Si_3N_4 thickness is shown in Figure 28.

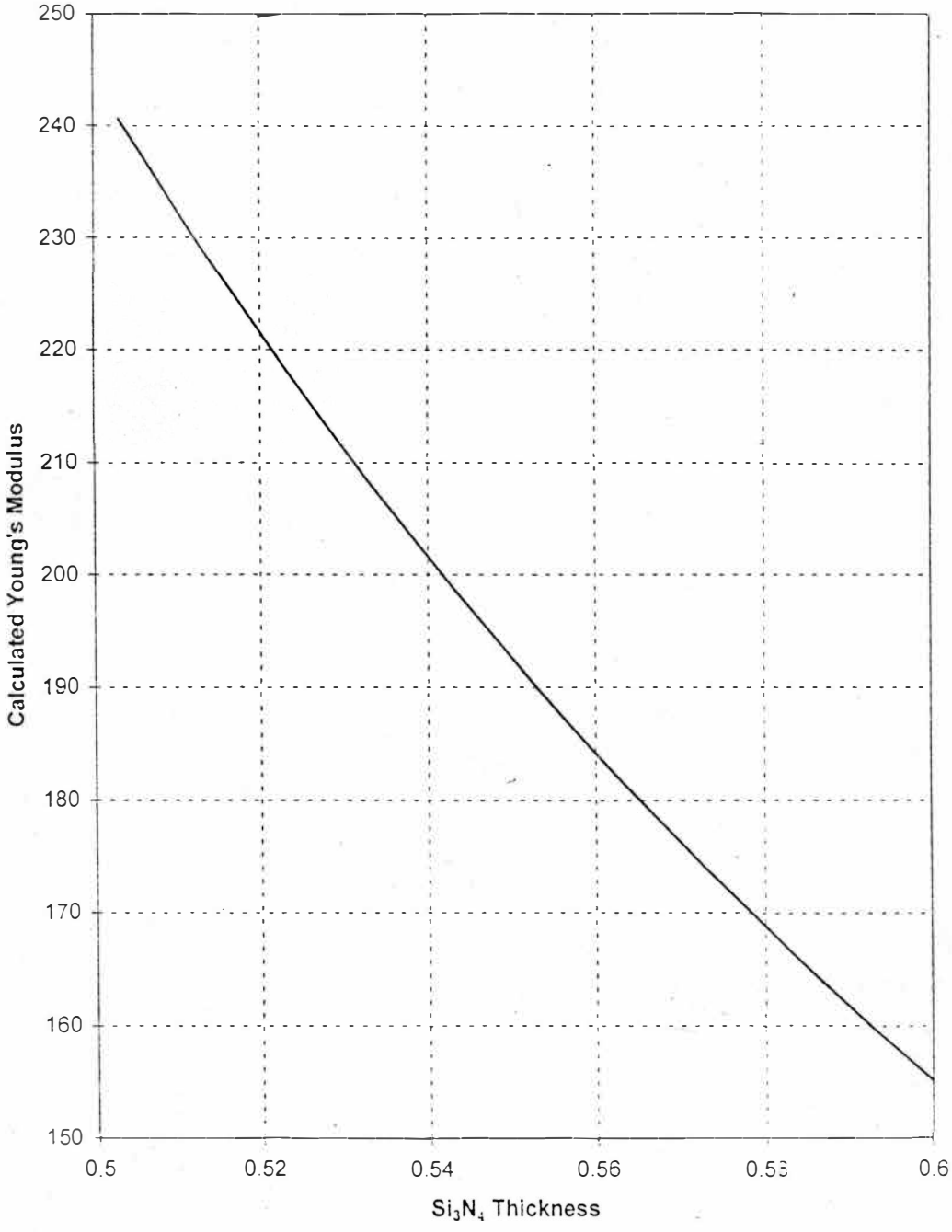

Figure 27. Calculated Modulus vs. Thickness.

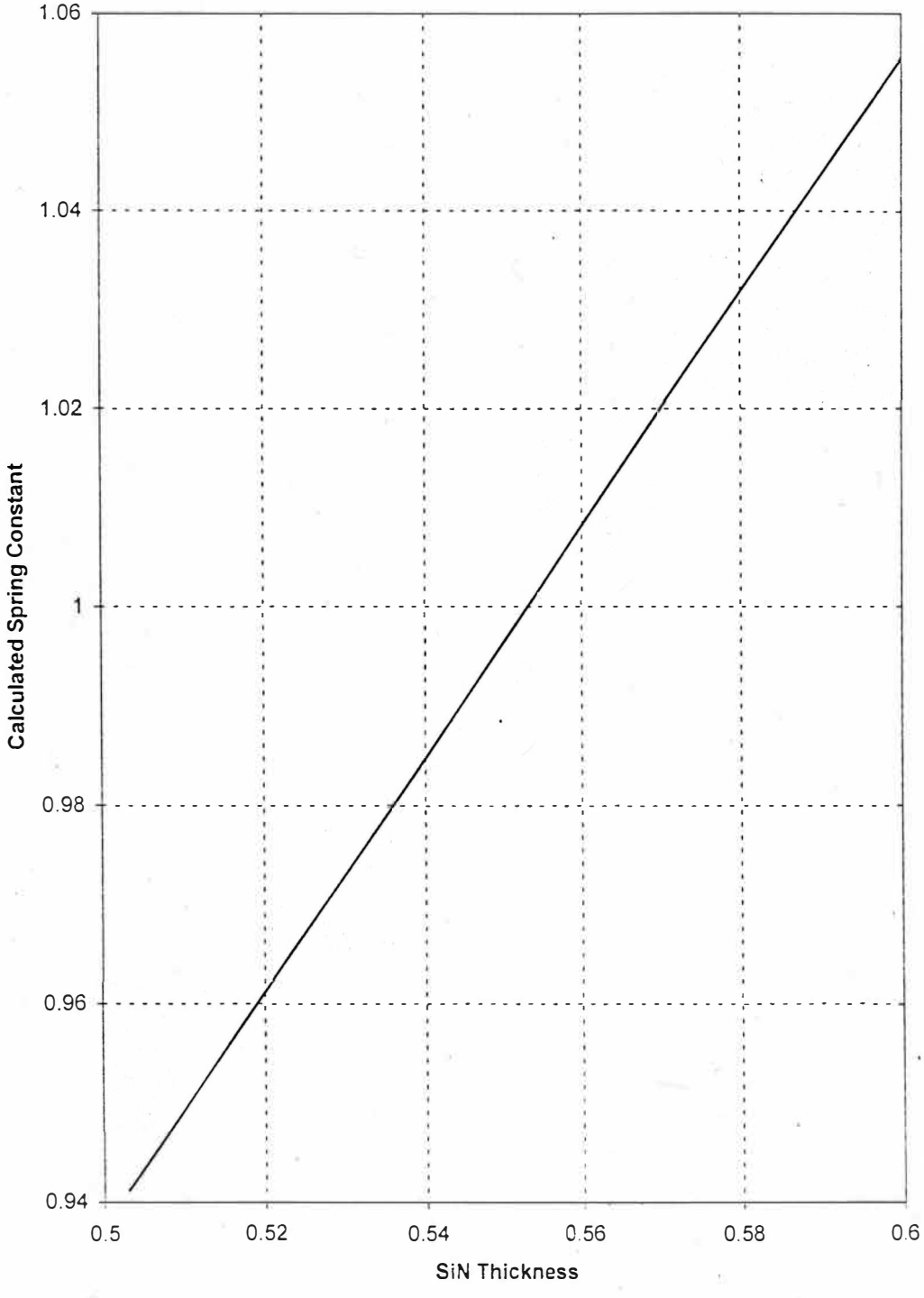

Figure 28. Calculated Spring Constant vs. Si_3N_4 Thickness.

However, a review of the literature (Jahanmir, 1994) shows a definite scaling of density with Young's modulus. Figure 29 shows the literature data. Fortunately this

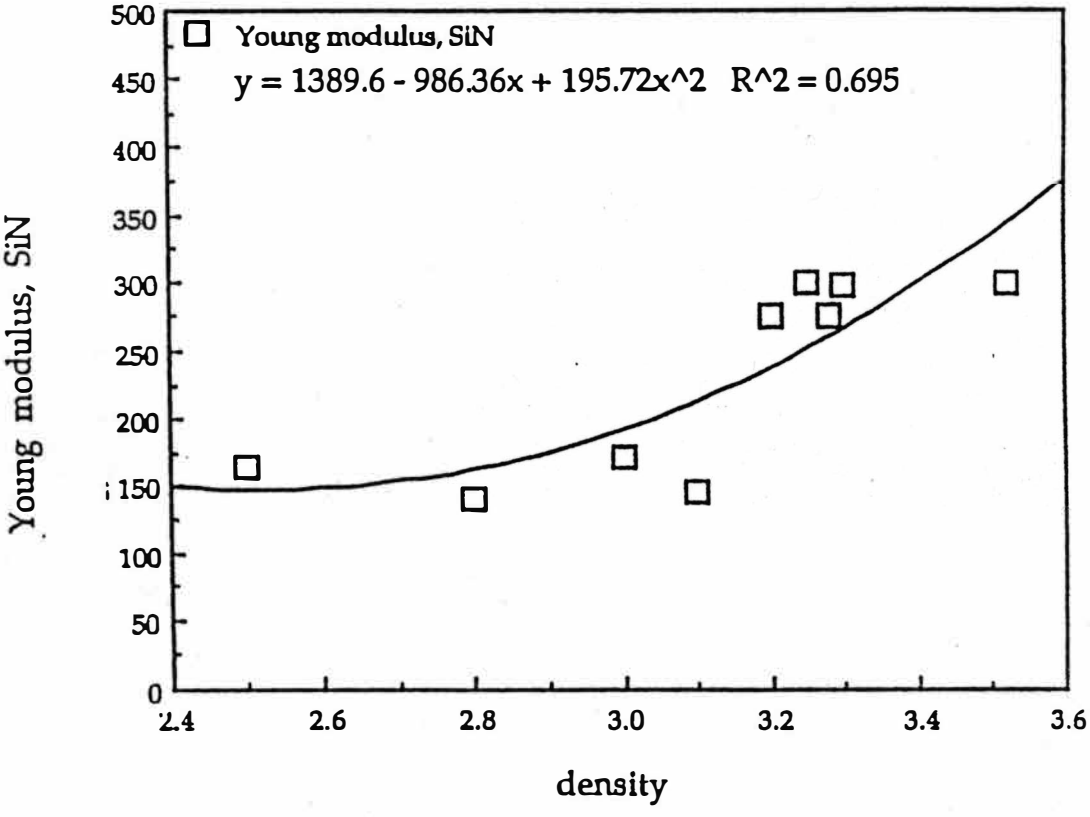

Figure 29. Young's Modulus vs. Density.

scaling can be incorporated into the modeling to remove some of the effects of error in measuring the cantilever thickness. For a fixed value of spring constant and lateral dimensions, E and I are inversely proportional. The value of I depends on the cube of thickness and therefore the value of calculated Young's modulus is inversely proportional to the thickness measurement cubed. This gives a derived Young's modulus that tends to compensate for thickness measurement errors.

The calculation for an measurement error of larger than actual thickness results in a lower calculated Young's modulus which implies a lower density in Si_3N_4 and thereby partially compensates for the error in calculated mass due to the thickness. Thus by employing this resonance frequency measurement with known relationships of material stiffness vs. density, the estimation of spring constant is much less prone to error than the uncertainty in thickness measurement would imply. Figure 30 shows the resulting calculated spring constant variation is only ±1% when the thickness measurement uncertianty is up to ±5% (±.025 microns).

In this work the lateral spring constant is determined by FEA modeling of the cantilever geometry to determine the ratio of lateral to normal spring constant. The variation of this ratio over the range of uncertainty in significant geometrical measurements is encouraging. The uncertainty in measuring the angle of the cantilever legs was ±1 degree. Figure 31 shows the variation in spring constant ratio K_{lat}/K_n as the angle is varied by ±1 degree. As a point of interest, the variation in the K_{lat}/K_n ratio is Figure 32 is plotted for large changes of theta to illustrate trends in the ratio. This also illustrates the unsuitability of the parallel beam approximation for determining lateral spring constants.

The error in measuring the leg length of the cantilever has a possible influence of ±2.5% on the spring constants ratio as shown in Figure 33. This ratio is independent of any variation of K_n introduced by error in leg length measurement. Poison's ratio was not measure in this work so a broad range of Poison's ratio was evaluated for the possible effects. This variation is probably much lower than

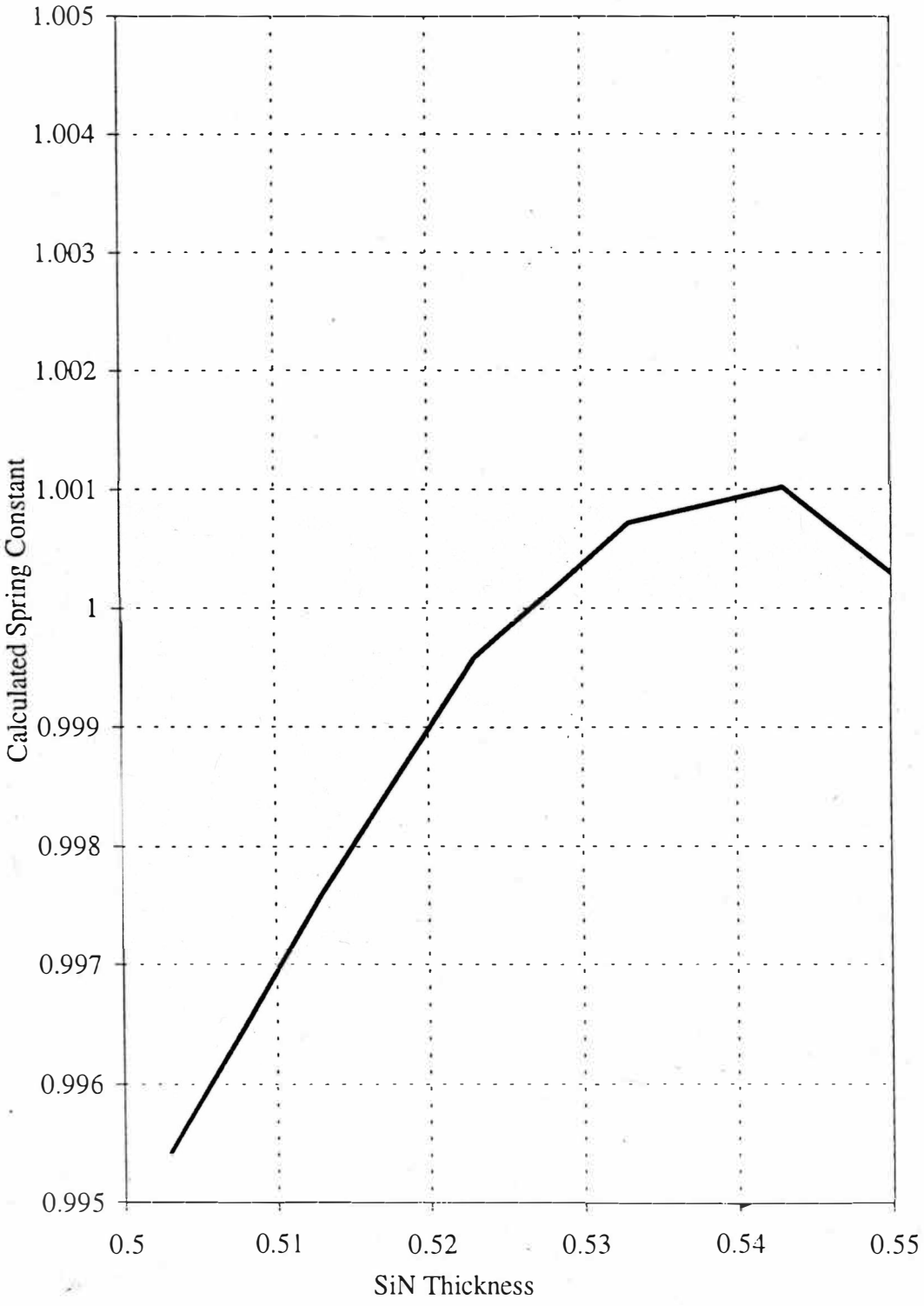

Figure 30. Calculated Spring Constant vs. Measured Si_3N_4 Thickness.

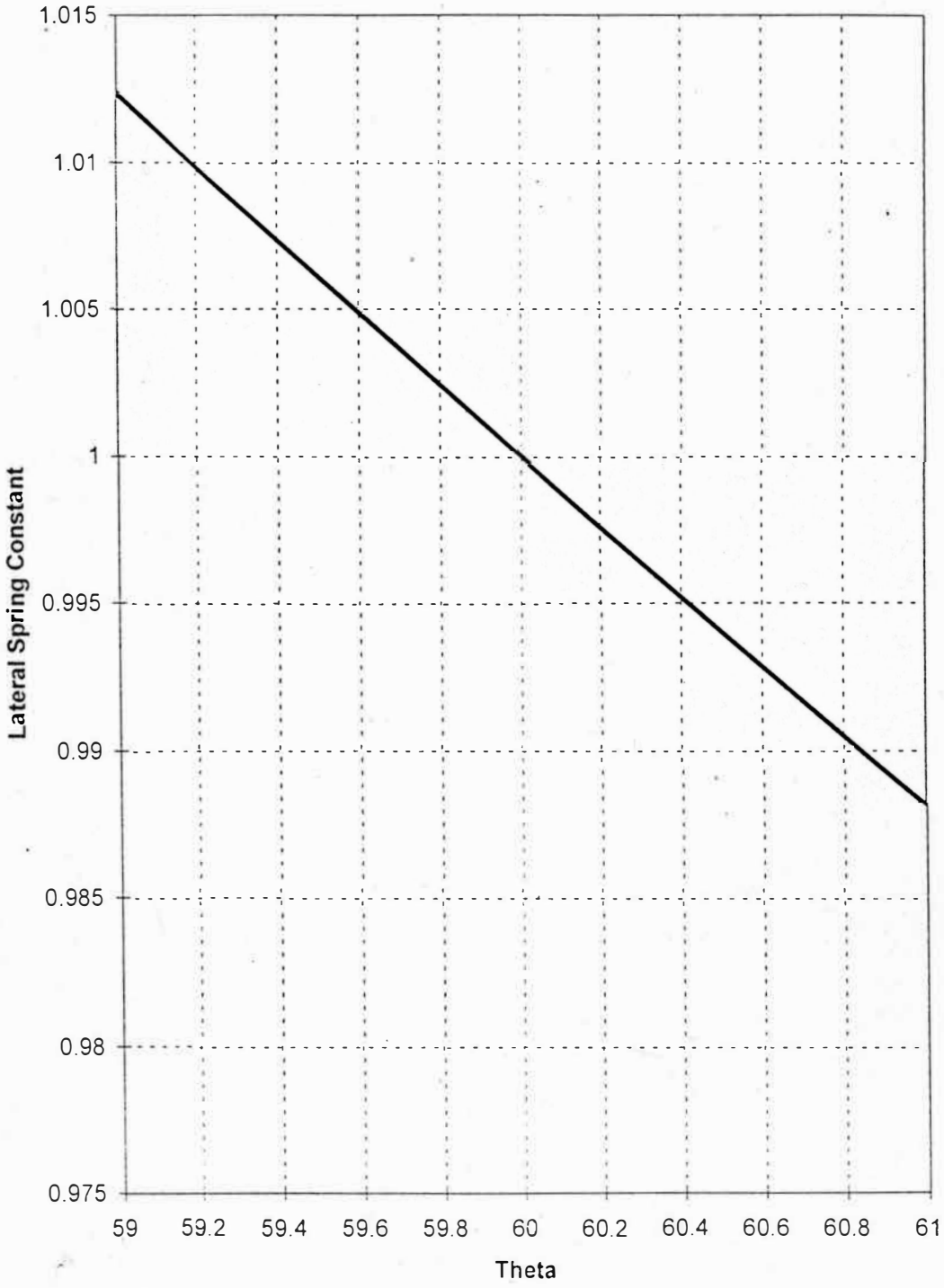

Figure 31. Sensitivity of K_{lat} to Theta Measurement Error.

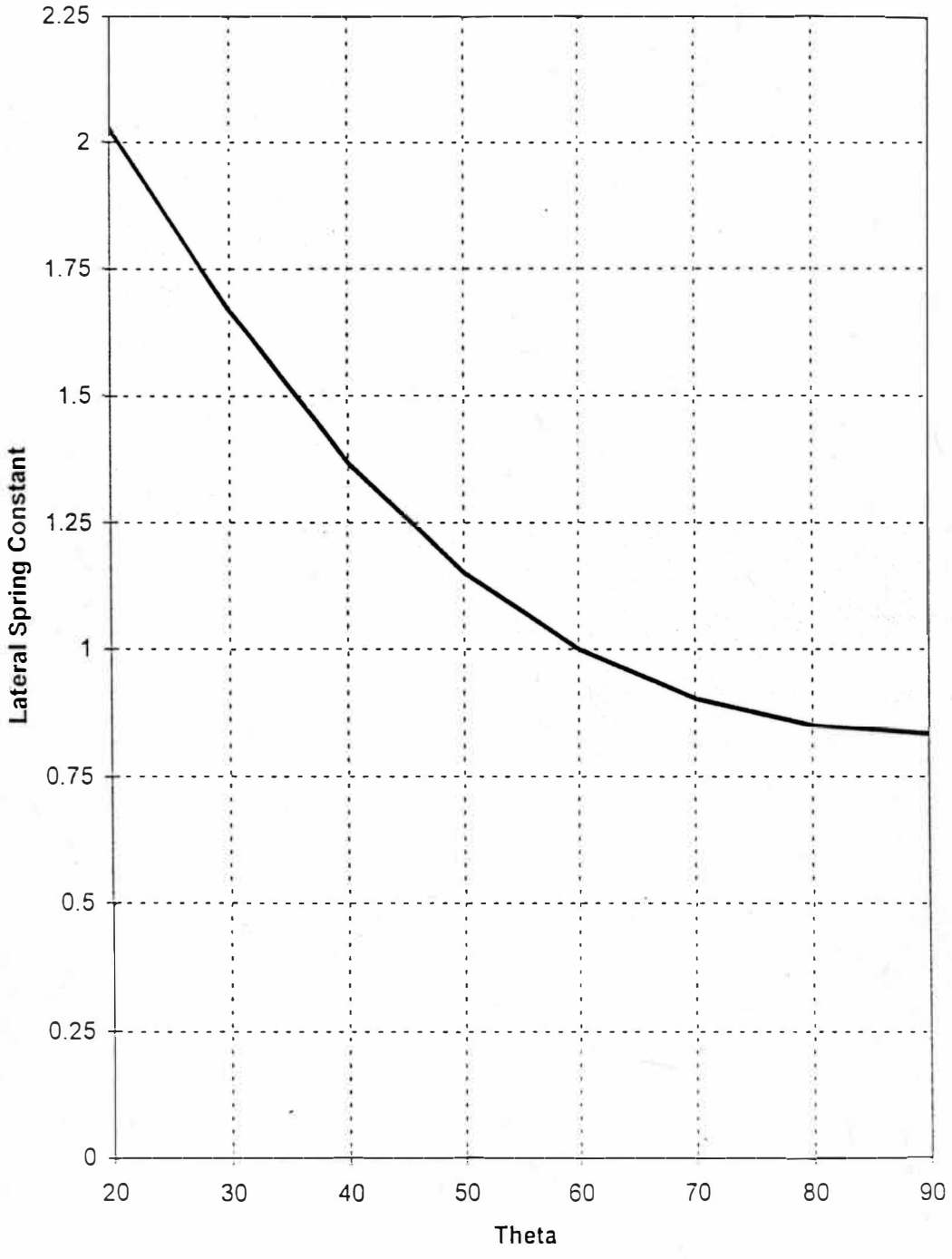

Figure 32. Sensitivity of K_{lat} to Theta.

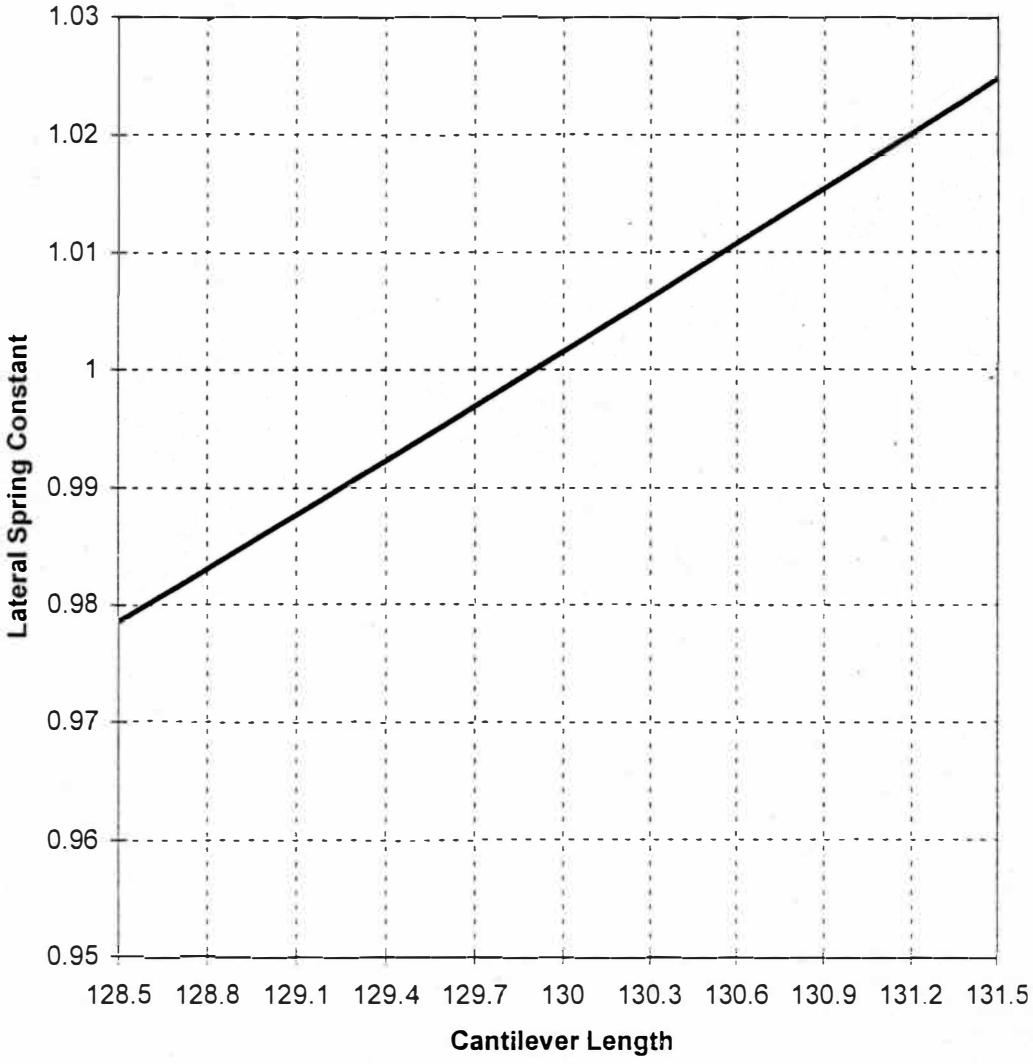

Figure 33. Sensitivity of K_{lat} to Cantilever Length.

presented, but even at the large variation it is still of small consequence as shown in Figure 34. The tip height is established by the photo-mask used to etch a pit in silicon. The etchant preferentially etches along the crystal planes of the silicon and

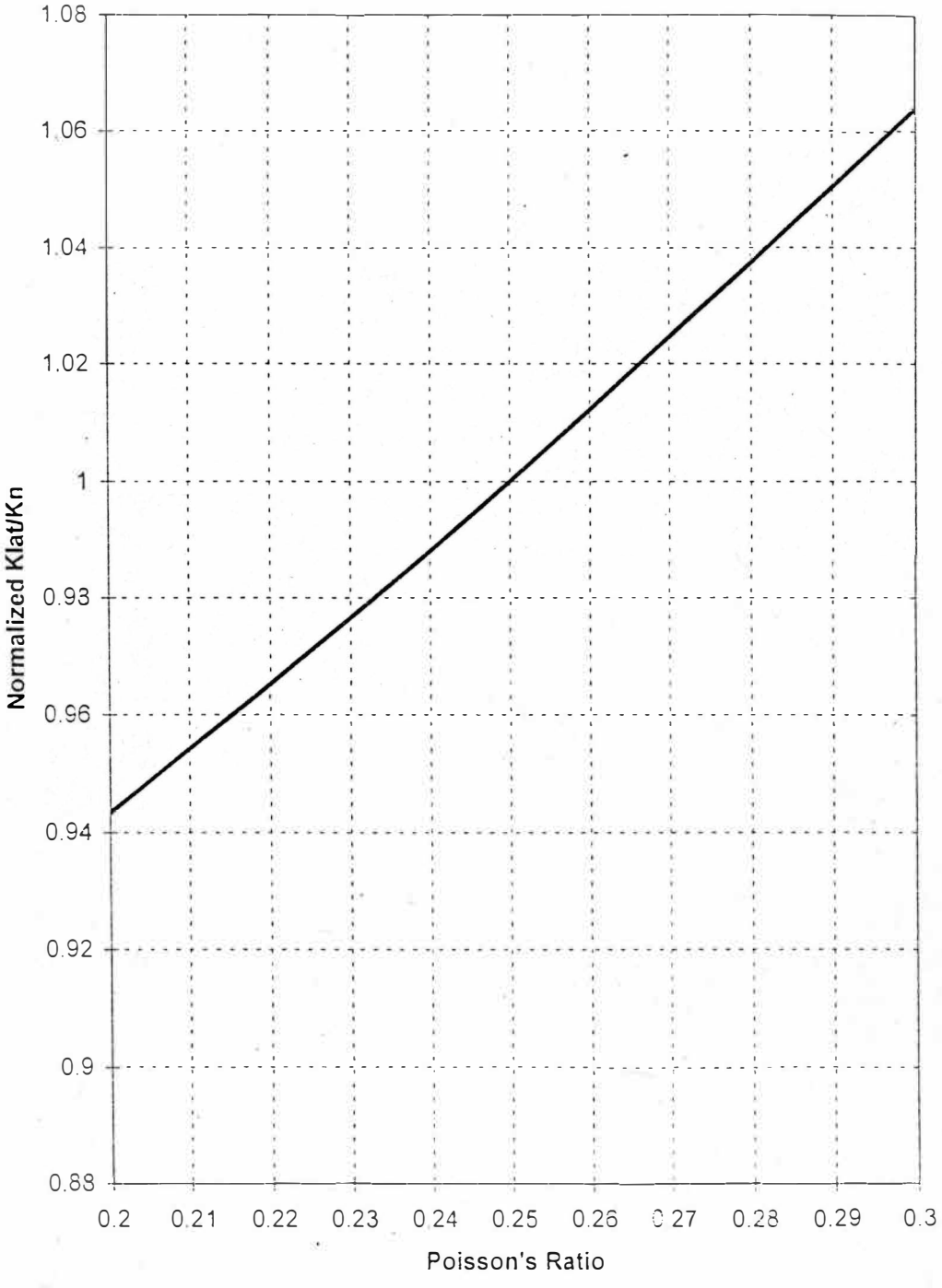

Figure 34. Sensitivity of K_{lat}/K_n to Poisson's Ratio.

then stops at a peak. This creates a very consistent geometry so the tip height is well controlled with most of the uncertainty in this measurement coming from the measured cantilever thickness. Figure 35 shows the possible ±6% variation in lateral spring constant due to uncertain tip height.

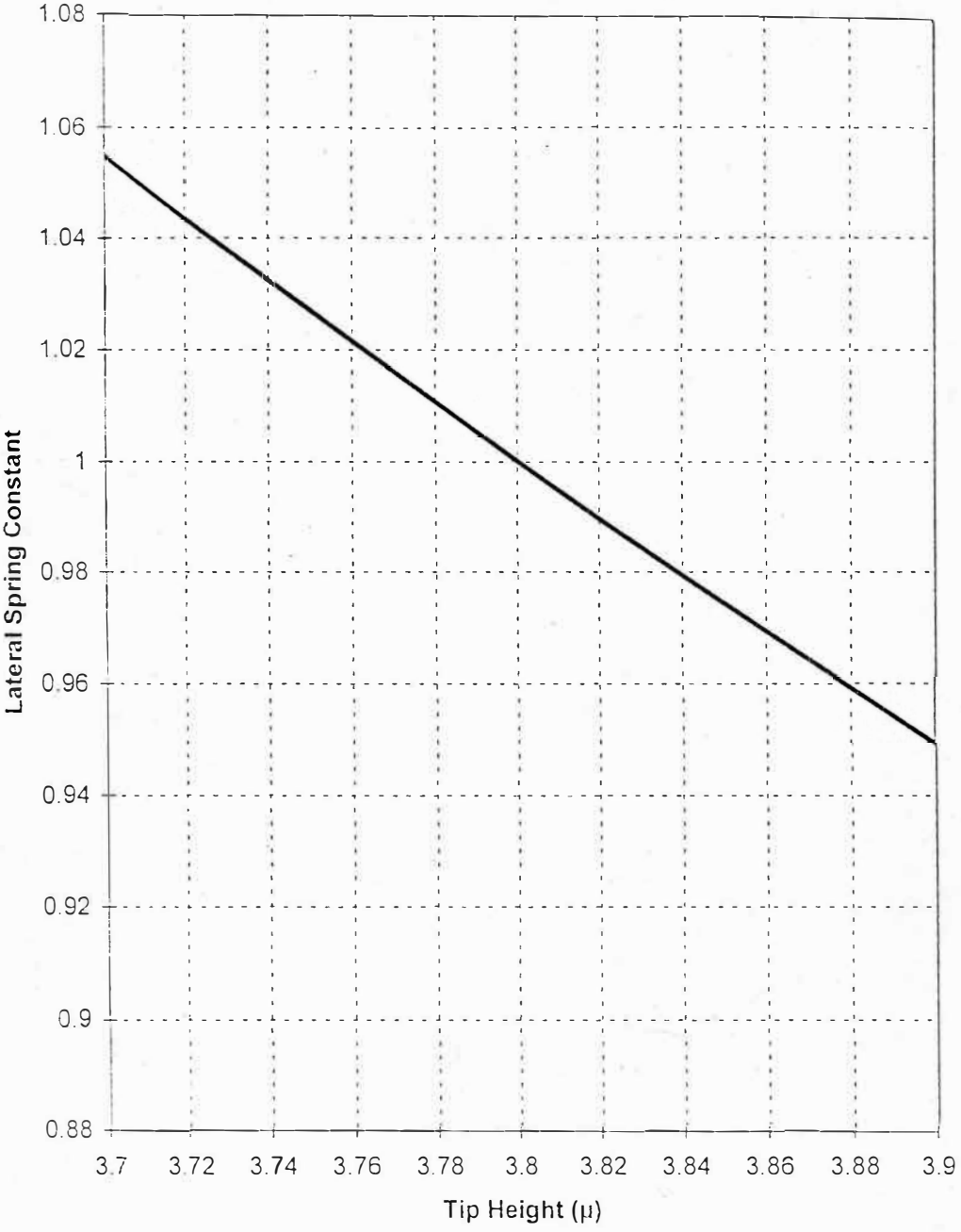

Figure 35. Sensitivity of Lateral Spring Constant to Tip Height.

CHAPTER X

DISCUSSION AND RESULTS

An important consideration for SPM friction measurements is the scanning direction. The most common scanning raster has the rapid scanning direction perpendicular to the cantilever axis of symmetry. Occasionally however, there is need to orient the rapid scan direction parallel to the cantilever axis of symmetry. Radmacher et. al. analyzed the effects of friction on this mode of scanning (Radmacher, 1993). The AFM used by Radmacher was in the constant deflection mode. This means that the feedback loop manipulates the z-peizo to maintain the laser spot on a preset position in the photodiode array. In turn this implies that the slope at the tip is held constant. Radmacher gives

$$z = \frac{F_n}{K_n}\left(\frac{x}{L}\right)^2 \quad (34)$$

for the deflection equation of an end loaded cantilevered beam. He then arrives at the expression

$$\frac{\partial z}{\partial x}_{x=L} = \frac{2z}{L} \quad (35)$$

$$\left.\frac{\partial z}{\partial x}\right|_{x=L} = \frac{2z}{L} \quad (35)$$

for the slope of a deflected cantilever. The Beer and Johnson give the deflection equation for an end-loaded cantilever as

$$z = \frac{F_n}{K_n}\frac{x^2}{2L^3}(3L - x) \quad (36)$$

Which implies the relation for the slope at the end of a deflected cantilever is given by

$$\left.\frac{\partial z}{\partial x}\right|_{x=L} = \frac{3z}{2L}. \quad (37)$$

Radmacher claims that the torque result from tip sample distance produces a height artifact. The height artifact due to the torque will be for decreased height in the forward scanning direction when traversing a high friction area. The opposite is true for the reverse direction. Radmacher claims that this allows subtraction of the forward and reverse images to obtain friction data. Assuming the friction induced moment to be $M=hF_f$ the change in slope is given as

$$\left.\frac{\partial z_m}{\partial x}\right|_{x=L} = \frac{2hF_f}{K_n L^2} \quad (38)$$

Using the equation for the deflection given by Beer and Johnson the actual value of change in slope at the cantilever end is

$$\left.\frac{\partial z_m}{\partial x}\right|_{x=L} = \frac{ML}{EI} = \frac{hF_f L}{\left(\frac{3EI}{L^3}\right)\left(\frac{L^3}{3}\right)} = \frac{3hF_f}{K_n L^2} \quad (39)$$

Resulting in a height artifact proportional to the bend of the cantilever that causes an identical change in slope at the end of the cantilever. By combining the equations above, the magnitude of the artifact produced by this effect can be expressed by

$$\left.\frac{\partial z_f}{\partial x}\right|_{x=L} = \frac{3hF_f}{K_n L^2} = \frac{3z_f}{2L} \quad (40)$$

Solving for the deflection:

$$z_f = \frac{2hF_f}{K_n L} \quad (41)$$

Finally substituting with reasonable values, h=3.5, F_f=10nN, L=100μm, and K_n=0.25N/m

$$z_f = \frac{2hF_f}{K_n L} = 2.8nm \quad (42)$$

Additionally, the lateral spring constant parallel to the axis of the cantilever is

$$K_{axis} = \frac{4EI}{Lh^2} = \frac{4}{3} K_n \frac{L^2}{h^2} = 270 \frac{N}{m} \quad (43)$$

This is more than double the value for the more commonly used K_{lat} spring constant of about 120N/m when the same cantilever is used scanning in the direction perpendicular to the cantilever axis.

$$F_{f1} = z_f K_n = 0.7nN \quad (44)$$

which results from the additional bend in the cantilever in response to the friction induced artifact. The cantilever is also at a 10 degree angle to the horizontal going downward from the substrate to the tip. During scanning this angle adds an additional contact force to the cantilever. If alpha is the angle made by the cantilever with the horizontal, the extra contact force is equal to

$$F_{f2} = F_f \sin(\alpha) = 1.74nN \quad (45)$$

Clearly for some situations where the fast scan direction of the raster is parallel this friction artifact can become an additional factor to account for.

This additional force F_{f2} is avoided by scanning in a direction perpendicular to the axis of the cantilever. In practice on Digital Instruments and Topometrix SPMs, there is no detectable coupling of friction to height data while the fast scanning direction is perpendicular to the probe axis of symmetry. The calibration of the lateral friction signal is a straightforward process.

Friction data for an individual scan line is often presented in the form of a friction loop (Figure 36). The horizontal axis in a friction loop represents the lateral

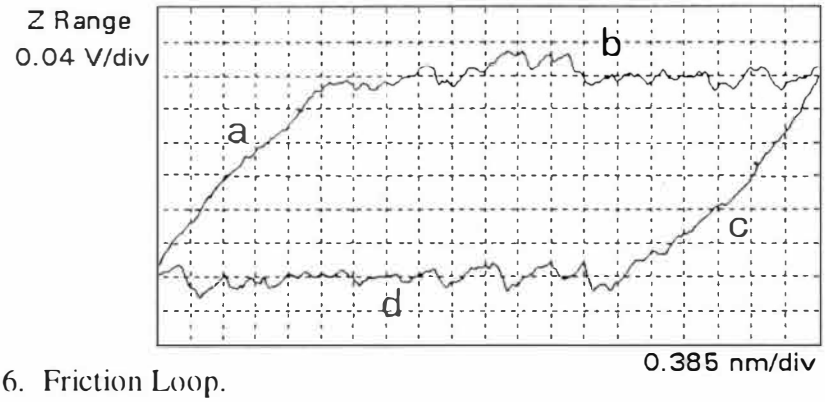

Figure 36. Friction Loop.

motion of the piezo scanner. The vertical axis reflects the torsion of the cantilever due to friction forces. The direction of the friction force and therefore the torsion is

opposite for forward and reverse directions. The voltage signal is opposite in sign for forward and reverse directions.

At the start of a particular scan line there is no sliding between the SPM tip and the sample. The initial motion of the piezo twists the cantilever until enough spring force is established to overcome the static friction coefficient. This initial non-sliding phase is denoted as "a" on Figure 36. In this non-sliding phase the lateral deflection of the tip is equal to the lateral displacement of the piezo scanner.

By observing the change in voltage output of the lateral photodiode signal at known displacements of the piezo scanner the deflection per volt of friction signal is obtained. The numerical value of the relationship is just the slope of the friction loop in the non-slip regime.

This factor is used to convert the lateral photodetector signal to the lateral cantilever deflection. Friction force is then calculated directly by

$$F_f = \frac{\Delta V}{2} m_{photo} K_{lat} \quad (46)$$

Where F_f is friction force ΔV is the difference between the forward and reverse traces of the friction signal, and m_{photo} is the slope of the signal in the non-slip regime. We established Digital Instruments Nanoscope specific instructions for this new calibration procedure (Appendix B).

CHAPTER XI

CONVENIENT CALIBRATION GRAPHS

The cantilever geometry used in this study is for a very commonly used SPM probe. The FEA modeling and materials parameter matching is a time consuming process. A method to minimize the calibration time would assist researchers to move to the data collection stage of their work more quickly. By correctly assessing the significance of cantilever parameters it is possible to streamline the process of calibration.

The previous analysis of possible variations of different cantilever parameters available in the literature allows drawing the conclusion that a major contribution comes from variable cantilever thickness in the range from 0.35 μm to 0.7 μm (0.60 μm in this work). For different wafers this variation results in 8 fold changes of spring constant. Primary attention should be paid to the variable thickness of the SPM cantilevers. Indeed, all other cantilever parameters (geometrical dimensions, density, and Young's modulus) contribute only about 1/7 of possible spring parameter changes caused by the variable cantilever thickness. Therefore, for further consideration we select cantilever thickness as a key parameter primary responsible for changes in spring parameters of the SPM cantilevers.

The k_n (f_0) behavior for composite ceramic/gold cantilevers with different thicknesses of gold overlays combining eqs. (32, 33) and FEA modeling for the evaluation of the geometrical factors, C_x, for V-shaped cantilevers is shown in Figure 37. These results are compared with a cubic solution for the equivalent homogeneous beam according to eq. (17). As is clear from this plot, a simple cubic relationship can be valid for a composite beam only within a narrow range of resonant frequencies.

The Figure 37 plots of $k_n(f_0)$ calculated for the bi-component cantilevers show rapid divergence from the homogeneous beam equation (10) in a wider range of resonant frequencies. The simple homogeneous beam approach overestimates spring constant for higher frequencies (thicker silicon nitride cantilevers) and underestimates spring constant at lower frequencies (thinner silicon nitride cantilevers). These deviations demonstrate the significant role of the bi-component composition of the SPM cantilevers in their complex mechanical behavior. Calibration plots k_n vs. f_o which can be used for spring constant assessment should account for the composite beam structure with very different elastic moduli and densities for the ceramic layer and gold overlay.

The actual mechanical behavior of the composite beams can be presented in the form of a scaling law in the form $k \sim f_o^{\bullet}$ where $\bullet$ varies from 2.45 to 2.65 for gold overlay thicknesses from 70 to 30 nm as determined by fit of the calibration curves in Figure 36. This result explains the k (f_o) fits observed experimentally for the SPM cantilevers where deviation from simple power laws with integer exponents. [21] The

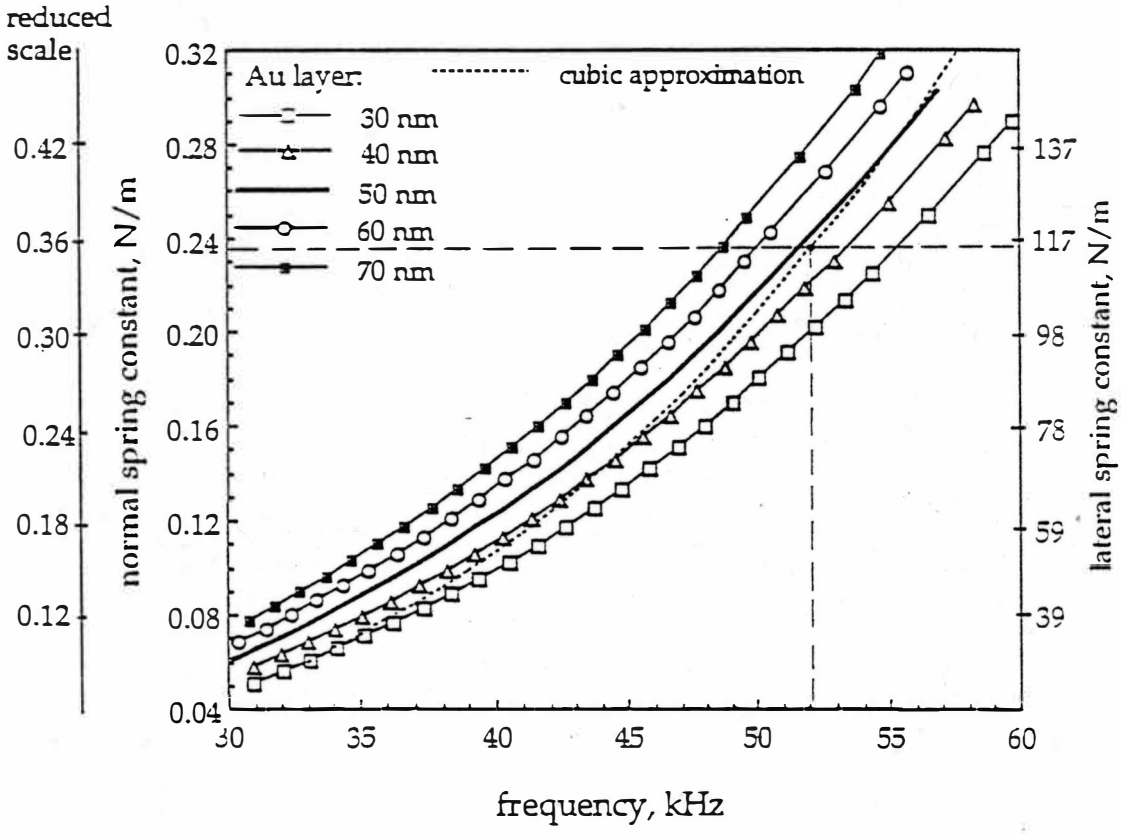

Figure 37. Calibration Plots (Au=const).

best fit was observed by replacements of power exponent of 3 in equations for homogeneous beams with values around 2.6. For this simplified analysis of SPM cantilevers we can propose a simple scaling relationship for typical gold layer thickness of 50 nm in the form:

$$K_n = 8.1x10^{-6} f_o^{2.6} \quad (47)$$

and

$$K_{lat} = 3.96x10^{-3} f_o^{2.6} \quad (48)$$

Obviously that direct assessment of spring constants of ceramic/gold cantilevers without available values of the gold overlay thickness may result in significant miscalculations and actual deviations can reach as much as 40% for cantilevers with various gold overlays. Therefore, while using equation (47) for crude estimations, we recommend determining k_n from the calibration graphs proposed using both gold thickness and resonant frequency measurements.

A family of k (f_o) plots can be fitted by a set of analytical functions. For this analysis a power function $k = A f_o^{\bullet}$ with parameters A and• • being fitted to gold overlay thickness variation in a linear form: $A(h_{Au}) = B + C h_{Au}$. A choice of the linear approximation significantly simplifies the final analytical expression and introduces only minor deviations from the exact solution within the range of gold thickness and resonant frequencies considered here. The final approximation for evaluation of normal spring constant from the known resonant frequency and the gold overlay thickness, therefore, can be presented in the form:

$$K_n = 2.9x10^{-7}(h_{Au} - 10.34) f_o^{(2.77-0.0047h_{Au})} \quad (49)$$

and

$$K_{lat} = 1.42x10^{-4}(h_{Au} - 10.34)f_o^{(2.77-0.0047t_{Au})}$$

(50)

where h_{Au} is in nanometers, f_o is in kiloHertz, and k_n is in N/m. This expression describes correctly a family of calibration plots in the range of resonant frequencies from 30 to 60 kHz for short V-shaped cantilevers. The power exponent in this expression does not follow exact solution, $\alpha = 3$ if $h_{Au} \rightarrow 0$ because of linear approximation used in this local fit. This simplification limits the applicability of analytical expression presented to the range of gold overlay thickness $30 < h_{Au} < 80$ nm where it is valid within accuracy of ± 2%.

The actual calibration procedure should be done in three-stages. First, resonant frequency should be measured by standard SPM analyzing software. Next, the average thickness of gold overlay should be found by SPM imaging of a silicon nitride chip surface from the same wafer with a partially removed gold overlay. Finally, the actual values of spring constants can be read directly from the plot in Figure 37 by finding intersection with the calibration curve for appropriate gold thickness as shown for particular type of cantilevers analyzed in this work.

Several cantilevers were analyzed by Zheng Huang using the added mass and spring-on-spring technique to compare the final results by each method (Huang,

1999). The results from the added mass and spring-on-spring measurments were withing 20% of the calibration curve value. Thus rapid calibration within 20% accuracy using the calibration curves can be expected using the calibration curves.

Several additional circumstances should be considered when applying calibration plot in Figure 37 or using the analytical expressions (49, 50). First, the calibration plot assumes a variation of *ceramic layer thickness* to be primary responsible for variable resonant frequency although gold layer change is the known correction parameter. This is the most probable scenario for composite V-shaped SPM cantilevers as proved by experimental observations for a wide set of wafers.

However, significant variations of gold overlay thickness with virtually constant thickness of the ceramic layer can lead to very different changes of the resonant behavior. We calculated calibration plots for variable gold overlay thickness as a primary cause of changes in the cantilever resonant behavior (Figure 38). A striking feature of this plot is *inverse variation* of spring constant versus resonant frequency. This very different behavior is caused by different contributions of ceramic layer and gold overlay. Increasing ceramic layer thickness causes significant increase of stiffness (due to high E_{SiN}) although adds a little mass (low ceramic density) that should result in increase both k_n and f_o. On the other hand, an increase of gold overlay thickness results in small increase in stiffness (caused by contribution of very low E_{Au}) but significantly increases cantilever mass (due to high gold density) leading to decrease of f_o. Obviously, for some bi-component cantilevers both scenarios can take

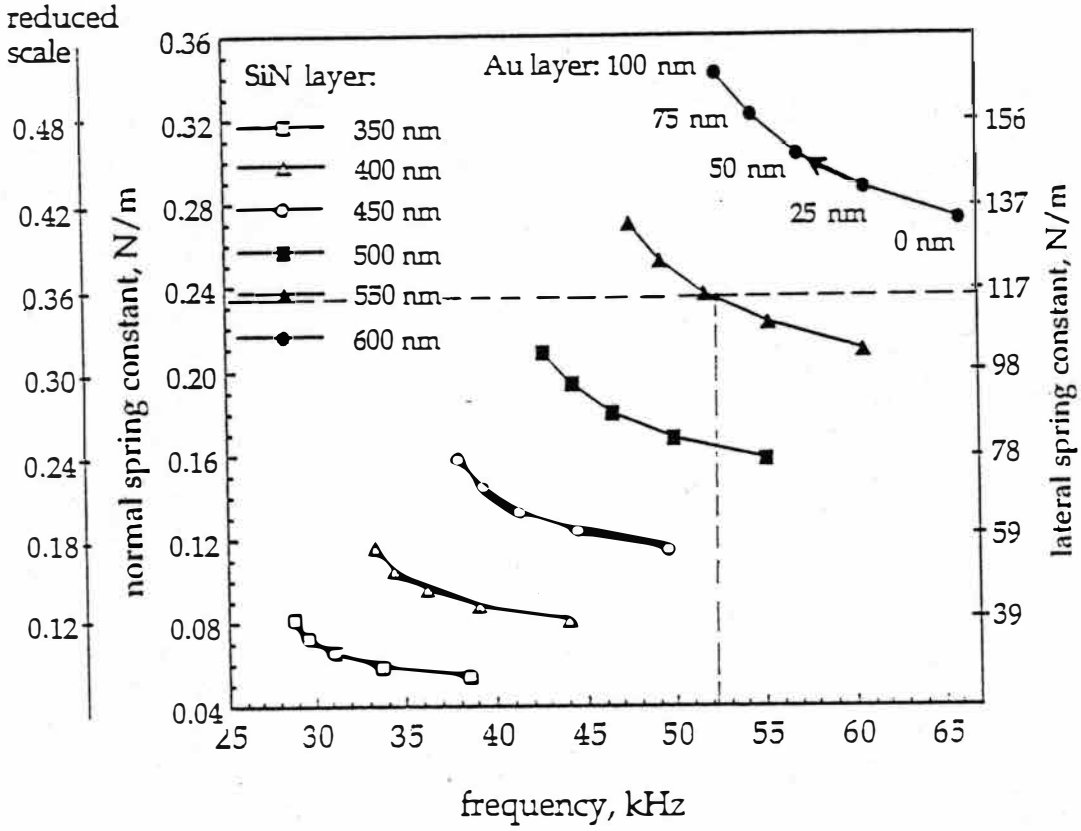

Figure 38. Calibration Plots (Si3N4=const).

place resulting in significant local deviations of corresponding experimental points from simple $k_n \sim f_o^2$ relationship as was observed for selected cantilevers (Cleveland, 1993). Therefore, this plot can be used to supplement the SPM calibration procedure if ceramic layer thickness is known. The knowledge of the gold overlay thickness is not required.

A simple additional correction for variation of spring constant, k_{cor}, caused by variable cantilever length can be used in the form:

$$\frac{k_{cor}}{k_n} = \left(\frac{L_1}{L_o} \right)^3 \quad (51)$$

where L_1 is the length from the base to the tip end for the particular cantilever considered and L_o is the same length for "reference" cantilever used in our calculations (L_o = 108.4 μm). The actual length of cantilevers can be measured by optical microscopy with a high accuracy and correction according eq. (17) can be easily implemented.

CHAPTER XII

APPLICATION EXAMPLES IN PUBLICATIONS

An important test of any new technique is demonstration of their practical application. The following examples clearly show several direct uses of calibrated force measurements. These few early examples will soon be followed by additional applications of calibrated force SPM (Tsukruk and Bliznyuk, 1998). As the surface analysis techniques continue in the transition from quantitative to qualitative methods the validation of specific surface theory and molecular models may be addressed (Chizhik et. al., 1998). Without accurately calibrated cantilevers this would not be possible.

Microelectromechanical systems (MEMS) are tiny machines produced by technology used for fabrication of integrated circuits. At the micron scales of these devices several considerations, which are usually ignored in typical sized machinery, become very important. For example the adhesion of mating parts due to capillary forces can completely disable a MEMS device by sticking them tightly together (Sulouff, 1998).

One approach to reducing these effects that has been investigated in the Tsukruk surface science lab is to attach molecular monolayers to the adjoining surfaces (Tsukruk, Hazel et al., 1998). These functionalized monolayers serve to control chemical and mechanical parameters of the surfaces. These monolayers can

also serve the function of establishing a very consistent which allows easier engineering of devices via the reduction in variables. In addition to control of forces, the employment of molecular layers may make wearless friction possible. By attaching a rigid, plate-like, molecule to the MEMS surfaces by flexible polymer chains, a nano-conforming surface is produced. As the molecular plates adapt to the local topography the peak forces tend to be minimized. If the peak shearing forces are low enough, the bond between molecules will never be broken which implies wearless sliding.

MEMS devices are currently impaired by proportionally very strong adhesion forces between components. Chemical modification of MEMS surfaces can drastically alter adhesive properties. The quantification of the adhesive forces by calibrated SPM allows estimating the degree of functional impairment in these devices due to the excessive contact forces resulting from adhesion. Figure 39 shows that the surface chemistry can vary adhesion by more than an order of magnitude (Tsukruk & Bliznyuk, 1998). The corresponding friction data obtained for the same surfaces shows that higher adhesion does not necessarily correspond to high friction coefficients. Figure 40 shows that the NH2 SAM layer, which displayed very high adhesion, has the median value of friction coefficient. Without calibrated cantilevers the assessing the significance of friction forces vs. adhesion forces would be very difficult. In this case though we reported quantitative values that can be incorporated into the design process.

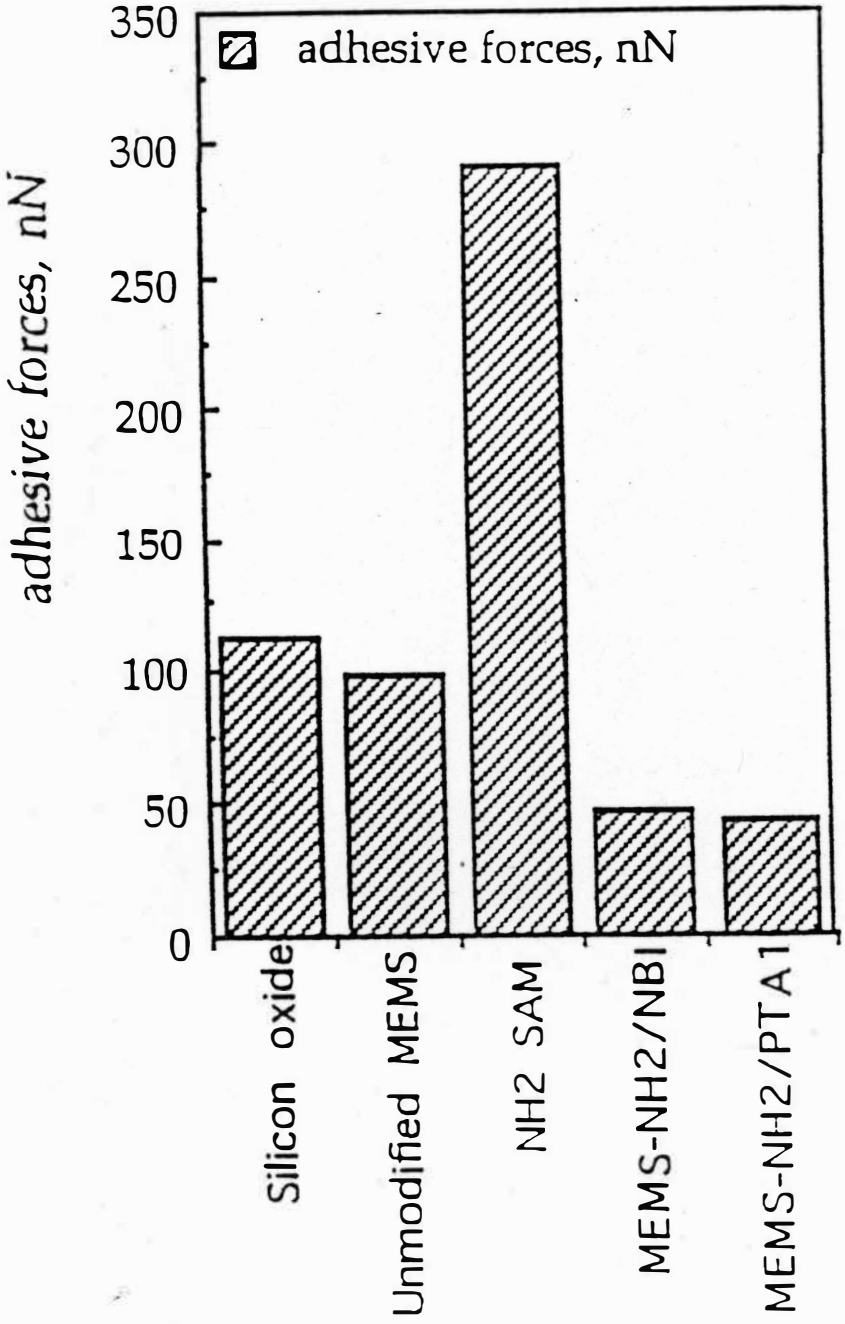

Figure 39. Surface Adhesion.

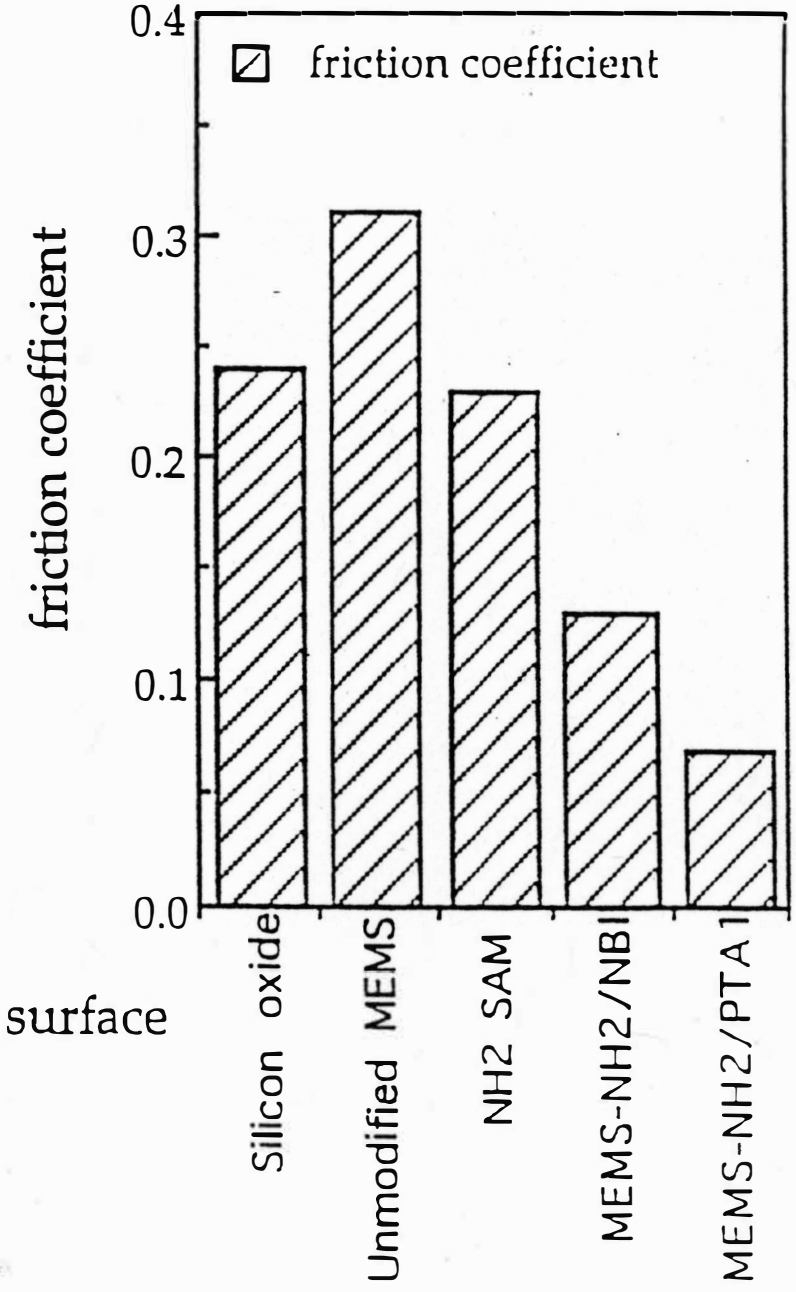

Figure 40. Friction Coefficient.

Furthermore in Figures 41 and 42 "loading curves" for molecular monolayer surfaces are shown. These surfaces were candidates for surface modification to

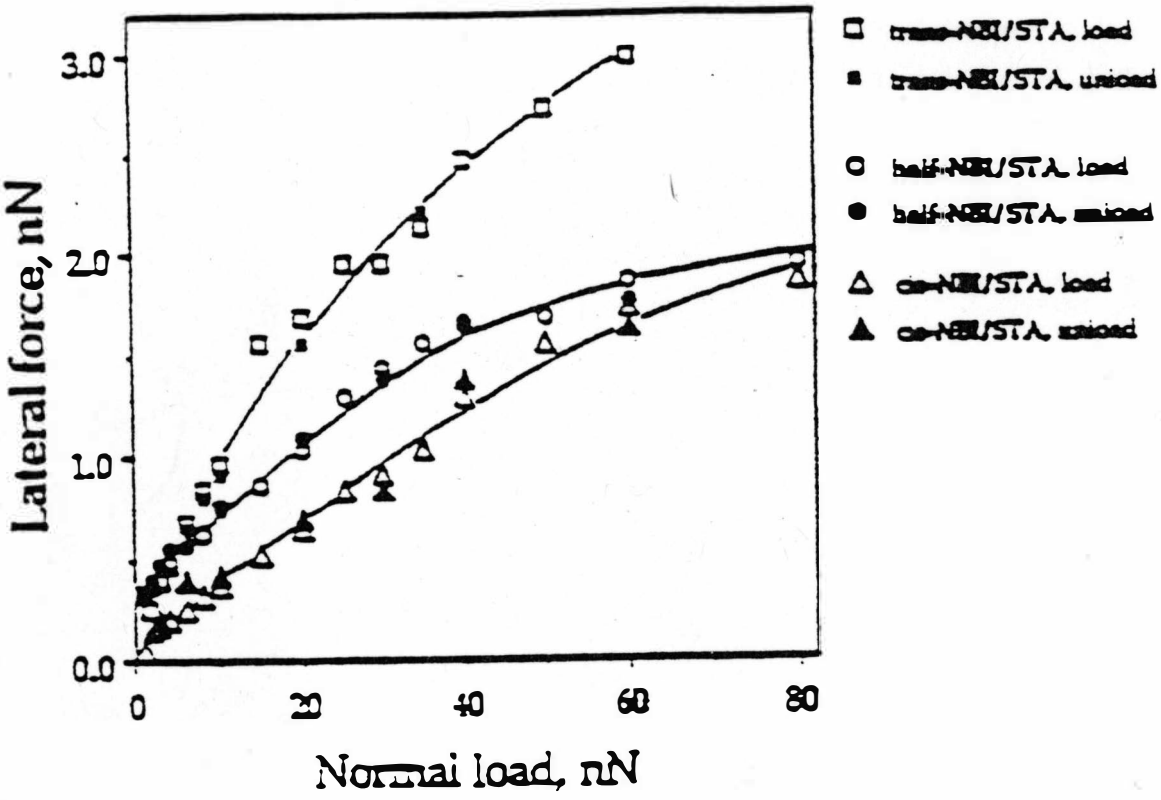

Figure 41. Friction Loading Curves.

prevent stick-slip behavior in mating parts. The dynamics of stick-slip can be tuned out by appropriate matching of friction properties. (Luedema, 1996) This tuning requires assessment of the friction character at a range of surface pressures.

The molecular monolayers display nonlinear behavior in friction force as a function of normal loading (Bliznyuk, Everson, Tsukruk, 1997). The quantitative results allow matching of the loading service to the frictional quality in the design

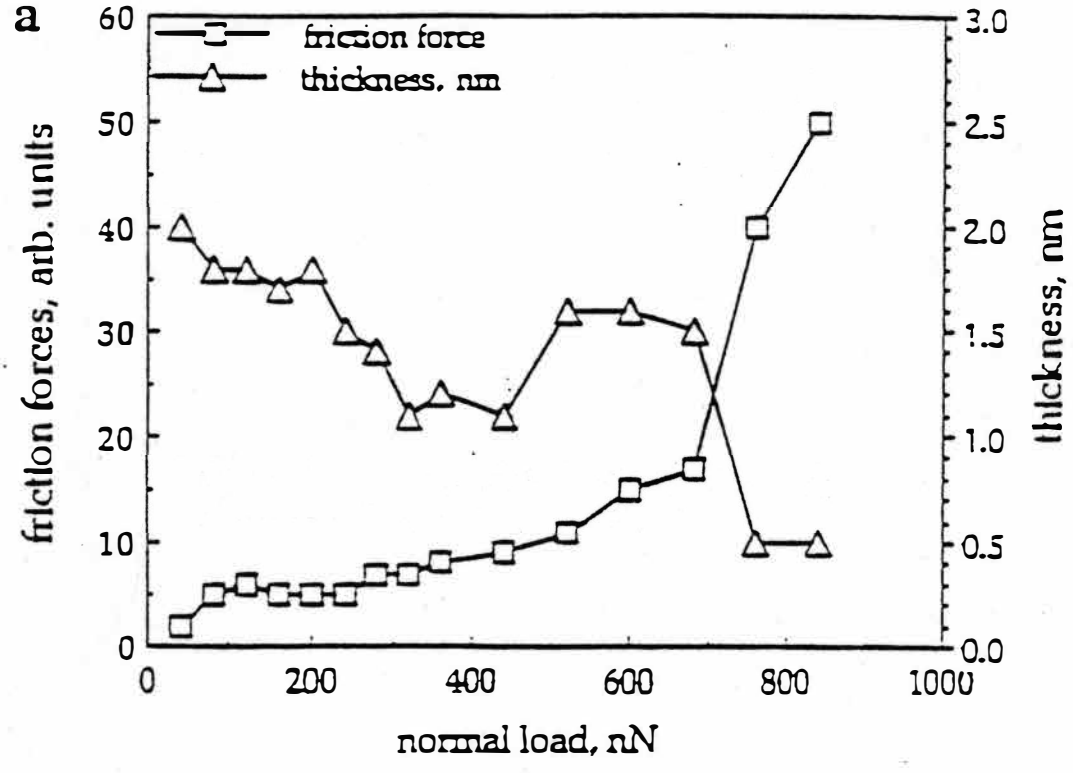

Figure 42. Friction Loading Curves With Transition.

stage. This allows a much better first iteration in the design process which can either shorten the design cycle or allow more complete optimization for a given development time. The alternative available with only qualitative data would be to use a cut and try approach. This engineering guessing often is very expensive due to the greater number of physical iterations in the design process.

A more well defined example of non linear variation of friction with loading is shown in Figure 43. We (Tsukruk, Hazel et. al. 1996) highlight the sudden change in

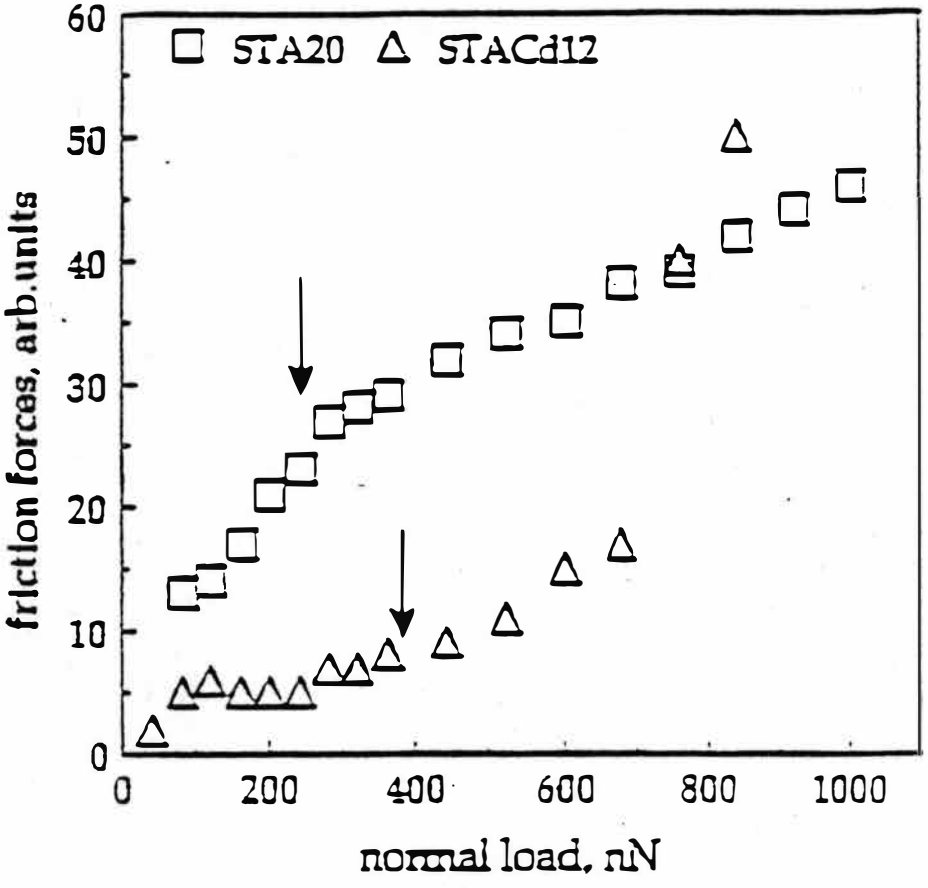

Figure 43. Loading Curves With Reduced Slope Transition.

slope of the data curve at approximately 300 and 400 nN for surfaces of two differently prepared surface monolayers. For employment of these monolayers in real devices the calibrated result allows designers to incorporate the friction characteristics in the early design process which can help refine the design at earlier stages compared to data based on purely qualitative data. Further analysis of the results of frictional forces showed a topographical reorganization of the molecular layer. Figure 44 shows the holes that appeared outside of the area undergoing frictional shearing. This indicates that for surfaces similar to those we studied a critical

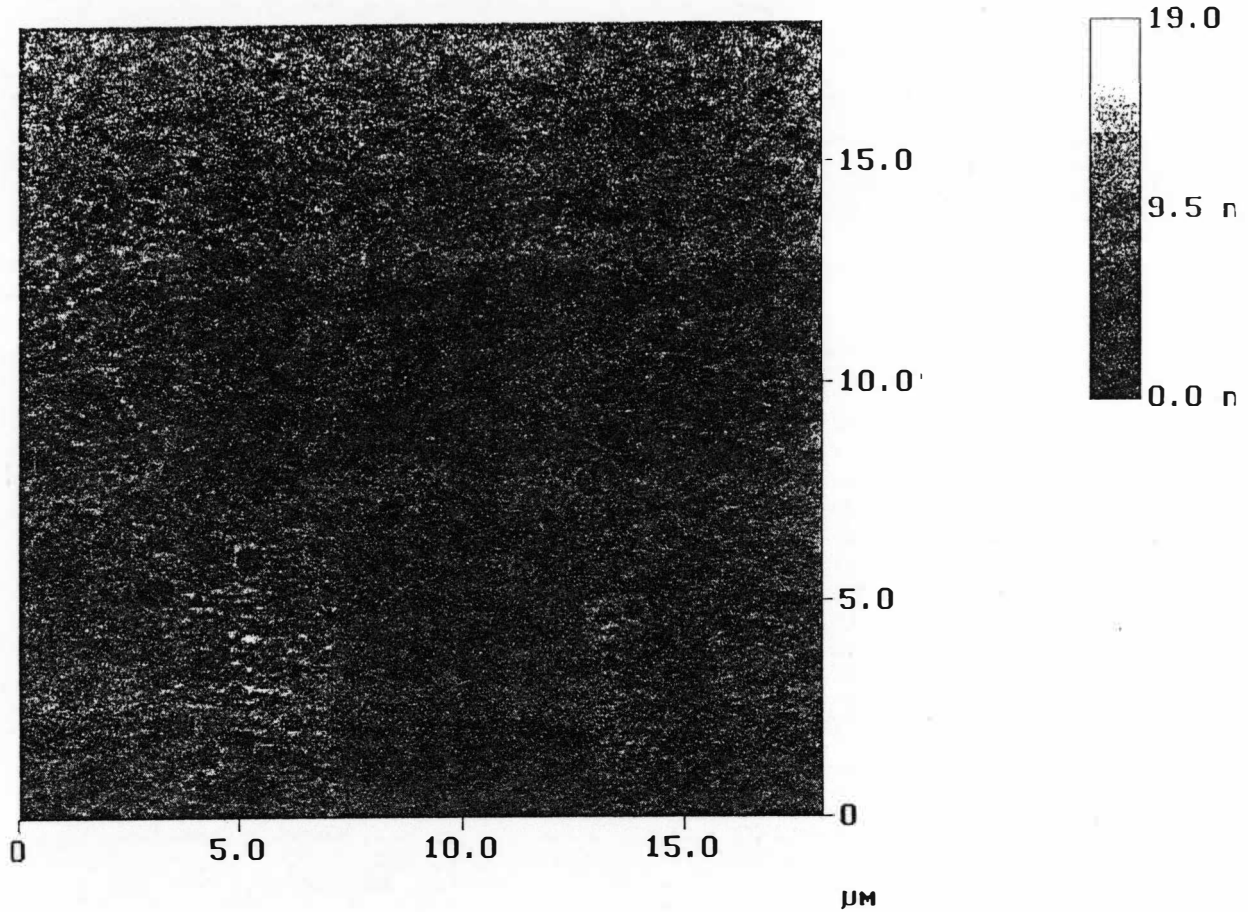

Figure 44. Reorganization of Molecular Monolayers Under Shear Forces.
Source: Tsukruk et. al. (1996)

level of abrasion force exists that will not only damage the area undergoing the abrasion but will also profoundly affect the surrounding area. Our calibrated SPM allows us to specify that the critical force is 300-400nN.

One more example of the advancements needing calibrated cantilevers is the nanomechanical teasing of surfaces. The calibration of forces applied in conjunction with tip topography assessment allows incorporation of theoretical models such as Johnson-Kendal-Roberts' into the nanomechanical measurements (Chizick et al 1998). Nanomechanical materials properties are then made measurable as shown in Figure 45.

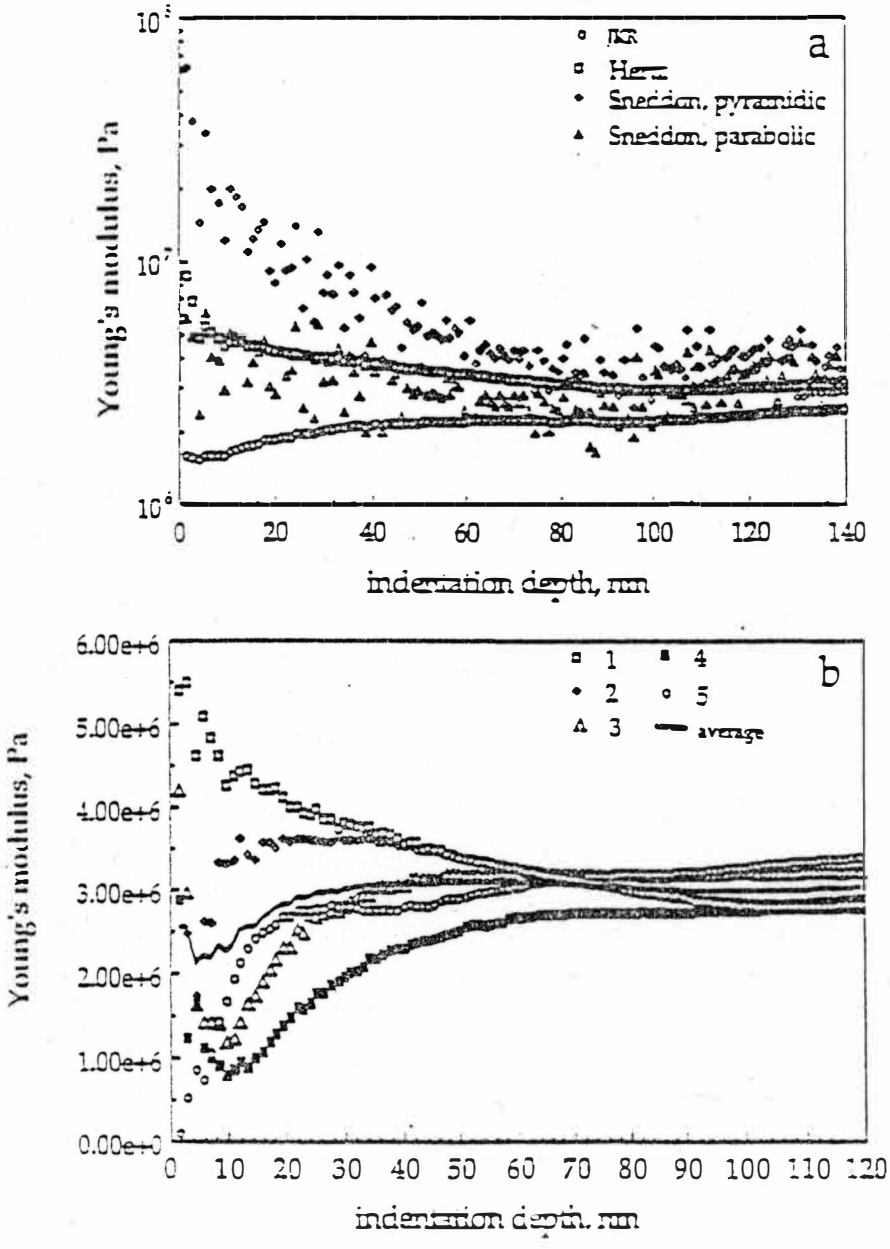

Figure 45. Sample Nanomechanical Data.
Source: Chizhik et al. (1998)

CHAPTER XIII

CONCLUSIONS

We advanced the current calibration precision of SPM cantilever in quantitative measurements of microscopic tribological properties. The approach proposed here includes a combination of finite element analysis calculations and resonant frequency measurements and is used to determine spring constants of the SPM cantilevers. Special attention is paid to the bi-component nature of ceramic/gold V-shaped cantilevers. The Si_3N_4 and Au layers are combined analytically into a equivalent single composite layer using parallel beam theorem and section transformation. This approach provides more accurate evaluation of mechanical properties of composite cantilever beams than standard linear approximation. Effective Young's modulus of the composite Si_3N_4 - Au beam is determined to be within 172 to 185 GPa through assimilation of FEA and resonant frequency measurements.

FEA parameters are compared to several analytical estimates and a new modified equation is proposed for the V-shaped cantilever (eqs. 13, 14) that gives the ratio k_n/k_t close to the full FEA solution. This ratio allows direct evaluation of friction coefficients from friction force microscopy data which is independent of thickness, Young's modulus, and density of microfabricated cantilevers.

The PBA results for normal spring constants are fairly good if the material properties are known. As mentioned earlier this is rarely the case. However the PBA model does not fare so well in estimating the torsional spring constant. As the leg angle is reduced the error becomes larger. The PBA analysis has deficiencies in that it does not model the torsion–bending due to the leg angle and it does not account for the effects of the connection between the legs near the probe tip.

Calibration plots in the form $k \sim f_o^{\bullet}$ are generated for convenient assessments of both normal and lateral (torsion) spring constants of bi-component 100 μm V-shaped SPM cantilevers considered in this work by measuring their resonant frequencies and thickness of gold overlay. This approach does not require additional extensive measurements of cantilever geometry and properties. Expected uncertainty of this calibration procedure is within 10 - 15%. The approximate solution is presented that can be used for numerical estimation of spring constants from known resonant frequency and gold overlay thickness. The calibration plots presented take into account this complex behavior and make more accurate assessment of the SPM cantilever spring parameters available. Application of these calibration plots in the reduced scale form towards V-shaped cantilevers fabricated from other materials is also possible.

A complex relationship between resonant frequency measured and spring constants is revealed in scaling form $k \sim f_0^{\bullet}$ where $\bullet$ is about 2.60 for typical range of gold thicknesses. The observed behavior modifies all property-geometry relationships

derived for homogeneous beams widely applied to composite cantilevers. These deviations are caused by the bi-component nature of cantilevers composed of ceramic layer and gold overlay.

Appendix A

Analytical Derivation of the Lateral-to-Normal Spring Constant Ratio for V-shaped Cantilevers

$$SE\_half := \frac{1}{8}\frac{M^2 L}{E I\_} + \frac{t^2 L}{G J}$$

$$M := T\cos(\theta)$$

$$t := T\sin(\theta)$$

$$I\_ := \frac{1}{12} w h^3$$

$$J := \frac{1}{3} w h^3$$

$$G := \frac{E}{2 - 2\nu}$$

$$SE := 3\frac{T^2 \cos(\theta)^2 L}{E w h^3} + 6\frac{T^2 \sin(\theta)^2 L (2 - 2\nu)}{E w h^3}$$

$$Kt := \frac{1}{6\frac{\cos(\theta)^2 L}{E w h^3} + 12\frac{\sin(\theta)^2 L (2 - 2\nu)}{E w h^3}}$$

$$Kts := \frac{1}{6}\frac{E w h^3}{L\left(-3\cos(\theta)^2 + 4 - 4\nu + 4\nu\cos(\theta)^2\right)}$$

$$Kn := \frac{1}{2}\frac{E w h^3}{L^3}$$

$$Kratio := 2\frac{L^3}{\left(6\frac{\cos(\theta)^2 L}{E w h^3} + 12\frac{\sin(\theta)^2 L (2 - 2\nu)}{E w h^3}\right) E w h^3}$$

$$Kratios := \frac{1}{3} \frac{L^2}{-3\cos(\theta)^2 + 4 - 4\nu + 4\nu\cos(\theta)^2}$$

$$Klatt := \frac{1}{6} \frac{E\,w\,h^3}{L\left(-3\cos(\theta)^2 + 4 - 4\nu + 4\nu\cos(\theta)^2\right) H^2}$$

$$Klat := \frac{1}{3} \frac{L^2\,Knexp}{\left(-3\cos(\theta)^2 + 4 - 4\nu + 4\nu\cos(\theta)^2\right) H^2}$$

Appendix B

Cantilever Calibration Procedure for Digital Instruments Nanoscope SPM

AFM Friction Force Calibration and Measurement

Calibration of AFM Cantilever in Bending.

Install the cantilever and measure the resonant frequency of your cantilever using cantilever tune in the tapping mode.(ref. Dimension™ 3000 Instruction Manual pp. 8-7 to 8-10 and Command Reference Manual pp. 4-17 to 4-24) Go to "Manual>>" mode and set the parameters as indicated in the chart below.

Cantilever	Drive Frequency	Sweep Width	Drive Amplitude	Setpoint
DI 100N	52Khz	2Khz	300mV	0
DI 200N	18Khz	2Khz	300mV	0
DI 100W				
DI 200W				

The strongest resonant peak should occur near the drive frequency given in the chart. Using auto tune should result in a precise value for the resonant peak frequency. Record this value on the cantilever calibration worksheet. Also record the thickness of the Au coating. Calculate the spring constant. If you type this value into the "spring const" box of the "Spring" window (button in the "Cantilever Tune" window) you will override the less accurate simple internal calculation of spring constant. However there is no provision in the software of the Dimension 3000 that will account for adhesion or repulsion of the tip.

Measurement of Adhesion Forces.

Switch to contact mode and engage the tip. Select the Force calibration mode. In the "Z Scan Controls" window set "Trigger Mode" to "off". In the "Z scan" window set "units" to "volts." The "Feedback Controls" window should have "setpoint" of 0.0 and "Input attenuation" of 8x. You may now set "Z range" in the "Channel 1" window to 20 volts. In the vertical bar near the right side of the force curve graph (left screen) two white lines indicate the Z piezo travel. Use the "Z scan start" and "Z scan size" to change the Z piezo travel so that the force curve plot is positioned left to right. If the one of the white lines in the vertical bar is at the top you have reached the retracting limit of travel for the piezo element. Use the "Motor control" window command "Tip up" to raise the piezo tube so it can operate in its usable range. You may want to adjust the Graph range now to scale the force curve vertically for easier viewing. The "setpoint" may be adjusted to move the force curve up or down in the graph. Use the mouse to rubber band a line on the force curve and automatically set the sensitivity. Switch "units" to metric and record the value shown in the "Sensitivity" box on the calibration worksheet. Switch back to units of "volts". On the force graph measure the vertical distance between the lowest voltage and the voltage for the free cantilever. Record this as the "pull off voltage" on the worksheet. Zero the "setpoint" again and record the voltage for the cantilever when it is not in contact with the surface V_{free}. (ref. Dimension™ 3000 Instruction Manual pp. 8-7 to 8-10 and Command Reference Manual pp. 4-1 to 4-17)

$$F_{normal} = F_{adhesion} + F_{force} = V_{pulloff}\frac{K_v}{Sens} + \left(V_{set} - V_{free}\right)\frac{K_v}{Sens} = \left(V_{pulloff} + V_{set} - V_{free}\right)\frac{K_v}{Sens}$$

Calibration of Cantilever in for Lateral Forces.

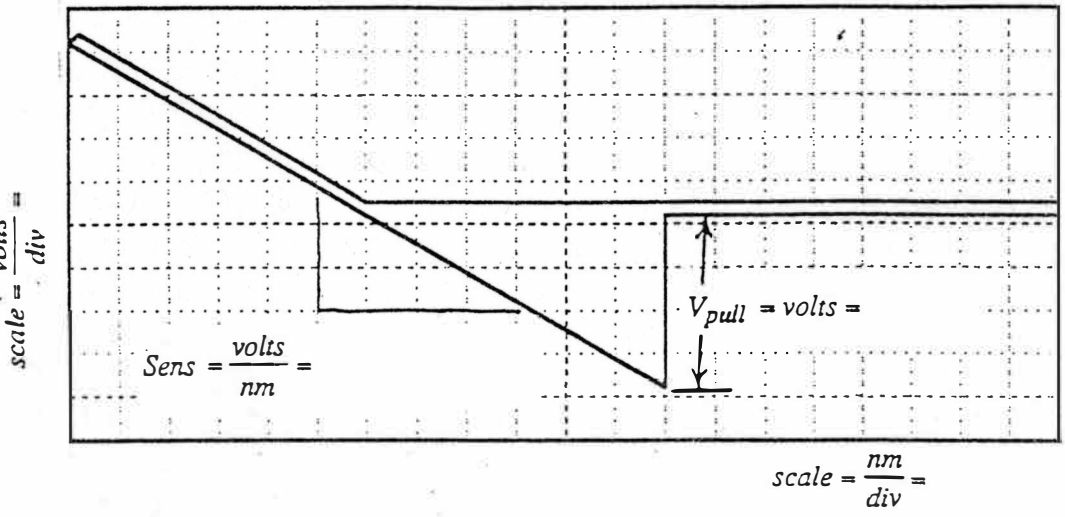

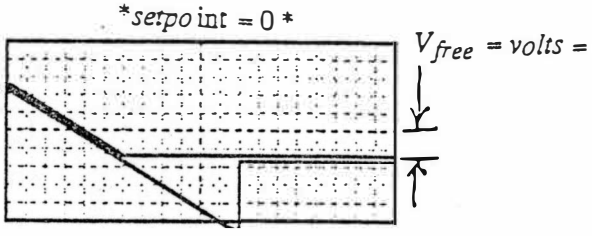

$$F_{ad} = \frac{K_n}{Sens} V_{pull} = \frac{\frac{N}{m}}{\frac{volts}{nm}} volts =$$

$$F_{spring} = \frac{K_n}{Sens}\left(V_{set} - V_{free}\right) =$$

$$F_{norm} = F_{ad} + F_{spring} = \frac{K_n}{Sens}\left(V_{pul} + V_{set} - V_{free}\right) =$$

$V_{pull} = volts =$

$$Sens = \frac{volts}{nm} =$$

$$scale = \frac{volts}{div} =$$

$$scale = \frac{nm}{div} =$$

$V_{free} = volts =$

$$F_{ad} = \frac{K_n}{Sens} V_{pull} = \frac{\frac{N}{m}}{\frac{volts}{nm}} volts =$$

$$F_{spring} = \frac{K_n}{Sens}\left(V_{set} - V_{free}\right) =$$

*setpoint = 0 *

After determining the normal spring constant calculate K_{lat} using the K_{lat}/Kn value for the cantilever from the chart or from calculation by the given formula. Engage the surface with channel 1 data type set to "height" and channel 2 data type set to "friction." Set the "Real time planefit" to "offset." Also set the scan angle to 90 degrees. When you have stable scanning enter "scope mode" in the real time menu. Reduce the "Scan size" to ≈5nm. Adjust (?) and (?) to get the friction loop vertically within the friction graph. Readjust the "Scan size" to get a friction loop similar to the one shown on the worksheet. Find the slope of the non-sliding portion of the curve in units of nm/div. Record the vertical and horizontal scales and calculate the value of $Sens_{lat}$.. $Sens_{lat}$ units are volts of change in the left-right photodetector's output per nm of horizontal tip motion. Then the equations below can be used to calculate lateral force in nN.

$$F_{lat} = \frac{K_{lat}}{Sens_{lat}} \Delta V_{lat}$$

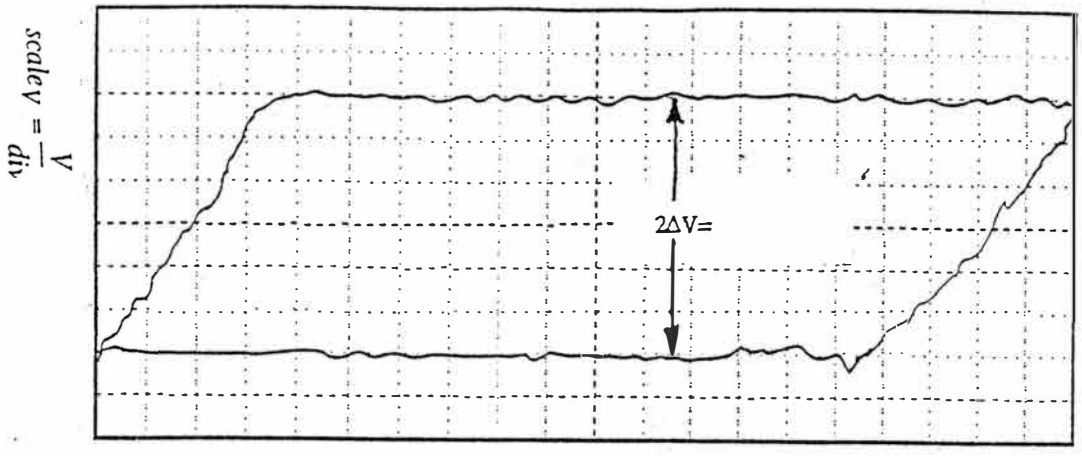

$$scale_{nm} = \frac{nm}{div} =$$

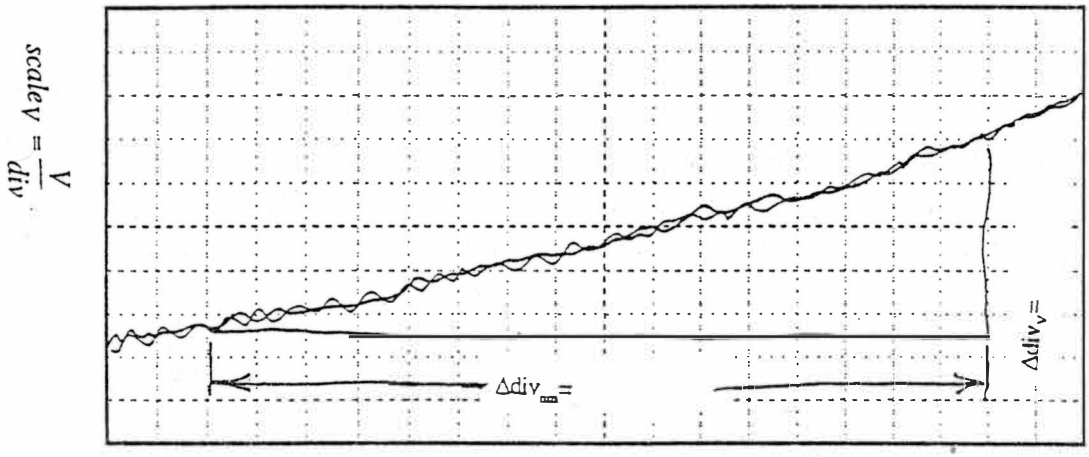

$$scale_{nm} = \frac{nm}{div} =$$

$$Sens_{lat} = \frac{\Delta V_{lat}}{\Delta X_{lat}} = \frac{\Delta div_V scale_V}{\Delta div_{nm} scale_{nm}} = \frac{volts}{nm} =$$

$$F_{lat} = K_{lat} \Delta X = \frac{K_{lat}}{Sens_{lat}} \Delta V = \frac{\frac{N}{m}}{\frac{volts}{nm}} volts = nN =$$

BIBLIOGRAPHY

Allison, D. P., Kerper, P. S., Doktycz, M. J., Spain, J. A., Modrich, P., Larimer, F. W., Thundat, T. and Warmack, R. J. (1996). "Direct atomic force microscope imaging of EcoRi endonuclease site specifically bound to plasmid DNA molecules." Proc. Natl. Acad. Sci. USA 93: 8826-8829.

Basire, C. and Fretigny, C. (1999). "Atomic force microscopy for the study of adhesive and mechanical properties of viscoelastic materials." Polymers and surfaces.

Beladidi, S., Girard, P. and Leveque, G. (1997). "Electrostatic forces acting on the tip in atomic force microscopy: Modelization and comparison with analytic expressions." Journal of Aplied Physics 81(3): 1023-1029.

Bosenung, E., Heuberger, M. and Dietler, G. (1994). "Energy dissipation during nanoscale indentation of polymers with an atomic force microscope." Applied Physics Letters 64(26): 3566-3568.

Burnham, N. A., Behrend, O. P., Oulevey, F., Gremaud, G., Gallo, P.-J., Gourdon, D., Dupas, E., Kulik, A. J., Pollock, H. M. and Briggs, G. A. D. (1997). "How does a tip tap?" Nanotechnology 8: 67-75.

Burnham, N. A., Gremaud, G., Kulik, A. J., Gallo, P.-J. and Oulevey, F. (1996). "Materials' properties measurements: Choosing the optimal scanning probe microscope configuration." Journal of Vacuum Science Technology B 14(2): 1308-1312.

Burnham, N. A., Kulik, A. J., Gremaud, G., Gallo, P.-J. and Oulevey, F. (1996). "Scanning local-acceleration microscopy." Journal of Vacuum Science Technology B 14(2): 794-799.

Butt, H. J., Siedle, P., Seifert, K., Fendler, K., Seeger, T., Bamberg, E., Weisenhorn, A. L., Goldie, K. and Engel, A. (1993). "Scan speed limit in atomic force microscopy." Journal of Microscopy 169: 75-84.

Cleveland, J. P., Manne, S., Brocek, D. and Hansma, P. K. (1993). "A nondestructive method for determining the spring constant of cantilevers for scanning force microscopy." Review of Scientific Instruments 64(2): 403-405.

Dai, H., Hafner, J. H., Rinzler, A. G., Colbert, D. T. and Smalley, R. E. (1996).

"Nanotubes as nanoprobes in scanning probe microscopy." Nature 384: 147-153.

DeRose, J. A. and Revel, J.-P. (1998). "Studying the surface of soft materials (live cells) at high resolution by scanning probe microscopy: Challenges faced." Thin Solid Films 331: 194-202.

DeVecchio, D. and Bhushan, B. (1997). "Localized surface elasticity measurements using an atomic force microscope." Review of Scientific Instruments 68(12): 4498-4505.

Drake, B., Prater, C. B., Weisenhorn, A. L., Gould, A. C., Albrecht, T. R., Quate, C. F., Cannell, D. S., Hansma, H. G. and Hansma, P. K. (1989). "Imaging crystals, polymers, and processes in water with the atomic force microscope." Science 243: 1586-1588.

Fang, J., Knobler, C. M., Gingery, M. and Eiserling, F. A. (1997). "Imaging bacteriophage T4 on patterned organosilane monolayers by scanning force microscopy." Journal of Physical Chemistry B 101(43): 8692-8695.

Florin, E.-L., Moy, V. T. and Gaub, H. E. (1994). "Adhension forces between individual ligand-receptor pairs." Science 264: 415-417.

Florin, E.-L., Radmacher, M., Fleck, B. and Gaub, H. E. (1994). "Atomic force microscope with magnetic force modulation." Review of Scientific Instruments 65(3): 639-643.

Fretigny, C., Basire, C. and Granier, V. (1997). "Determination of complex modulus by atomic force microscopy." Journal of Applied Physics 82(1): 43-48.

Goo, N. S. and Kim, S. J. (1997). "Dynamic contact analysis of laminated composite plates under low-velocity impact." AIAA Journal 35(9): 1518-1521.

Hansma, P. K., Cleveland, J. P., Radmacher, M., Walters, D. A., Hillner, P. E., Bezanilla, m., Fritz, M., Vie, D., Hansma, H. G., Prater, C. B., Massie, J., Fukunaga, L., et al. (1994). "Tapping mode atomic force microscopy in liquids." Applied Physics letters 464(13): 1738-1740.

Hazel, J. L. and Tsukruk, V. V. (1998). "Friction force microscopy measurements: Normal and torsional spring constants for V-shaped cantilevers." Journal of Tribology 120(4): 814-819.

Henderson, R. M., Schneider, S., Li, Q., Hornby, D., White, S. J. and Oberleithner, H. (1996). "Imaging ROMK1 inwardly rectifying ATP-sensitive K+ channel

protein using atomic force microscopy." Proc. Natl. Acad. Sci. USA 93: 8756-876).

Hinterdorfer, p., Baumgartner, W., Gruber, H. J., Schilcher, K. and Schindler, H. (1996). "Detection and localization of individual antibody-antigen recognition events by atomic force microscopy." Proc. Natl. Acad. Sci. USA 93: 3477-3481.

Howard, A. J., Rye, R. R. and Houston, J. E. (1996). "Nanomechanical basis for imaging soft materials with tapping mode atomic force microscopy." Journal of Applied Physics 79(4): 1885-1890.

Hudson, J. E. and Abruna, H. D. (1996). "Electrochemically controlled adhension in atomic force spectroscopy." Journal of the American Chemical Society 118(26): 6303-6304.

Hues, S. M., Draper, C. F. and Colton, R. J. (1994). "Measurement of nanomechanical properties of metals using the atomic force microscope." Journal of Vacuum Science Technology B 12(3): 1-4.

Hutter, J. L. and Bechhoefer, J. (1993). "Calibration of atomic-force microscope tips." Review of Scientific Instruments 64(7): 1868-1873.

Ito, T., Namba, M., Buhlmann, P. and Umezawa, Y. (1997). "Modification of silicon nitride tips with trichlorosilane self-assembled monolayers (SAMs) for chemical force microscopy." Langmuir 13(16): 4323-4332.

Itoh, T., Ohashi, T. and Suga, T. (1996). "Noncontact scanning force microscopy using a direct-oscillating piezoelectric microcantilever." Journal of Vac. Sci. Technol. B 14(3): 1577.

Jarvis, S. p., Yamada, H., Yamamoto, S.-I., Tokumoto, H. and Pethica, J. B. (1996). "Direct mechanical measurement of interatomic potentials." Nature 384: 247-249.

Johnson, C. A. and Lenhoff, A. M. (1996). "Adsorption of charged latex particles on mica studied by atomic force microscopy." Journal of colloid and interface science 179: 587-599.

Kerssemakers, J. and De Hosson, J. T. M. (1996). "Influence of spring stiffness and anisotropy on stick-slip atomic force microscopy imaging." Journal of Applied Physics 80(12): 623-.

Knapp, H. F., Wiegrabe, W., Heim, M., Eschrich, R. and Guckenberger, R. (1995). "Atomic force microscope measurements and manipulation of Langmuir-

Blodgett films with modified tips." Biophysical Journal 69(708-715).

Kuhle, A., Sorensen, A. H. and bohr, J. (1997). "Role of attractive forces in tapping tip force microscopy." Journal of Applied Physics 81(10): 6562-6569.

Labardi, M., Allegrini, M., Salerno, M., Frediani, C. and Ascoli, C. (1994). "Dynamical friction coefficient maps using a scanning force and friction microscope." Applied Physics A: Solids and Surfaces: 3-10.

Li, Y. Q., Tao, N. J., Pan, J., Garcia, A. A. and Lindsay, S. M. (1993). "Direct measurement of interaction forces between colloidal particles using the scanning force microscope." Langmuir 9(3): 637-641.

Majumdar, A., Lai, J., chandrachood, M., Nakebeppu, O., Wu, Y. and Shi, Z. (1995). "Thermal imaging by atomic force icroscopy using thermocouple cantilever probes." Review of Scientific Instruments 66(6): 3584.

Marti, A., Hahner, G. and Spencer, N. D. (1995). "Sensitivity of frictional forces to ph on a nonometer scale: A lateral force microscopy study." Langmuir 11: 4632-4635.

Mate, C. M., McClelland, G. M., Erlandsson, R. and Chiang, S. (1987). "Atomic-scale friction of a tungsten tip on a graphite surface." Physical Review Letters 59(17): 1942-1945.

Noy, A., Frisbie, C. D., Rozsnyai, L. F., Wrighton, M. S. and Lieber, C. M. (1995). "Chemical force microscopy: Exploiting chemically-modified tips to quantify adhension, friction, and functional group distributions in molecular assemblies." Journal of the American Chemical Society 117: 7943-7951.

Noy, A., Sanders, C. H., Vezenov, D. V., Wong, S. S. and Lieber, C. M. (1998). "Chemically-sensitive imaging in tapping mode by chemical force microscopy: Relationship between phase lag and adhesion." Langmuir 14(7): 1508-1511.

Noy, A., Vezenov, D. V. and Lieber, C. M. (1997). "Chemical force microscopy." Annual Review of Material Science 27: 381-421.

O'Connor, S. D., Gamble, R. C., Eby, R. K. and Baldeschwieler, J. D. (1996). "Noise reduction in atomic force microscopy: Resonance contact mode." Review of Scientific Instruments 64(2): 393-396.

Ohnesorge, F. and Binning, G. (1993). "True atomic resolution by atomic force microscopy through repulsive and attractive forces." Science 260: 1451-1455.

Ortiz, J. L. and Barhorst, A. A. (1997). "Closed-form modeling of fluid-structure interaction with nonlinear sloshing: Potential flow." AIAA Journal 35(9): 1510-1517.

Oulevey, F., Gremaud, G., Semoroz, A., Kulik, A. J., Burnham, N. A., Dupas, E. and Gourdon, D. (1998). "Local mechanical spectroscopy with nanometer-scale lateral resolution." Review of Scientific Instruments 69(5): 2085-2094.

Park, S. B. and Carman, G. P. (1997). "Tailoring the properties of piezoelectric ceramics: Analytical." International Journal of Solids Structures 44(26): 3385-3399.

Pedersen, H. G., Hoj, J. W. and Engell, J. (1998). Measuring forces between alfa-A1203 surfaces using the atomic force microscope, Institute of Mineral Industry, Technical University of Denmark.

Pfeiffer, F. (1996). "Complementarity problems of stick-slip vibrations." Journal of Vibration and Accoustics 118: 177-183.

Pharr, G. M., Oliver, W. C. and Brotzen, F. R. (1992). "On the generality of the relationship among contact stiffness, contact area, and elastic modulus during indentation." Journal of Material Research 7(3): 613-617.

Putman, C. A. J., Van Der Werf, K. O., De Grooth, B. G. and Van Huist, N. F. (1994). "Tapping mode atomic force microscopy in liquid." Appl. Phys. Lett. 64(18): 2454-2456.

Rabe, U., Janser, K. and Arnold, W. (1996). "Vibrations of free and surface-coupled atomic force microscope cantilevers: Theory and experiment." Review of Scientific Instruments 67(9): 3281-3293.

Radmacher, M., Cleveland, J. P., Fritz, M., Hansma, H. G. and Hansma, P. K. (1994). "Mapping interaction forces with atomic force microscope." Biophysical Journal 66: 2159-2165.

Radmacher, M., Fritz, M., Cleveland, J. P., Walters, D. and Hansma, P. K. (1994). "Imaging adhension forces and elasticity of lysozyme adsorbed on mica with the atomic force miroscope." Langmuir 10(10): 3809-3814.

Radmacher, M., Fritz, M., Kacher, C. M., Cleveland, J. P. and Hansma, P. K. (1996). "Measuring the viscoelastic properties of human platelets with the atomic force microscope." Biophysical Journal 70: 556-567.

Radmacher, M., Tillmann, R. W., Fritz, M. and Gaub, H. E. (1992). "From molecules

to cells: Imaging soft samples with the atomic force microscope." Science 257: 1900-1905.

Radmacher, M., Tillmann, R. W. and Gaub, H. E. (1993). "Imaging viscoelasticity by force modulation with the atomic force microscope." Biophysical Journal 64: 735-742.

Rief, M., Gautel, M., Oesterhelt, F., Fernandez, J. M. and Gaub, H. E. (1997). "Reversible unfolding of individual titin immunoglobulin domains by AFM." Science 26676: 1109-1112.

Rief, M., Oesterhelt, O., Heymann, B. and Gaub, H. E. (1997). "Single molecule force spectroscopy on polysaccharides by atomic force microscopy." Science 275: 1295-1297.

Sader, J. E., Larson, I., Mulvaney, P. and White, L. R. (1995). "Method for the calibration of atomic force microscope cantilevers." Review of Scientific Instruments 66(7): 3789-3798.

Shao, L., Tao, N. J. and Leblanc, R. M. (1997). "Probing the microelastic properties of nanobiological particles with tapping mode atomic force microscopy." Chemical Physics Letters 273: 37-41.

Siedle, P. and Butt, H.-J. (1995). "Artifacts in force measurements with the atomic force microscopy due to digitalization." Langmuir 11(4): 1065-1067.

Sinniah, S. K., Steel, A. B., Miller, C. J. and Reutt-Robey, J. E. (1996). "Solvent exclusion and chemical contrast in scanning force microscopy." Journal of the American Chemical Society 118(37): 8925-8931.

Smith, D. P. E. (1995). "Limits of force icroscopy." Review of Scientific Instruments 66(5): 3191-3195.

Smith, S. T. and Howard, L. P. (1994). "A precision, low-force balance and its application to atomic force microscope probe calibration." Review of Scientific Instruments 65(4): 903-909.

Stalder, A. and Durig, U. (1995). "Nanoguitar: Oscillating string as force sensor." Review of Scientific Instruments 66(6): 3576-3579.

Tamayo, J. and Garcia, R. (1996). "Deformation, contact time, and phase contrast in tapping mode scanning force misroscopy." Langmuir 12: 4430-4435.

Tao, N. J., Lindsay, S. M. and Lees, S. (1992). "Measuring the microelastic properties

of biological material." Biophysical Journal 63: 1165-1169.

Tapson, J. and Greene, J. R. (1997). "The resonant behavior of segmented piezoceramic tubes." Review of Scientific Instruments 68(7): 2797-2799.

Taylor, M. E. (1993). "Dynamics of piezoelectric tube scanners for scanning probe microscopy." Review of Scientific Instruments 64(1): 154-158.

Tentschert, J., Fei, L., Siriwardane, H. and Fraundorf, P. "In situ monitoring of scanned probe tip shape using nuclear track pits." .....

Tsukruk, V. V. and Bliznyuk, V. N. (1998). "Adhesive and friction forces between chemically modified silicon and silicon nitride surfaces." Langmuir 14(2): 446-455.

Tsukruk, V. V., Bliznyuk, V. N., Hazel, J. and Visser, D. (1996). "Organic molecular films under shear forces: Fluid and solid langmuir monolayers." Langmuir 12(20): 4840-4849.

Tsukruk, V. V., Nguyen, T., Lemieux, M., Hazel, J., Weber, W. H., Shevchenko, V. V., Klimenko, N. and Sheludko, E. "Tribological properties of modified MEMS surfaces."

Umehara, Y., Ogiso, Y., Chihara, K., Mukasa, K. and Russell, P. E. (1995). "Method for evaluating sharpeness of tip apex of a cantilever for the atomic force microscope." Review of Scientific Instruments 66(1): 269-270.

van der Vegte, E. W. and Hadziioannou, G. (1997). "Scanning force microscopy with chemical specificity: An extensive study of chemically specific tip-surface interactions and the chemical imaging of surface functional groups." Langmuir 13(16): 4357-4368.

Vanlandingham, M. R., McKnight, S. H., Palmese, G. R., Eduljee, R. F., Gillespie, J. W., Jr. and McCulough, R. L. (1997). "Relating elastic modulus to indentation response using atomic force microscopy." Journal of Materials Science Letters 16: 117-119.

Vanlandingham, M. R., McKnight, S. H., Palmese, G. R. Elings, J. R. Huang, X., Bogetti, T. A., Eduljee, R. F., and Gillespie, J. W., Jr. "Nanoscale indentation of polymer systems using the atomic force microscope." Journal of Adhesion 64(1-4): 31-59.

Vezenov, D. V., Noy, A., Rozsnyai, L. F. and Lieber, C. M. (1997). "Force titrations and ionization state sensitive imaging of functional groups in aqueous solutions

by chemical force microscoopy." Journal of the American Chemical Society 119(8): 2006-2015.

Villarrubia, J. S. (1997). "Algorithms for scanned probe microscope image simulation, surface reconstruction, and tip estimation." Journal of Research of the National Institute of Standards and Technology 102(4): 425-454.

Walters, D. A., Cleveland, J. P., Thomson, N. H. and Hansma, P. K. (1996). "Short cantilevers for atomic force microscopy." Review of Scientific Instruments 64(10): 3583-3590.

Weigert, S., Dreier, M. and Hegner, M. (1996). "Frequency shifts of cantilevers vibrating in various media." Applied Physics Letters 69(4): 2834-2836.

Willemsen, O. H., Snel, M. M. E., Kuipers, L., Figdor, C. O., Greve, J. and De Grooth, B. G. (1999). "A physical approach to reduce nonspecific adhension in molecular recognition atomic force microscopy." Biophysical Journal 76(716-724).

Winkler, R. G., Spatz, J. P., Moller, M., Reineker, P. and Marti, O. (1996). "Imaging material properties by resonant tapping-force microscopy: A model investigation." Physical Review B 24(12): 8908-8912.